Mixing and Secondary Circulation in Juan de Fuca Strait

by

Michael William Ott
B.Sc., University of Waterloo, 1992

A Dissertation Submitted in Partial Fulfillment of the
Requirements for the Degree of

DOCTOR OF PHILOSOPHY

in the School of Earth and Ocean Sciences

Abstract

Estuaries, the regions where runoff of freshwater, soil, and contaminants first encounter the ocean, are also primary fishing and recreation areas. It is therefore important to understand the dynamics associated with mixing and currents within these bodies of water. Pollutants and freshwater from river runoff flow out to sea in the upper layer, while nutrient-carrying oceanic water returns beneath. While there have been many studies of the processes involved in this exchange flow, the dynamics and vertical structure of transverse flows are much less understood, despite the role these currents play in redistributing water properties and momentum throughout the estuary.

One such estuary, Juan de Fuca Strait, is an ideal location in which to study estuarine exchange and the resulting cross-channel flows induced by internal friction, primarily because its length and smooth topography reduce the topographic steering of currents. Historical current meter data from a number of deployments in Juan de Fuca Strait reveal that, while mean along-channel currents are roughly consistent with the thermal wind equation, cross-channel flows are not, particularly at mid-depths where transverse currents are largest.

A momentum balance using historical sea level and current meter data suggests that the vertical eddy viscosity $A_v \approx 0.02$ m^{2}s^{-1} at interfacial depths in May. The mean circulation in Juan de Fuca Strait is highly seasonal in nature, however, and larger values may be more appropriate in summer when the estuarine exchange peaks due to the freshet. Stronger friction is in turn associated with elevated mixing rates and increased transverse velocities.

An Acoustic Doppler Current Profiler deployed in Juan de Fuca Strait in the summer of 1996 resolved the vertical structure of these velocities. Concurrent Current-Temperature-Depth data reveal that neither the along- nor the cross-channel currents are in geostrophic balance with the hydrographic structure, suggesting that

the physical processes associated with these currents are more localised than the five kilometre scales over which the hydrography was measured.

Zooplankton within Juan de Fuca Strait comprise a significant part of the scattering cross-section upon which the ADCP depends. During their dusk migration into the euphotic zone to feed and dawn descent to escape predation, they do not act as passive backscatter targets for the Acoustic Doppler Current Profiler. Vertical migration velocities, measured from the backscatter intensity record, reached 0.03 m s^{-1}, suggesting that significant biases in the measured vertical velocity could be introduced. Little effect was actually seen in the velocity fields, however, even though the cross-sectional fraction of the zooplankton was an order of magnitude larger than the background.

Mean currents in Juan du Fuca Strait reveal strong transverse flows at mid-depths, suggestive of interfacial Ekman layers. The along-channel estuarine exchange is significantly enhanced at neap tide, consistent with weaker mixing upstream. The cross-channel flows at interfacial depths are also substantially larger during neap tide, implying a fortnightly modulation of mixing rates within the strait.

The ADCP was also used to measure the Reynolds stresses directly. These were found to be more than an order of magnitude larger at neap tide than during spring tide and were consistent with changes in the mean current over the spring-neap cycle. Reynolds stresses were maximal at mid-depth on the transition from ebb to flood, at which time the gradient Richardson numbers were smallest, suggesting that critical layer absorption of internal waves are important dynamically.

Table of Contents

List of Tables

List of Figures

Acknowledgments

I would like to thank my supervisor Dr. Chris Garrett for his guidance and generous support, as well as my external examiner, Dr. Wayne Geyer, and the members of my committee, Dr. Rolf Lueck, Dr. Andrew Weaver, and Dr. Patrick Cummins, for their comments and suggestions. I would also like to thank Dr. Richard Dewey for many helpful discussions and for lending me his library. I am very grateful to my parents, Bill and Atie for their constant encouragement and support. My wife Laura has been a great source of comfort and encouragement for me and has been wonderful support during the research and writing of this dissertation.

Chapter 1

Introduction and Motivation

Coastal waters have, since early times, been very important in shaping human development and lifestyle. Nearshore upwelling regions are among the most biologically productive areas, accounting for nearly 50% of the global marine food catch with only 10% of the oceanic surface area. Commercial sea traffic is increasing as the world economies become further integrated. Recreational use of coastal seas is also intensifying as urban populations continue to grow, as do the pressures associated with waste disposal and contaminant runoff.

Estuaries, the regions where runoff of freshwater, soil, and contaminants first encounter the ocean, frequently experience large fluctuations in environmental conditions over small time scales. Variations in tidal heights often create large intertidal zones, while tidal currents and wave action result in constantly changing salinities, temperatures, nutrient and gas concentrations, and sediment loads. In addition to these fluctuations, the organisms which inhabit these regions, and upon which we depend for much of our food supply, must increasingly cope with the effects of pollution which is leached from the land or dumped directly into the sea, accidentally or otherwise.

Along-channel currents, which ultimately control the salinity, nutrient, and contaminant concentrations within coastal channels via exchange with the open ocean, have been studied to a far greater extent than vertical and transverse flows. Vertical velocities bring nutrients upward into the euphotic zone where biological production occurs and lead to exchange and entrainment between the upper fresher surface layer and lower oceanic water. Cross-channel flows tend to slow the along-channel exchange by transferring momentum to the sidewalls. They also enhance diffusion within an estuary by exposing tracers to cross-channel differences in the along-channel velocity.

Transverse currents can be significant in regions where friction is important, such as in the bottom boundary and at the interface between inflows and outflows.

Friction is associated with turbulence, the small-scale high-frequency current fluctuations by which energy that is continuously supplied to the oceans by gravitational attraction, solar irradiation, and wind stress is removed. Turbulence enhances diffusion by increasing the exposed surface area of tracers over which molecular processes can act. Cross-correlations in turbulent velocities, or Reynolds stresses, can directly modify currents at longer timescales.

A better understanding of turbulence and of dynamics in general is important not only for local estuaries but also for many different types of global geophysical flows over a wide range of length and time scales. As a semi-enclosed basin which is long, straight, and has relatively smooth topography, Juan de Fuca Strait is an ideal laboratory in which to examine some of these phenomena. In the summer of 1996, an observational programme in the middle section of Juan de Fuca Strait was undertaken to study exchange flow, particularly the friction and dynamics associated with the interface between the inflow and outflow layers.

Chapter 2 provides the theoretical background for the thesis, and includes sections on estuaries, turbulence, and tides. Various estuarine classification schemes and non-dimensional parameters are introduced, as are analytical, numerical, and laboratory models which attempt to explain some of the dynamics. The Navier-Stokes equations are used to review the concepts of Reynolds stress, non-dimensional instability parameters, and log-layer dynamics. The last section considers the structure of barotropic and internal tides in a channel.

Chapter 3 focuses on Juan de Fuca Strait specifically, detailing historical work and highlighting some of the scientific questions raised. The 1996 observational programme is motivated by demonstrating that an area-averaged along-channel momentum balance of the upper layer current requires strong interfacial friction and implies strong transverse currents and turbulence. The hydrographic and current meter data collected to examine the dynamics of Juan de Fuca Strait are discussed in Chapter 4.

A short treatment of the errors associated with the measured velocities and Reynolds stresses is also included.

Since the vertical velocity is significantly smaller than the horizontal components, possible biases and errors in the measured vertical velocity must be examined before Reynolds stresses can be calculated. The difficulties in measuring the vertical velocity are discussed in Chapter 5, and attempts are made to validate these currents. This is done primarily by using the backscatter intensity, a measure of the scattering cross-section upon which the Acoustic Doppler Current Profiler relies to measure velocity. Contamination of the vertical velocity by horizontal components and the problem of spatial inhomogeneity of the flow are also considered.

The vertical structure of the tides is analysed in Chapter 6, particularly for the $M2$ constituent, where attempts are made to quantify the strength of the internal along-channel, cross-channel, and vertical components. Bottom boundary layer dynamics are also explored, including log-layer and rotary current analyses.

In Chapter 7, non-tidal flows are examined. The mean flow is compared to hydrography and to laboratory results of a two-layer rotating flow. Simple models and current meter data suggest that the along-channel current may be subject to baroclinic instability. The spring-neap cycle of the shear instability and in the observed Reynolds stresses are examined and the results are related to changes in the measured mean flow.

Chapter 2

Background

2.1 Estuaries

In most estuaries, freshwater from river runoff mixes with water from the ocean. Cameron and Pritchard (1963) state that an estuary is "a semi-enclosed coastal body of water which has a free connection with the open sea and within which sea water is measurably diluted with fresh water derived from land drainage." Nevertheless, there exist "negative" estuaries, in which evaporation exceeds precipitation and runoff, leading to surface salinities larger than those of the ocean. The dense surface waters within these basins sink and flow out into the sea at depth and are replaced with oceanic return flow at the surface. This thesis will, however, focus on "positive" estuaries, where outflow of diluted surface water is compensated by return flow of dense oceanic water at depth.

2.1.1 Classification Schemes

Categorising the world's estuaries into distinct classes is a difficult, if not impossible, task given their widely varying geometries, bathymetries, mixing rates, and circulations. Furthermore, conditions within an individual estuary can change greatly with location (e.g. relative to the head or mouth), time of year (seasonal changes in freshwater input), and tidal phase (mixing levels). Nevertheless, a number of different classification schemes exist, based on topography, salinity distribution, circulation type, or a combination of these.

a) The Topography of Estuaries

Pritchard (1952) proposes a classification scheme based on topography which has three main categories: drowned river valleys, fjords, and bar-built estuaries. A

fourth group comprises estuaries which do not fall into the general categories, and includes estuaries formed by landslides or movement along tectonic fault lines.

The most common type is the drowned river valley, otherwise known as a coastal plain estuary. These were formed when sea levels rose due to the melting of glaciers and thus generally have depths less than 30 m. Initially carved by rivers, the estuaries are often sinuous and the cross-sections triangular. Width to depth ratios are typically large, and both the width and depth increase toward the mouth. River flow (per tidal period) is typically small compared to the tidal prism (the difference in volume of an estuary between high and low tides).

Fjords, created when glaciers substantially deepened existing river valleys, often have shallow sills at the mouth where glaciers deposited moraine. These estuaries are up to 800 m deep, are generally straight and long (up to 100 km), and have a small width to depth ratio. River input per tidal cycle is usually large compared to the tidal prism since tidal ranges are often restricted, but are very small compared to the water volume within the fjord.

In a bar-built estuary, sediment is deposited at the mouth, forming a bar across the estuary. Sedimentation rates are large and the estuaries are generally only a few metres deep. Occasionally, bars are also formed within the estuary which may create lagoons, stretches of saltwater cut off from the main estuary. River input is large, and varies considerably throughout the year. During periods of unusually large river flow, the bar may be temporarily moved or destroyed.

b) The Salinity Structure Within Estuaries

The hydrography of estuaries ranges from vertically homogeneous through continuously stratified to essentially two-layer. As mentioned, the stratification within an individual estuary can vary over seasonal and tidal cycles, and even along its length. Pritchard (1955) and Cameron and Pritchard (1963) distinguish four main types of estuaries based on the observed salinity structure: homogeneous (well-mixed), partially-mixed (partially-stratified), fjords, and salt wedge, where the latter two are sometimes collectively termed highly-stratified.

For estuaries of small depth, turbulence associated with bottom friction acting on the tides may be sufficient to vertically mix the entire water column. These vertically homogeneous estuaries can be either laterally homogeneous, which occurs when the width is small enough that friction laterally mixes the estuary, or inhomogeneous, in which case the flow may be horizontally separated. In the former case, flow is outward at all depths, and the outward advection of salt by the mean flow is balanced by the inward turbulent diffusion of salt due to eddies. In laterally inhomogeneous estuaries, horizontal circulation tends to transport salt up-estuary along the left side of the channel (in the Northern hemisphere) due to rotation.

The partially-mixed estuary is characterised by limited vertical stratification: turbulent mixing, while intense, is not sufficient to completely homogenise the water column. Salt and water are entrained into the upper layer, increasing both surface salinity and water transport. The resulting density structure drives a return flow in the lower layer to balance the salt loss in the upper layer.

The highly-stratified estuary is subdivided into two types: the salt-wedge and the fjord. In salt-wedge flow, river flows are considerably larger than tidal flows (Dyer 1973), and the sea water intrudes upstream as a wedge below the fresh layer. The position of this salt wedge depends on the strength of the river flow, and oscillates horizontally with the tide. Salty water will be entrained into the upper layer, increasing the discharge rate as the mouth is reached and requiring a landward flow in the salt wedge to balance the salt loss. The salinity inside the salt wedge does not change in the along-channel direction since there is no entrainment into the lower layer. The fjord estuary is similar to the salt-wedge flow, except that the lower layer is often much deeper, and a sill usually exists at the mouth of the estuary. Occasionally, the sill is shallow enough to cut off the return flow, and the lower layer in the estuary stagnates. Renewal sometimes occurs only annually, when the river flow is at its peak. At these times, entrainment is large, and the density difference between the lower layers of the estuary and the ocean is greatest.

c) Estuarine Parameters

Many attempts have been made to develop a classification scheme based only on external parameters such as the tidal current strength, the freshwater input, and dimensions of the estuary. The goal, essentially, is to identify the physical processes leading to the observed salinity structure.

Perhaps the simplest scheme is that proposed by Simmons (1955) and based on the ratio of the river input per tidal cycle to the tidal prism. The former is $Q_f T$, with Q_f the freshwater volumetric input rate and T the tidal period. The tidal prism for an estuary of width W and depth H at the mouth is $P_T = WHu_T T$, where u_T is the mean tidal flow. For $Si = Q_f/(WHu_T)$ of order unity, arrested (salt-wedge) flow is usually found, a situation in which a thin layer of fresh water overlays a stationary layer of oceanic water, with little to no entrainment or mixing between the two layers. Ratios of 10^{-1} and 10^{-2} correspond to partially-stratified and well-mixed estuaries, respectively. However, in omitting gravity and the density difference between fresh and oceanic water, the stabilising influence of buoyancy has not been properly considered.

Civil engineers have long used the 'estuary number', $E_s = P_T F_o^2/(TQ_f)$ for a tidal channel, where $F_o = u_T/\sqrt{gH}$ is the external Froude number, "to correlate model experiments and field data" (Turner 1973). With the above definitions for the Simmons parameter and the tidal prism, $E_s = F_o^2/Si = Wu_T^3/(gQ_f)$. Values of 0.03 to 0.3 define the transition between stratified and well-mixed estuaries, with larger E_s implying greater vertical homogeneity (Turner 1973).

A related parameter, based on the "pipe Richardson number" (Ellison and Turner 1960) is the "estuarine Richardson number" Ri_e. This is the ratio of the buoyancy input (due to a river) per unit width ($\Delta\rho g Q_f/W$, where $\Delta\rho$ is the density difference between fresh and ocean water) to the mixing power of the tides (u_T^3). Using the mean density ρ_o to non-dimensionalise,

$$Ri_e = \frac{g\Delta\rho}{\rho_o}\frac{Q_f}{Wu_T^3} \tag{2.1}$$

Estuarine observations suggest that "transition from a well-mixed to a strongly stratified estuary occurs in the range $0.08 < Ri_e < 0.8$" (Fischer *et al.* 1979).

The estuary number and estuarine Richardson number are closely related: $Ri_e = \Delta\rho/\rho_o E_s^{-1}$. With the density ratio $\Delta\rho/\rho_o \approx 0.02$ in most estuaries (Turner 1973), the transition regions for the two parameters are, not surprisingly, almost identical. On the other hand, the ratio between the estuarine Richardson number and the parameter proposed by Simmons (1955) is $Ri_e/Si = g'H/u_T^2 = 4Fr'^{-2}$, where Fr' is the internal Froude number based on the tidal speed and the internal wave speed for a two-layer flow with freshwater of depth $H/2$ above oceanic water of equal depth.

In his analysis of estuarine adjustment to changes in river flow and tidal mixing MacCready (1999) considers the three fundamental velocity scales in an estuary: the river velocity $\overline{u} = Q_f/(WH)$, the root mean square (rms) tidal velocity u_T, and the maximum internal wave speed $C_o = \sqrt{g'H/4}$, just as Hansen and Rattray (1966) had done earlier. From these three velocities, two non-dimensional parameters can be defined. Whereas Hansen and Rattray (1966) chose the "densimetric Froude number" $F_m = \overline{u}/C_o$, and the flow ratio $P = \overline{u}/u_T$, MacCready found it more convenient to use F_m and $\Gamma = u_T/C_o$, as these yield independent measures of the river flow and tidal amplitude, respectively. Of course, these choices are arbitrary and the resulting parameters are clearly related: $\Gamma = F_m/P$.

It is also not surprising that these parameter pairs are related to the earlier set (Ri_e, Fr'), with $F_m = Ri_e Fr'^3/4$ and $\Gamma = Fr'$. This begs the question of the number of separate non-dimensional parameters needed to adequately describe the range of estuary types. The work of Hansen and Rattray (1966) and MacCready (1999) suggest that there are two, unless they appear in only one combination in the governing equations. In this case, which may occur only for simplified forms of the equations, only one parameter may be needed.

Ignoring the effects of wind stress, the characteristic external parameters for an estuary are Q_f, W, H, L, u_T, g, and $\Delta\rho$, where L is the length of the estuary. Noting that it is the freshwater input per unit width which defines the local buoyancy anomaly, that $\Delta\rho$ needs to be divided by a background density ρ_o as it is the only parameter involving mass, and that the length of the channel should not affect the tidal currents or freshwater input, non-dimensional parameters classifying estuaries should be based on $Q_f/W, H, u_T, g$, and $\Delta\rho/\rho_o$. Furthermore, gravity acts upon the density difference, so the latter two terms should be combined as $g' = g\Delta\rho/\rho_o$, the estuary number E_s notwithstanding. The four remaining parameters involve only two dimensions (length and time), implying two non-dimensional numbers. Nevertheless, "the idea of being able to predict estuarine structure from a few simple external parameters remains elusive" (MacCready 1999).

Rather than using external parameters, Hansen and Rattray (1966) proposed a classification scheme which utilises parameters involving the measured hydrography and current structure within an estuary. Two dimensionless parameters, based only on salinity and velocity, classify estuaries along a continuum rather than into distinct classes. The two-dimensional parameter space is divided into characteristic regions, similar to those proposed by Pritchard (1955), based on the ratio of the tidal diffusion salt flux to the total up-estuary salt flux. The stratification parameter is $\delta S/S_o$, where δS is the surface to bottom difference in salinity and S_o is the mean cross-sectional salinity. The circulation parameter u_s/u_m, with u_s the net surface current averaged over a tidal cycle, and u_m the mean cross-sectional velocity (i.e. $\overline{u}$, the river input divided by the cross-sectional area), is a measure of the amount of entrainment into the upper layer. For partially-mixed estuaries of rectangular cross-section, the circulation and stratification parameters can be related to the external parameters F_m and P.

d) Estuarine Models

Hansen and Rattray (1965) analytically modelled two-layer flows in partially-mixed estuaries and expressed the circulation as the sum of three modes: river discharge, the gravitational-convection mode, and wind-stress flow. While only the flow associated with river discharge produces a net transport of water, each mode affects the salinity distribution within the estuary. Gravitational convection is a result of the horizontal salinity gradients caused by entrainment as the river discharge flows downstream; heavier water slumps beneath lighter upstream water, providing an upstream salinity flux and tending to create vertical salinity gradients. As a result of this interaction between salinity and velocity, salinity gradients in an estuary are stabilised against large variations in river input. The large increase in salinity gradients expected from increased outflow is offset by increased upstream salt advection in the presence of vertical variations in salinity. Thus, while estuarine velocities and the salinity field are strongly coupled, advection of salinity implies that velocities cannot be reliably determined from the stratification. The authors suggest that "deep estuaries in particular may have well-developed gravitational convection even though tidal mixing nearly destroys the vertical salinity gradient" (Hansen and Rattray 1965). In addition, even for small horizontal salinity gradients, deeper estuaries are more likely to have a mean upstream flow at depth.

The Hansen and Rattray (1965) analysis involved finding similarity solutions for two dimensional flow in a laterally homogeneous estuary where the momentum balance is $p_x/\rho = (A_v u_z)_z$ and $p_z/\rho = -g$ in the along-channel and vertical directions, respectively, with the subscripts x and z indicating spatial derivatives and A_v the vertical eddy viscosity. The model included conservation of water, $(Bu)_x + (Bw)_z = 0$, and salt, $B(uS_x + wS_z) = (BK_hS_x)_x + (BK_vS_z)_z$, as well as a linear equation of state $\rho = \rho_f(1 + kS)$, where B is the channel width, S the salinity, ρ_f the density of freshwater, and with K_h and K_v the horizontal and vertical turbulent diffusivity, respectively. A_v was not allowed to vary spatially, the bottom streamfunction was set to to zero (the no-slip condition), stresses at the free surface were matched to

the wind stress, the net transport was forced to equal the river inflow, and the width B was assumed constant. The similarity solutions were then matched with observed mean velocity and salinity profiles to estimate the three exchange coefficients (A_v, K_h, and K_v). In Juan de Fuca Strait, they find $A_v \approx 0.0075$ m^2 s^{-1}, based primarily on data by Herlinveaux (1954) and Waldichuk (1957), although they note that there are no detailed dynamical studies of Juan de Fuca Strait to support this or to suggest how A_v may vary spatially.

MacCready (1999) used analytical and numerical models to study time dependent two-layer estuarine flow. In particular, he was interested in the response of estuaries to changes in fresh water discharge, and noted that results depended on channel depth. Holding all other parameters (i.e. the river discharge, salinity difference, tidal strength, and channel width) constant, he found that the diffusive fraction of the up-estuary salt flux decreased as the depth increased. That is, for deeper estuaries, the primary balance in the salt budget is between the mean flow (down-estuary) and the exchange flow (up-estuary), whereas in shallower estuaries the primary balance is between the mean flow and diffusion brought about by longitudinal tidal mixing.

The diffusive fraction of the up-estuary salt flux is zero in a perfect two-layer estuarine flow, and increases continuously through the salt wedge, partially-stratified and well-mixed estuarine regimes until it is unity for the vertically and horizontally homogeneous case. The traditional estuarine Richardson number also spans the range of these estuary types. However, superimposing lines of constant Ri_e on the diffusive fraction versus (Γ, F_m) phase space diagram of MacCready (1999) reveals that the diffusive fraction is not constant for a given value of Ri_e, implying that the estuarine Richardson number is not sufficient to adequately determine the estuary type.

2.1.2 The Partially-Mixed Estuary

Along-channel flow is the dominant mean (i.e. excluding tides) circulation in an estuary with appreciable freshwater input from land drainage, and has been studied extensively (Rattray and Hansen 1962; Fischer *et al.* 1979; Labrecque *et al.* 1994;

Mertz and Gratton 1995) in a wide variety of estuaries. Freshwater input from rivers creates a dynamic head which drives an upper-layer outflow. Within the channel, this water entrains surface seawater, resulting in an export of salt from the estuary in the upper layer. Mixing also ensures that isopycnals become more shallow in the seaward direction, causing a baroclinic pressure gradient which opposes the surface pressure gradient. At depth, the net pressure gradient is reversed, forcing a return flow of salty ocean water into the estuary. This flow maintains the overall salinity content of the estuary. For a two-layer estuarine flow in the absence of diffusive fluxes, volume and salt conservation imply the well-known Knudsen equations

$$Q_1 = \frac{Q_f}{1 - S_1/S_2} \qquad \text{and} \qquad Q_2 = Q_1 S_1/S_2 \tag{2.2}$$

which express the volumetric outflow and inflow rates (Q_1 and Q_2, respectively) as functions of the salinities in the upper and lower layers (S_1 and S_2, respectively), and the freshwater input.

2.1.3 The Effects of Rotation

Cross-channel tilts in the isopycnals are established to geostrophically balance the along-channel flow. Sea surface slopes set up by the outflow in the upper layer are typically very small, owing to the large density difference between air and water. The isopycnal slopes, required to counter the sea surface slope and balance the lower layer inflow, are of the opposite sign and are much larger in magnitude, as density differences within the fluid are two to three orders of magnitude smaller.

That along-channel currents in the upper layer are relatively constant from the mouth to the head of Juan de Fuca Strait despite the presence of a dynamic head requires that frictional forces be significant. The resulting breakdown in the geostrophic balance implies that substantial cross-channel flows, in addition to those arising from local bathymetric steering and tidal rectification, should result. Nevertheless, secondary flow has been studied to a much lesser extent than the main

estuarine circulation, and although various mechanisms have been proposed, it remains poorly understood.

Sidewall friction induces mixing and the resulting water would be expected to spread into the interior along the appropriate isopycnals. Interfacial friction of a sufficient magnitude would imply mixing between the upper fresher and lower saltier waters, which alters the along- and cross-channel slopes of isopycnals at the mixing depths, leading to transverse currents. A third mechanism leading to cross-channel currents is Ekman layer dynamics, both at solid boundaries (Trump 1983; Johnson and Sanford 1992) and at the interface between inflow and outflow (Csanady 1972). Just above the interface, reduced along-channel flows lead to an imbalance between the Coriolis force and the cross-channel pressure gradient, inducing a flow to the left (Northern hemisphere) across the strait. Just below the interface, one would expect cross-channel flows in the opposite direction in the interfacial Ekman layer.

Mertz and Gratton (1995) examined cross-channel flow in the St. Lawrence River, and found that while near surface currents were all very close to along-channel alignment, deeper currents deviated considerably. Examining the balance between pressure, frictional, and Coriolis forces in along-channel momentum, they considered the cross-channel flows arising from pressure and frictional effects separately. The "pressure gradient velocity" and "frictional steering velocity" are given by

$$v_p = \frac{1}{f\rho_o}\frac{\partial p}{\partial x} \qquad \text{and} \qquad v_f = -\frac{1}{f}\frac{\partial}{\partial z}\left(A_v\frac{\partial u}{\partial z}\right) \tag{2.3}$$

Without knowledge of the along-channel sea surface slope, they were only able to determine the vertical shear in the pressure velocity and could not compare it to the frictional steering velocity. However, through a scale analysis, they demonstrated that both may be important in generating lateral flows. They also performed a linear regression between the observed cross-channel flow and the second vertical derivative of the measured along-channel flow to estimate the vertical eddy viscosity. Although there was no significant relationship when the second derivative was weak, they found $A_v \approx 0.004\ \mathrm{m^2\ s^{-1}}$. Nevertheless, it may not be appropriate to consider

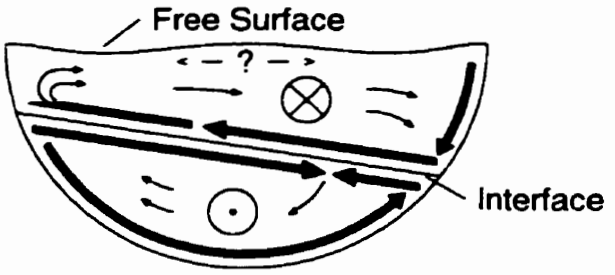

Fig. 2.1. Laboratory results of rotational exchange flow (Johnson and Ohlsen 1994). Thick arrows indicate Ekman layer flows while thin arrows indicate interior flows.

these effects separately, as friction and the along-channel pressure gradient are related: the presence of friction creates interfacial Ekman layers, leading to a change in the cross-channel isopycnal slopes and hence to along-channel flow. This requires cross-channel interior flow which must be in geostrophic balance with the along-channel pressure gradient.

Johnson and Ohlsen (1994) found significant secondary circulation (Figure 2.1) in laboratory experiments of frictionally modified rotating hydraulic channel exchange flow. They determined that the cross-channel flows limited the magnitude of the along-channel exchange flow. Ekman layers were found at the bottom and sidewalls, as expected in a frictional boundary layer where the balance between the pressure gradient and Coriolis force is broken. In addition, interfacial Ekman layers were seen both above and below the interface between the two layers of differing density.

They found that, at the deep side of the channel (defined as the side where the pycnocline is deeper), the cross-channel flow of water on both sides of the interface is into the interior. In the lower inflow layer, bottom friction causes a bottom Ekman layer flow toward the sidewall on the deep side, which is forced into the interior just below the interface, and in the upper outflow layer, interfacial friction directly causes the Ekman layer seen. This convergence of water results in a tightening of the isopycnals at the deep side. In contrast, the interfacial Ekman layer of the upper layer and the bottom Ekman layer of the lower layer diverge at the shallow side of

the channel, causing a decrease in stratification. This process is aided by the Ekman interfacial layers, which induce a cross-channel shear in the interface.

Their analysis did not attempt to explain at which point along the interface the cross-channel flows just below the interface converge, what dynamics occurs there, or what implication this has for mixing rates. They did find, however, that the upper layer interfacial Ekman layer increased sidewall friction by bringing the higher along-channel velocities of mid-channel closer to the wall. They concluded that both friction and rotation are important in channel dynamics, and that the Ekman layers also limit the exchange through the channel by driving strong cross-channel circulations which bring water with reduced along-channel velocities from the boundaries into the interior.

2.2 Turbulence

Away from solid boundaries and the interfaces of water masses, molecular frictional forces are weak compared to Coriolis and pressure forces. That much of the ocean's currents are in geostrophic balance provides confirmation that "the direct effect [of friction] on large-scale motion has been shown ... to be utterly negligible" (Pedlosky 1979). Nevertheless, the fact that both oceanic currents and external forcing (such as solar radiation and wind stress) are steady in time, when averaged appropriately, indicates that friction is vital in removing energy from large scale flows.

Although global currents are too large in scale for molecular friction to work against directly, the length scales in any geophysical flow cover the spectrum from that of the main flow to the scales small enough that molecular diffusion is important. In an average sense, energy is continuously removed from shear in large-scale flows, cascaded through turbulent eddies of ever decreasing size, and eventually dissipated into heat energy at molecular scales.

Recognising both that frictional effects need to be considered in the dynamics of oceanic flows and that the range of length scales involved is too large to allow for resolution of the small-scale turbulent eddies themselves, there is clearly a need to

parameterise these viscous effects. That is, the dissipation of energy (at small scales) taken from the large-scale flow must be related to properties of the main flow and of the boundary only.

A similar problem exists for gradients of temperature, salinity, and scalar properties of the flow such as nutrient and dissolved gas concentrations. The gradients which exist in the large-scale flow are initially increased through the action of turbulent eddies which stretch regions of high concentrations into thin filaments, enabling molecular diffusion to act over a very large surface area. The flux of a scalar due to random molecular motions is from regions of high to low concentration, and is modeled as $-\kappa_S \nabla S$ (Batchelor 1967), where κ_S is the diffusion coefficient and ∇S the scalar gradient of the scalar quantity S. This parameterisation is used as a model for that of eddy "diffusion" due to turbulence.

2.2.1 Reynolds Stress

The momentum, or Navier-Stokes, equations relate the total change in velocity (with time and by advection) to the pressure gradient, gravity, the Coriolis force, and horizontal and vertical diffusion. With $\boldsymbol{u}= (u, v, w)$ the three-dimensional velocity, f the Coriolis parameter, p pressure, ρ the density, ρ_o an average density, subscripts x, y, z, and t denoting partial differentiation, ν the kinematic molecular viscosity, and g gravity, the momentum equations can be written

$$\begin{aligned} u_t + \boldsymbol{u}\cdot\nabla u - fv &= \frac{-1}{\rho_o} p_x + \nu\nabla^2 u \\ v_t + \boldsymbol{u}\cdot\nabla v + fu &= \frac{-1}{\rho_o} p_y + \nu\nabla^2 v \\ w_t + \boldsymbol{u}\cdot\nabla w + g &= \frac{-1}{\rho} p_z + \nu\nabla^2 w \end{aligned} \tag{2.4}$$

where the depth-dependent density is kept (i.e. instead of the reference density) in the third equation to allow for the effects of gravity. The last term in each of the

momentum equations is the gradient of molecular diffusion of momentum, with the dynamic molecular viscosity $\mu = \rho\nu$ held constant.

To examine the effect of turbulent flow on the mean, a Reynolds decomposition of the current, density, and pressure is used, in which each variable is separated into a mean and a time-varying component. The pressure, for example, becomes $p = \overline{p} + p'$, where $\overline{p} \equiv < p >$, and $< p' > \equiv 0$, with $<>$ denoting an average over a suitable time period. Substituting into the u-momentum equation (2.5) and averaging, the resulting equation

$$\overline{u}_t + \overline{\boldsymbol{u}}\cdot\nabla\overline{u} + (\overline{u'u'})_x + (\overline{u'v'})_y + (\overline{u'w'})_z - f\overline{v} = \frac{-1}{\rho_o}\overline{p}_x + \nu\nabla^2\overline{u} \qquad (2.5)$$

shows that the material derivative of $\overline{u}$ changes not only in response to mean forces, but also due to the gradient of velocity fluctuation correlations. The correlations themselves, when multiplied by density (e.g. $\rho\overline{u'w'}$), are called Reynolds stresses: there are similar terms in the v and w momentum equations. Except near solid boundaries where turbulent fluctuations are small, the effect of these stresses is much larger than that of the viscous term, which is consequently omitted.

The nine Reynolds stress terms need to be related to mean flow values in order to close the system, and the simplest parameterisation is analogous to that for the molecular diffusion of momentum. That is, the turbulent diffusion of momentum is related to the mean shear

$$-(\overline{u'u'}, \overline{u'v'}, \overline{u'w'}) = (A_x\overline{u}_x, A_y\overline{u}_y, A_v\overline{u}_z) \qquad (2.6)$$

where the eddy viscosities (A_x, A_y, A_v) are the proportionality constants. Assuming that $A_x \approx A_y \equiv A_h$ (A_v is smaller owing to stratification and the fact that the vertical length scale is much smaller than the horizontal scale) the u-momentum equation becomes

$$u_t + \boldsymbol{u}\cdot\nabla u - fv = \frac{-1}{\rho_o}p_x + \nabla_h\cdot(A_h\nabla_h u) + (A_v u_z)_z \qquad (2.7)$$

where $\nabla_h = (\partial/\partial x, \partial/\partial y)$ is the horizontal gradient operator, (A_h, A_v) are the (horizontal,vertical) eddy viscosities, and the overbars indicating average quantities have been dropped.

A similar procedure is followed for the equations of conservation of heat, salinity, and other scalars. Reynolds fluxes, the mean movement of properties by correlations in velocity and property fluctuations, are related to background gradients of those properties. For example,

$$-(\overline{T'u'}, \overline{T'v'}, \overline{T'w'}) = (K_h \overline{T}_x, K_h \overline{T}_y, K_v \overline{T}_z) \tag{2.8}$$

where T' are temperature fluctuations, and (K_h, K_v) are the (horizontal,vertical) eddy diffusivities of heat. The equation for heat, neglecting internal sources such as the absorption of solar radiation,

$$T_t + \boldsymbol{u} \cdot \nabla T = \kappa_T \nabla^2 T \tag{2.9}$$

where κ_T is the molecular diffusivity of heat, becomes, upon use of the Reynolds decomposition and the above parameterisation for Reynolds fluxes,

$$T_t + \boldsymbol{u} \cdot \nabla T = \nabla_h \cdot (K_h \nabla_h T) + (K_v T_z)_z \tag{2.10}$$

Unfortunately, while molecular viscosities and diffusivities are properties of the fluid, their turbulent counterparts are properties of the flow. In addition, the parameterisation itself "does not produce very exact results except in special cases" (Pond and Pickard 1983), such as the bottom boundary layer where A_v has been shown to vary linearly with height. Nevertheless, the parameterisation can often be used to show that, in certain cases, Reynolds stresses are small compared to other terms in the momentum equation and can be omitted.

2.2.2 The Reynolds Number

The non-linear terms in the Navier-Stokes equations of motion can cause small perturbations in the flow to grow into large fluctuations, while molecular friction acts to remove them. The scaled ratio of the along-flow advective (i.e. non-linear) term to the term representing molecular viscosity is the Reynolds number

$$Re = \frac{UL}{\nu} \tag{2.11}$$

with U a typical current speed in the flow and L a typical length scale, is a non-dimensional measure of the instability to turbulence of flows in homogeneous fluids.

Transition from laminar to turbulent flow does not occur at the same Reynolds number for all flows however. That is, the transition depends on flow conditions, such as the intensity of the initial perturbations, as well as on boundary conditions such as roughness and geometry (e.g. wall-bounded flow versus jet flow). In addition, the transition is not instantaneous, but occurs in stages of increasing complexity. In the case of wall-bounded parallel shear flow, for example, instability first manifests itself as two-dimensional Tollmien-Schlichting waves "which grow and eventually reach equilibrium at some finite amplitude" (Kundu 1990). Indeed, for homogeneous fluids, Squire (1933) proved that "for each unstable three-dimensional wave there is always a more unstable two-dimensional one travelling parallel to the flow", and Yih (1955) extended the theorem to non-homogeneous fluids. These two-dimensional waves are, in turn, unstable to three-dimensional waves of short wavelength.

Nevertheless, Reynolds numbers for oceanic conditions are well above those found to correspond to the transition to turbulence in the laboratory (e.g. 10 for free-shear layers or 10^3 for wall-bounded flow (Kundu 1990). For example, in Juan de Fuca Strait, where $U \sim 0.1$ m s^{-1} is a typical mean along-channel flow, $L \sim 10^2$ m is the depth scale of the flow, and $\nu \approx 1.4 \times 10^{-6}$ m^2 s^{-1}, $Re \approx 10^7$. One might therefore expect that all oceanic flows are turbulent. Stratification, however, acts to stabilise flows, lowering the rate of transfer of momentum, temperature, and concentrations

of scalars within the flow. After a brief discussion of the effect of turbulence in the well-mixed bottom-boundary layer, the effect of stratification on stability will be considered.

2.2.3 The Bottom-Boundary Layer

Frictional contact between currents and the bottom boundary implies that water in direct contact with the boundary has zero velocity, and thus that a shear layer exists near the bottom. Geophysical flows are generally turbulent and the eddies bring faster-moving water closer to the boundary and slower-moving water farther away. The resulting increase in the local velocity gradients enhances the role of viscosity as compared to its role in laminar flows; eddy viscosities are generally orders of magnitude larger than molecular viscosities, greatly augmenting momentum transfer between the flow and solid boundary.

The momentum is dissipated against the bottom boundary in a thin sublayer where viscosity and bottom roughness are important. Just above the "viscous sublayer" is a layer through which the momentum of the free-stream velocity U_∞ is transferred to the boundary. (In fully developed turbulent flow, there is a constant cascade of energy from large to small scales.) The velocity gradient in this region should therefore not depend on the viscosity, but rather only on the height above the bottom z, the density ρ, and the momentum flux. The flux is clearly related to the dissipation at the boundary which gives rise to the bottom stress τ_o. Dimensionally, this implies a velocity profile of the form

$$U(z) = \frac{u_*}{\kappa} \ln(\frac{z}{z_o}) \qquad u_* = \sqrt{\tau_o/\rho} \qquad (2.12)$$

where u_* is the "friction velocity", κ is von Karman's constant, z_o is the bottom roughness, and where $U(z)$ reaches zero at $z = z_o$, a height above the bottom equal to the length scale of bottom roughness. The stress across the "log-layer" is constant with depth because "there is little production or dissipation; there is simply an inertial

transfer ... " (Kundu 1990). That is, the log-layer lies above the viscous sublayer, where momentum is dissipated against the wall, and below the main turbulent flow, where turbulent energy is drawn from the mean current.

The log-layer lies beneath a layer in which the shear weakens to the point where the effects of the Earth's rotation become important. The log-layer height should therefore clearly depend on the strength of the flow, U_∞. For steady homogeneous flow, one measure of the boundary-layer thickness (i.e. of the entire layer, and not merely the log-layer region) is $z_h = u_*/f$ (Gill 1982). Soulsby (1983) found that the log-layer height was a small fraction of this (i.e. $z_h = 0.04u_*/f$) in the Celtic Sea, and Tennekes (1973) found similar results ($z_h = 0.03u_*/f$) in the atmosphere.

Given the turbulent nature of the flow in this layer, the transfer of momentum is not regular, and the log profile will not accurately describe the instantaneous horizontal current. To obtain the constant rate of momentum transfer needed to make the log-layer argument valid requires averaging the horizontal currents in time. In the atmosphere, "averaging times required are of the order of minutes for points a few meters above the ground." (Gill 1982). Longer averaging times are needed to sample the same number of eddies in the ocean because mean flows are smaller.

Experimentally, calibrations of the log fit with direct measurements of the stress at the bottom boundary yield a value for von Karman's constant of $\kappa \approx 0.41$. The log fit can then be used to estimate the bottom stress in geophysical flows, where direct measurements are less practical. The bottom stress can be related to the flow speed at a given height above the bottom, U_{ref}, through the use of a dimensionless drag coefficient C_D. Dimensionally,

$$\tau_o = \rho C_D U_{ref}^2 \tag{2.13}$$

where C_D is found experimentally to depend on bottom roughness, U_{ref}, and the stratification. Drag coefficients are then used in numerical models to parameterise the friction on currents arising from solid boundaries, although the proper magnitude of the coefficient, as well as its spatial variation, is not readily agreed upon.

In addition to transferring energy from large to small scales, turbulence acts to mix water, redistributing water properties such as temperature, salinity, dissolved gas, and nutrients in such a way as to reduce their gradients. Hydrographic profiles typically reveal bottom layers in which temperature and salinity, for example, are nearly constant with depth. The thickness of these layers varies with the strength of the turbulence, which is in turn dependent on the magnitude of the shear and the bottom roughness, as well as on the stratification itself. The thickness of the well-mixed layer should be greater on average than the thickness of the dynamic log-layer because turbulence exists outside the log-layer. In addition, in regimes where tidal flows are important, the well-mixed layer in density is more persistent than the log-layer for velocity. While the log-layer disappears and re-establishes itself as the tide turns, restratification is unlikely to occur over much of the thickness.

2.3 Stability in the Presence of Stratification

Stable systems are those in which wavelike perturbations do not grow by removing energy from the background state. Many geophysical flows, on the other hand, are unstable, and initially small disturbances increase in magnitude, leading to fluctuations in the mean currents and hydrography which are not in phase with the seasonal and diurnal cycle of forcings of the sun, moon, and wind. These fluctuations also affect the mean flow, so that the observed flow is not the one which should be properly used in a stability analysis. That is, "the time-averaged state ... is frequently found to be more stable than the relevant initial state" (Pedlosky 1979), although, in practice, the mean state is often that which is used.

There are many mechanisms which can lead to instability in geophysical flows, but in most cases, with wave-wave interactions being one exception, the instability grows by extracting energy from the background state. In convective instability the background density field is statically stable, but unstable to vertical displacements of water parcels. That is, the potential density is unstable; the in-situ density decreases less with height than a displaced water parcel would due to pressure effects. Salt

fingers grow as a result of the different molecular diffusion rates of salt and heat. Barotropic instabilities remove energy from horizontal variations in the main flow. Shear instability, in which energy is removed from shear in the background flow, and baroclinic instability, for which the energy source is available potential energy are considered in more detail.

2.3.1 Shear Instability

In a homogeneous fluid, the ratio of the non-linear to viscous terms in the Navier-Stokes equation is a measure of instability. In a non-homogeneous fluid, however, gravity suppresses turbulence by increasing the amount of energy needed to raise heavier water. The square root of the ratio of the scaled non-linear terms ($\rho_o U^2/L$) to the buoyancy term ($g\Delta\rho$ in a two-layer system, where $\Delta\rho$ is the density difference between the upper and lower layers) is $Fr' = U/\sqrt{g'H}$, with H the vertical length scale of the flow. For a continuously stratified fluid, the internal Froude number becomes $Fr' \equiv U/(NH)$, where

$$N^2 \equiv -\frac{g}{\rho_o}\frac{\partial \rho}{\partial z} \tag{2.14}$$

is defined as the buoyancy frequency. It is more common, however, to use the inverse square of the internal Froude number, a non-dimensional parameter known as the bulk Richardson number ($Ri = N^2H^2/U^2$). The gradient Richardson number

$$Ri = \frac{N^2}{\partial^2 U/\partial z^2} \tag{2.15}$$

is the local value of the bulk parameter, i.e. using $N(z)$ and $U(z)$.

Another form of Richardson number arises from consideration of terms in the equation of turbulent kinetic energy. Summing the scalar product of the three-dimensional perturbation momentum equation and the perturbation velocity $\boldsymbol{u}=(u_1, u_2, u_3)$ and defining the fluctuating strain rate $e_{ij} \equiv (\partial u_i/\partial x_j + \partial u_j/\partial x_i)/2$, the turbulent kinetic energy equation is

$$\left(\frac{\partial}{\partial t} + U_j \frac{\partial}{\partial x_j}\right) \frac{1}{2}\overline{u_i u_i} + \frac{\partial}{\partial x_j}\left(\frac{1}{\rho_o}\overline{p\,u_j} + \frac{1}{2}\overline{u_i u_i u_j} - 2\nu\,\overline{u_i \epsilon_{ij}}\right) = -\overline{u_i u_j}\frac{\partial U_i}{\partial x_j} + g\,\overline{w\rho}/\rho_o - 2\nu\,\overline{\epsilon_{ij}\epsilon_{ij}} \qquad (2.16)$$

where summation over the subscripts i and j is understood. $\boldsymbol{U}$ is the mean flow, and $q^2 \equiv u_i u_i = u_1^2 + u_2^2 + u_3^2$ is twice the turbulent kinetic energy. The first two terms are recognised as the material derivative, the third and fourth are the transport of energy by turbulent pressure gradients and turbulent convection, respectively, and the last term on the left side is viscous transport. The first term on the right side is the shear production of turbulent kinetic energy, i.e. the effect of the interaction of the Reynolds stress with the mean shear. This term is usually positive, implying a transfer of kinetic energy from the mean to turbulent flow. The second term is the buoyant production of turbulent kinetic energy, which can be of either sign, and the last term is the viscous dissipation, ϵ.

The flux Richardson number

$$R_f \equiv \frac{g\,\overline{w\rho}/\rho_o}{-\overline{uw}\,dU/dz} \qquad (2.17)$$

is the ratio of the buoyant destruction to shear production (of turbulence) terms in the turbulent kinetic energy equation. A stable density profile (for which $R_f > 0$) acts to suppress turbulence, while unstable stratification ($R_f < 0$) results in convection. When $R_f > 1$, buoyancy clearly removes turbulence at a greater rate than it is produced by the shear. However, dissipation also removes turbulence: observations (Panofsky and Dutton 1984) show that turbulence decays when $R_f \gtrsim 1/4$.

The flux Richardson number is, however, difficult to measure. Using the eddy coefficient assumption for momentum (2.6) and a similar assumption for density, i.e. $-\overline{w\rho} = K_v d\overline{\rho}/dz$ (compare to 2.8), the flux and gradient Richardson numbers are related as $Ri = A_v/K_v\, R_f$, where A_v/K_v is the turbulent Prandtl number. This ratio

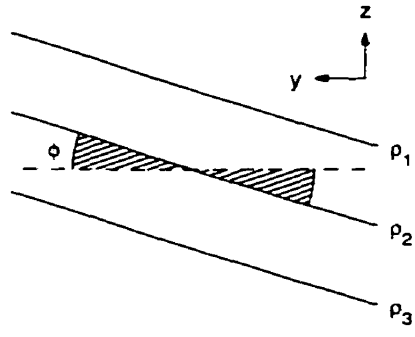

Fig. 2.2. Wedge of instability (shaded region) between sloping isopycnals (solid lines) and horizontal (dashed line). Displacements from one region to another release potential energy, allowing for the growth of baroclinic instabilities.

is unity in neutrally stable environments, but can be larger but for stable stratification, since momentum can also be transferred through internal waves. The momentum flux is not reduced as much as the buoyancy flux, implying that turbulence can persist for gradient Richardson numbers larger then 1/4. This can be true even for $Ri > 1$ (Turner 1981; Bradshaw and Woods 1978). Indeed, "because of non-uniform flow the transition [from laminar to turbulent flow] will occur at a higher Ri [than 1/4]" (Dyer 1973).

2.3.2 Baroclinic Instability

Whereas the kinetic energy of the mean flow is the source of energy in shear instability, in baroclinic instability small disturbances grow at the expense of potential energy stored in sloping isopycnals. In this way, it is a form of convective instability, although isopycnal slopes do not imply the presence of available potential energy. Only vertical displacements falling within the wedge formed between the horizontal and lines of potential density (Figure 2.2) do not feel a restoring force, but are rather accelerated further. Horizontal boundaries limit the horizontal scales of motion, which, in turn, limit the ability of disturbances to lie within the wedge.

Pedlosky (1979) used dimensional arguments to show that the requirement that displacement falls within the wedge (i.e. $0 < tan(o) < (\partial z/\partial y)_\rho$, where the upper bound is the isopycnal slope) is equivalent to $L \gtrsim L_H$, where L is the horizontal scale of motion and $L_H = NH/f_o$ is the Rossby radius of deformation based on the buoyancy frequency and water depth. For the basic state of along-channel flow, the isopycnals slant in the cross-strait direction, implying that the width is the relevant length scale in limiting horizontal displacement.

a) Two-Layer Flow

In modelling mathematically the two-layer baroclinic instability seen in a small gap annulus, Stern (1975) expanded the one-layer quasi-geostrophic potential vorticity equation in powers of the Rossby number, $Ro = U/fW$, to obtain

$$(\frac{\partial}{\partial t} + \boldsymbol{u}_j \cdot \nabla)\ (\zeta_j - \frac{fh_j}{H_j}) \ = \ 0 \tag{2.18}$$

to first order, where ζ_j is the relative vorticity in the jth layer, h_j is the layer thickness, and H_j is the mean layer thickness. That is, fractional errors in neglecting higher order terms are of order Ro.

Using the hydrostatic relations for pressure, and the geostrophic along-channel current as the mean, the solution to the linearised perturbation form of the potential vorticity equation in each layer is found to be proportional to

$$\sin(n\pi y/W)e^{ik(x-cUt)} \tag{2.19}$$

where k is the wavenumber, cU the phase speed, and y/W the non-dimensional cross-channel distance. The parameter c satisfies the quadratic relation

$$(1 + \frac{\lambda^2}{\alpha_1} - \frac{1}{(1-c)})(1 + \frac{\lambda^2}{\alpha_2} - \frac{1}{c}) \ = \ 1 \tag{2.20}$$

where $\lambda = k^2 + n^2\pi^2/W^2$ and $\alpha_j = f^2/(g'H_j)$, and has imaginary roots if $4\alpha_1\alpha_2 \geq \lambda^4$. The smallest value of λ occurs when $n = 1$ and $k = 0$. The instability criterion then becomes

$$W^2 \geq \frac{\pi^2}{2}\frac{g\Delta\rho}{\rho_o}\frac{\sqrt{H_1 H_2}}{f^2} \tag{2.21}$$

and with $H_1 \approx H_2 \approx H/2$ and $N^2 \approx g\Delta\rho/\rho_o/(H/2)$, the requirement becomes $W \geq (\pi/\sqrt{8})NH/f$, identical to that of the geometric argument, aside from the factor $\pi/\sqrt{8}$.

b) Continuous Stratification

Eady (1949) considered the stability of a quasi-geostrophic flow to baroclinic instability for a continuously stratified fluid. The conservation of quasi-geostrophic vorticity equation can be written as

$$\left(\frac{\partial}{\partial t} + U_o\frac{\partial}{\partial x}\right) q_g = 0, \qquad \text{with} \qquad q_g = \frac{\partial^2\psi}{\partial x^2} + \frac{\partial^2\psi}{\partial y^2} + \frac{\partial}{\partial z}\left(\frac{f_o^2}{N^2}\frac{\partial\psi}{\partial z}\right) + \beta y \tag{2.22}$$

where $\boldsymbol{U} = (U_o, 0, 0)$ is the background geostrophic flow, ψ is the perturbation stream function, and $f = f_o + \beta y$ is the β-plane approximation to the Coriolis force. The boundary condition for no vertical flow at the boundaries is

$$\left(\frac{\partial}{\partial t} + U_o\frac{\partial}{\partial x}\right)\frac{f_o}{N^2}\frac{\partial\psi}{\partial z} - \frac{f_o}{N^2}\frac{\partial U_o}{\partial z}\frac{\partial\psi}{\partial z} = \frac{-N^2 w}{f_o} = 0 \tag{2.23}$$

at $z = 0$ and $z = H$, while that for no transverse flow at the sidewalls is $v = \partial\psi/\partial x = 0$ at $y = 0$ and $y = W$. Considering disturbances of the form $\psi = \Phi(y)\Theta(z)e^{i(kx-\omega t)}$, the latter condition requires that $\Phi(y) = \sin(n\pi y/W)$. Setting the potential vorticity to zero, ignoring the β effect, and using a constant stratification implies $\Theta(z) = A\cosh(\gamma z) + B\sinh(\gamma z)$, where $\gamma = \sqrt{k^2 + n^2\pi^2/W^2}\,N_o/f_o$. Finally, with $U_o = 0$ at $z = 0$ and for constant $\partial U_o/\partial z = U_z$, the boundary condition of no vertical current at the top and bottom requires that

$$\omega = \frac{U_z kH}{2}\left(1 \pm \sqrt{1 - \frac{4\coth(\gamma H)}{\gamma H} - \frac{4}{(\gamma H)^2}}\right) \tag{2.24}$$

The frequency must have an imaginary component for instability to occur and for $n = 1$ and $k = 0$ this requires

$$W \geq \frac{\pi}{2.4}\frac{NH}{f} \tag{2.25}$$

which, aside from a factor $\sqrt{8}/2.4$, is identical to the result for the two layer flow. Flows in a channel of a given width are therefore more susceptible to baroclinic instability with decreased stratification, shallower depths, and at higher latitudes.

2.4 Tides

Tides are caused by the difference between the gravitational forces of the moon-sun-Earth system and the centrifugal forces resulting from the rotation of these bodies around their common centre of mass. While the vertical component of the tidal force is negligible relative to the Earth's gravity, the horizontal component is comparable in magnitude to other horizontal forces acting on the ocean, such as wind stress. The resulting disturbances travel as surface longwaves (i.e. with wavelength much larger than the water depth).

Surface gravity waves of the form $e^{i(kx-\omega t)}$ in a rotating homogeneous fluid of constant depth H must satisfy the dispersion relation $\omega^2 = g\gamma \tanh(\gamma H)$, where ω is the wave frequency and γ is related to the horizontal wavenumber k by $k^2 = \gamma^2 - R^{-2}\gamma H \coth(\gamma H)$ (Gill 1982). The Rossby radius of deformation, $R \equiv \sqrt{gH}/f$, is the horizontal length scale at which rotation effects become important. That is, for $k^{-1} = \lambda/2\pi \ll R$, $k \approx \gamma$, and the dispersion relation reduces to that of the non-rotating case $\omega^2 = gk\tanh(kH)$. On the other hand, when $k^{-1} \gtrsim R$, $k^{-1} \gg H$ (since $H \ll R$ in the ocean), and with $\gamma^2 \approx k^2 + R^{-2}$, the dispersion relation simplifies to

$\omega^2 = f^2 + k^2c^2$, with $c = \sqrt{gH}$ the wave speed in the absence of rotation effects. These waves, known as Poincaré waves, take the form

$$\begin{aligned} \eta &= \eta_o cos(kx - \omega t) \\ u &= \frac{\omega \eta_o}{kH} cos(kx - \omega t) \\ v &= \frac{f \eta_o}{kH} sin(kx - \omega t) \\ w &= -\omega \eta_o sin(kx - \omega t) \end{aligned} \tag{2.26}$$

where η is the surface elevation. The horizontal velocity vector rotates anticyclonically, tracing an ellipse of relative axes lengths of ω and f parallel and perpendicular to the direction of propagation, respectively.

2.4.1 Tides in Channels

Away from the coast, tidal currents are generally less than 0.1 m s^{-1} and tidal elevations are also small. However, boundaries impose restrictions on the flows: near the coast, tidal currents easily reach speeds of several metres per second, and tidal amplitudes of several metres are common. The relative magnitudes and phases of the tidal constituents determine these local flow fields and elevations and, while they are constant in time, they vary with location, depending on the local topography.

Tides within semi-enclosed basins are made up of the independent tide, the result of tidal forcing on the water within the basin itself, in addition to the sympathetic tide, that imposed on the basin by the oceanic tide. In most small basins, the independent tide is negligible relative to the oceanic forcing.

Although individual Poincaré waves cannot satisfy the boundary condition of zero normal flow at a coast, combinations can. In particular, for a uniform channel of width W, the superposition of two Poincaré waves of wavevector $\boldsymbol{k}_1 = (k, l)$ and $\boldsymbol{k}_2 = (k, -l)$ and of equal amplitude satisfy the boundary condition $v = 0$ at $y = 0, W$ provided that the cross-channel wavenumber $l = m\pi/W$ for non-zero integer m. The

dispersion relation is $\omega^2 = \omega_c^2 + k^2 gH$, where k is the along-channel wavenumber, and

$$\omega_c^2 = f^2 + l^2 gH = f^2(1 + m^2\pi^2 R^2/W^2) \tag{2.27}$$

is the minimum frequency allowed. For narrow channels (i.e. $W \ll R$) ω_c becomes large, and Poincaré waves at tidal frequencies cannot exist. Barotropic tidal waves containing cross-channel velocity components which may exist in the open ocean are therefore evanescent within the channel.

Kelvin waves, with $v \equiv 0$ everywhere, also satisfy the boundary conditions, and have the form (Gill 1982)

$$\begin{aligned} \eta &= \eta_o e^{-y/R} \cos(kx - \omega t) \\ u &= \sqrt{g/H}\,\eta_o e^{-y/R} \cos(kx - \omega t) \\ w &= \omega \eta_o e^{-y/R} \sin(kx - \omega t) \end{aligned} \tag{2.28}$$

where R is again the Rossby radius of deformation. These edge waves travel with the coast on the right (in the Northern hemisphere) and have amplitudes which decay exponentially with distance from the coast.

Tidal amplitudes can grow to be very large when tidal periods closely match the resonant period of the basin. For a rectangular channel of length L which is open to the ocean at one end, the resonant period is given by $T \approx 4L/\sqrt{gH}$, where g is the gravitational acceleration, and H is the water depth. Resonances can also occur in the cross-channel direction; the resonant period for a channel of width W, where both ends are closed, is $T = 2W/\sqrt{gH}$. In a simple channel of length, width, and depth on the order of those of Juan de Fuca Strait, these resonant periods are approximately four hours and 15 minutes, respectively.

For channels of finite extent where one end is closed (representative of a simple estuary), Kelvin waves of tidal frequency enter from the ocean and are reflected at the opposite end, following the boundaries of the channel in a cyclonic sense. At

the closed end. Poincaré waves are generated to satisfy the boundary condition of no normal flow. Oceanic Poincaré waves also enter the channel from the open end. In narrow channels, the magnitudes of these Poincaré waves decay quickly with distance from the source regions. However, transverse currents of significant magnitude are not precluded at tidal frequencies in "real" (i.e. stratified) channels due to the presence of baroclinic tides.

2.4.2 Internal Tides

Just as surface waves exist on the boundary between ocean and atmosphere, waves on the boundary between water masses can be found within the fluid. Much smaller interior density differences support waves of significantly larger amplitude. Internal waves also have greater wavelengths and smaller phase speeds than those on the surface.

Although the processes which cause them are not fully understood, a variety of mechanisms throughout the water column have been examined. At the surface, these include travelling atmospheric pressure fields, space-time variations in the wind stress field (leading to pumping), moving buoyancy fluxes due to precipitation and solar heating, and resonant interaction of surface gravity waves. Penetrative convection (Stull 1976) and geostrophic adjustment (Rossby 1938; Blumen 1972) are known to generate internal waves in the atmosphere and may also be important in the ocean interior. The large amplitudes of internal tides over the continental shelf and slope have inspired a great deal of study of flow over topography, in particular of the barotropic tidal current over the continental shelf and slope. Estuaries, especially those with strong tides and sills, are also strong generation regions owing to irregular and shoaling bathymetry. Passing over a step-like shelf, for example, a barotropic tide generates internal tides (i.e. of the same frequency) which are both reflected back into the ocean and transmitted landward.

Internal waves in a two-layer system are restricted to propagate horizontally along the interface, with velocities and amplitudes decaying with distance from the

interface to zero at the bottom and to nearly zero at the surface. In a continuously stratified medium, internal waves whose wavelengths are small compared to the water depth are able to propagate in directions other than the horizontal, transferring energy throughout the water column. However, internal waves of long wavelength, such as baroclinic tides, feel the boundaries, and vertical velocities at the free surface and bottom must again vanish. Furthermore, the boundary conditions restrict the vertical wavenumber to discrete values for fixed frequency and stratification. For each of these vertical wavenumbers there is a corresponding vertical profile, or mode, of the wave amplitude.

In an infinitely long channel of constant rectangular cross-section with width sufficiently narrow that transverse currents are everywhere zero, solutions to the inviscid linear momentum equations for waves of the form $e^{i\omega t}$ are known as internal Kelvin waves and are given by (Defant 1961)

$$\begin{aligned} \eta &= \hat{\eta}(z)\, e^{-y/R_n} \cos(\omega t - kx) \\ u &= \frac{\omega}{k} \frac{\partial \hat{\eta}(z)}{\partial z} e^{-y/R_n} \cos(\omega t - kx) \\ v &= 0 \\ w &= \omega\, \hat{\eta}(z)\, e^{-y/R_n} \sin(\omega t - kx) \end{aligned} \tag{2.29}$$

with η the displacement, and $\hat{\eta}(z)$ the vertical dependence. Here $R_n \equiv c_n/f$ is the internal Rossby radius of deformation for the n^{th} vertical mode, where c_n is the corresponding phase speed.

Defant (1961) also showed that combinations of internal Poincaré modes which satisfy the boundary condition $v = 0$ at $y = 0$. W take the form

$$\begin{aligned} \eta &= \left(\sin(\alpha y) - \frac{\omega\alpha}{kf} \cos(\alpha y) \right) \hat{\eta}(z) \cos(\omega t - kx) \\ u &= \left(\frac{\omega}{k} \sin(\alpha y) - \frac{\alpha}{f} \frac{\omega^2 - f^2}{k^2 + \alpha^2} \cos(\alpha y) \right) \frac{\partial \hat{\eta}(z)}{\partial z} \cos(\omega t - kx) \\ v &= \frac{f^2 k^2 + \omega^2 \alpha^2}{fk(k^2 + \alpha^2)} \sin(\alpha y) \frac{\partial \hat{\eta}(z)}{\partial z} \sin(\omega t - kx) \end{aligned} \tag{2.30}$$

with $\alpha = m\pi/W$ for non-zero integer m. Fjeldstad (1935) showed that $\eta(z)$ in both types of waves satisfies

$$\frac{d^2\eta(z)}{dz^2} + \frac{N^2 - \omega^2}{c_n^{\,2}}\eta(z) = 0 \qquad (2.31)$$

subject to the boundary conditions $\eta(0) = \eta(H) = 0$, and that the wavenumbers are given by $k_n = \omega/c_n$ for internal Kelvin waves and

$$k_{nm}^2 = (\omega^2 - f^2)/c_n^2 - \alpha_m^2 \qquad (2.32)$$

for internal Poincaré waves, where the latter are possible only for $\omega > f$ and for real k_{nm}. For the barotropic mode (i.e. $n = 0$), where $c_0^2 = gH$, real k_{0m} implies that the minimum frequency is given by (2.27). At a latitude of 49°, for example, representative of both Juan de Fuca Strait and the St. Lawrence River, internal Poincaré modes are not possible at diurnal frequencies ($\omega < f$), and these tides must be comprised only of barotropic and baroclinic Kelvin waves. Although the $\omega > f$ criterion is satisfied for semidiurnal frequencies, not all combinations of vertical and lateral modes are permitted (i.e. k_{nm} is not real).

Using hydrography data from the St. Lawrence River, Forrester (1974) found that no internal Poincaré modes for $n = 1$ (i.e. the first internal mode) were allowed and that only the first lateral mode ($m = 1$) was possible for $n = 2$. He used a string of along- and cross-channel current meters to measure the tidal magnitudes, determined the best fit wavenumber to the data, and compared these to the previous theoretical results. For both the along- and cross-channel magnitudes and phases, the baroclinic $M2$ tide is very well represented by a seaward propagating Poincaré type wave of second vertical and first lateral mode. Although the results for the measured diurnal constituents were not as conclusive, he found a peak in the wavenumber near that predicted for a Kelvin wave of the first vertical mode.

Forrester (1974) noted that the short wavelength of internal modes means both that observed tidal currents can change rapidly over short distances in the horizontal

and vertical directions and that there "must be relatively strong convergence and divergence between the crests and troughs." He further remarked that seasonal changes in the tides might be significant owing to the sensitivity to N^2 in (2.31).

However, Forrester (1974) did not consider the effect that background currents have on both the shape and propagation of internal waves. For a mean flow of $\boldsymbol{U} = (U(z), 0, 0)$ and perturbation velocity $\boldsymbol{u}' = (u', v', w')$, the "non-linear" terms involving the mean flow and perturbation quantities in the inviscid perturbation momentum equations

$$\begin{aligned} u'_t + Uu'_x + U_z w' - fv' &= -p'_x/\rho_o \\ v'_t + Uv'_x + fu' &= -p'_y/\rho_o \\ w'_t + Uw'_x + g\rho'/\rho_o &= -p'_z/\rho_o \end{aligned} \tag{2.33}$$

and in the conservation of mass and continuity equations

$$\begin{aligned} \rho'_t + U\rho'_x + \rho_{oz} w' &= 0 \\ u'_x + v'_y + w'_z &= 0 \end{aligned} \tag{2.34}$$

are retained. These five equations in five unknowns (u', v', w', ρ', p') are solved for arbitrary $U(z)$ and $\rho_o(z)$.

Using the non-rotating ($f = 0$), two-dimensional ($v' \equiv 0, \partial/\partial y \equiv 0$), non-hydrostatic (i.e. retaining all terms in the w-momentum equation) form of these equations, and again employing the separation of variables technique, the z dependence of $w' = w(z)\, e^{ik(x-ct)}$ is found to satisfy the relation

$$\frac{\partial}{\partial z}\left(\rho_o (U-c)\frac{\partial w}{\partial z}\right) - \frac{\partial}{\partial z}\left(\rho_o \frac{\partial U}{\partial z} w\right) - \left(\rho_o k^2 (U-c) + \frac{g\partial\rho_o/\partial z}{(U-c)}\right) w = 0 \tag{2.35}$$

which is known as the non-Boussinesq form of the Taylor-Goldstein equation. Using the chain rule this can be written as

$$w_{zz} + \rho_{oz}/\rho_o \, w_z - \left(\frac{U_{zz} + U_z \rho_{oz}/\rho_o}{(U-c)} + k^2 + \frac{g\rho_{oz}/\rho_o}{(U-c)^2} \right) w = 0 \tag{2.36}$$

where differentiation with respect to z is denoted by a subscript. The Boussinesq form is obtained by ignoring vertical differences in the reference density, ρ_o, except where they are multiplied by gravity, g. Using the Boussinesq approximation, and for mean flow $U \equiv 0$, (2.36) reduces to (2.31). The vertical structure of the tides given by the Taylor-Goldstein equation with and without background flow is compared in Chapter 6, where the theoretical modes are fit to the measured tidal amplitudes.

Chapter 3

Juan de Fuca Strait

Juan de Fuca Strait (Figure 3.1) is a 160 km long estuarine channel, approximately 22 km wide and 200 m deep in the central section, increasing to 40 km wide and about 250 m deep at the western end. It is oriented in a WNW-ESE direction, is fairly straight, and has relatively smooth bathymetry, except for a sharp northward turn at the eastern end. There is also a sill, south of Victoria, which extends across most of the strait at a depth of less than 100 m. Off the western end, a submarine canyon oriented to the southwest drops to over 300 m depth within 30 km of the coast, allowing deeper Pacific Ocean water into the lower depths of the strait.

3.1 Background

Juan de Fuca Strait is the principal outlet for the Strait of Georgia and Puget Sound, and thus for most of the precipitation falling over much of southern British Columbia and northern Washington State. The river runoff into this three-basin system is highly seasonal in nature, varying from about 5,000 $m^3 s^{-1}$ in winter to 25,000 $m^3 s^{-1}$ during the summer freshet (from snow melt in the mountains), which usually reaches a maximum in June, although there is considerable inter-annual variation in both the magnitude and timing of this peak. Fraser River discharge (Figure 3.2) is the major contributor to this buoyancy input, especially during the freshet, when it accounts for about 50% of the total freshwater forcing (Griffin and LeBlond 1990). There is also river runoff directly into Juan de Fuca Strait, mostly from western Vancouver Island during the heavy winter rains; averages of 500 $m^3 s^{-1}$ are estimated (LeBlond *et al.* 1983). Jordan River is one of the larger sources in the middle section of the strait under consideration.

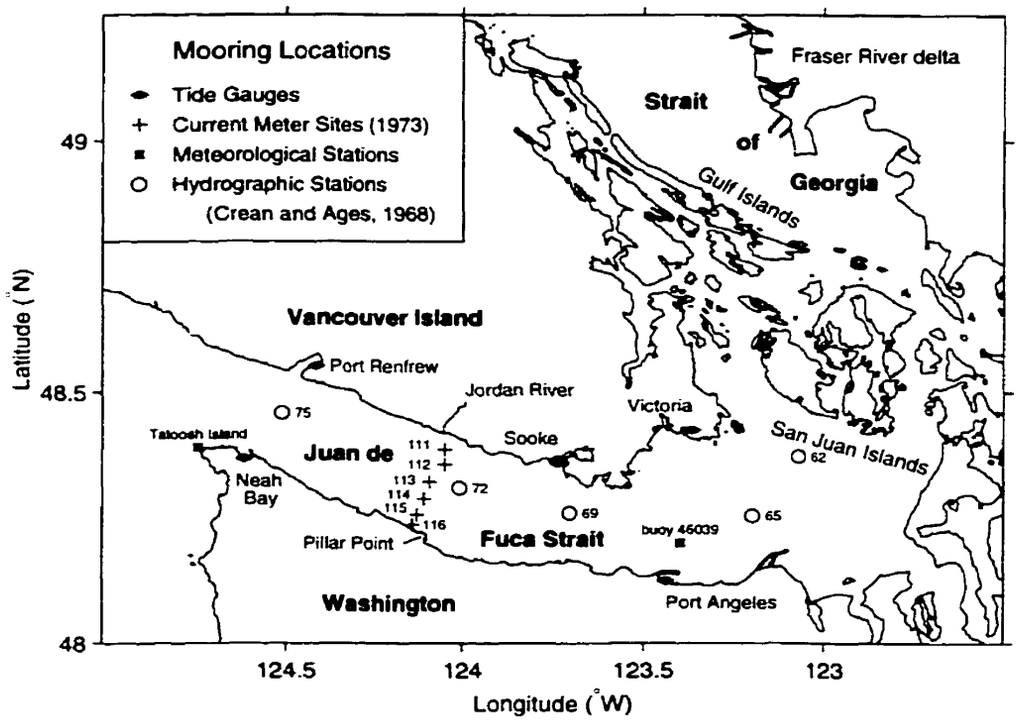

Fig. 3.1. Geography of Juan de Fuca Strait and the Strait of Georgia with hydrographic, meteorological, sea level gauge, and current meter sites.

Tidal currents in Juan de Fuca Strait are particularly strong in the shallow constrictions around the Gulf Islands and the San Juan Islands, where vigorous mixing of salty Pacific Ocean water and brackish Fraser River outflow occur. Downstream, in central Juan de Fuca Strait, flows are not as vigorous, although maximum horizontal currents still reach 1.8 m s^{-1} during spring tides, with rms tidal speeds of about 0.5 m s^{-1} typical within the strait. The tides are comprised mainly of strong diurnal and semi-diurnal components; Holbrook *et al.* (1980) found that 65% to 88% of the variance in the along-channel flow could be accounted for by just these constituents.

Buoyancy input into Juan de Fuca Strait itself is largest during neap tides, when vertical mixing in the islands is reduced. Griffin and LeBlond (1990) state that this mixing region acts as a periodic barrier separating Juan de Fuca Strait from the Strait of Georgia, "because the vertical exchange of momentum (during spring

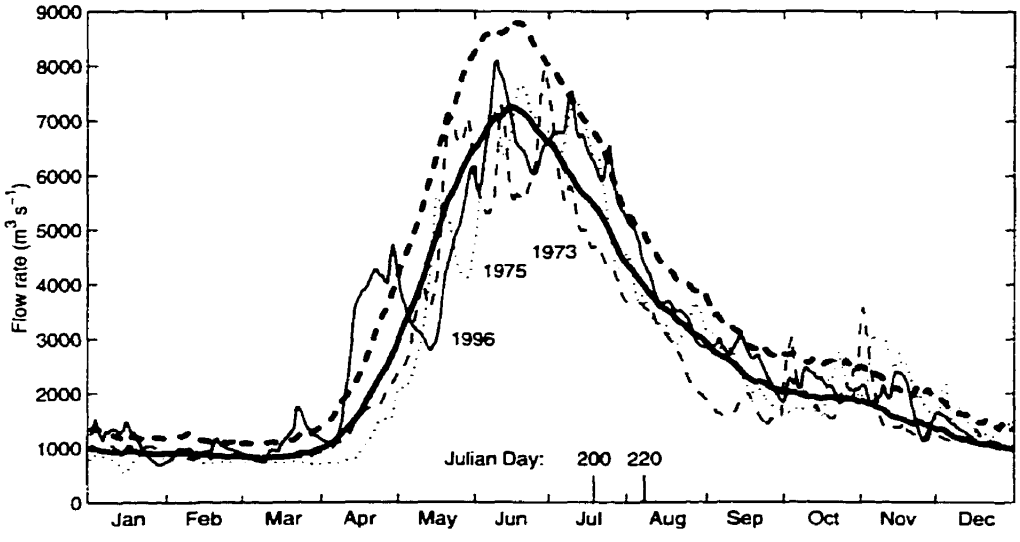

Fig. 3.2. The seasonal cycle in the volumetric flow of the Fraser River, as measured at Hope. The thick solid line is the mean and the thick dashed line is the mean plus standard deviation over the years 1912 to 1996. The freshwater input into the Strait of Georgia is about 30% larger than the amount measured at Hope.

tides) inhibits the sheared flow that would commence if mixing were to cease." The spring-neap cycle is reduced in strength in autumn and spring due to the smaller solar declinational tide, and Fraser River runoff is largest in summer, so the greatest fluctuations of buoyancy input into Juan de Fuca Strait should occur in early summer, particularly when northwesterly winds occur in the Strait of Georgia. Using surface salinity records between 1967 and 1985, Griffin and LeBlond (1990) show that salinity fluctuations at Race Rocks are indeed greatest in the summer, and that more than 47% of the variance can be accounted for by the M_m (period 27.55 days), and MS_f (14.76 days) components. The M_m and MS_f frequencies are shallow-water components, resulting from non-linear interactions between the $M2$ and $N2$, and $M2$ and $S2$ components, respectively.

Mean winds in Juan de Fuca Strait are along the channel about 30% of the time throughout the year (Thomson 1981), constrained by the mountain ranges near the coast on both sides of the strait. These blow toward the ocean during the fall

and winter, and landward during the summer. This seasonal difference is related to the atmospheric pressure systems that dominate the North Pacific Ocean: the North Pacific High during the summer, and the Aleutian Low in winter. Winds are generally stronger in winter and in the western part of Juan de Fuca Strait. At Tatoosh Island (Figure 3.1), winds exceed 8.5 m s^{-1} about 40% of the time from November through January, and less than 10% from May through August, while at Port Angeles, winds exceed 8.5 m s^{-1} about 5% in the winter and nearly 10% in June and July. The COADS (DaSilva *et al.* 1995) up- and cross-channel (positive toward Vancouver Island) surface wind stresses vary from -0.025 and $+0.05$ N m^{-2}, respectively, in winter, to $+0.03$ and -0.015 N m^{-2} in July.

Offshore winds and pressure systems also affect the circulation within Juan de Fuca Strait. Holbrook *et al.* (1980) found that subtidal motions were highly correlated with the forcing of large scale coastal winds, and not with winds within Juan de Fuca Strait. Northward coastal winds due to occasional passing storms drive an onshore Ekman transport, leading to surface intrusions of Pacific water into the strait. In winter, coastal winds are generally northward; this can reverse the sea surface slope and lead to a reversal in the estuarine circulation (Holbrook and Halpern 1982). In summer, coastal winds are from the northwest and drive coastal upwelling, bringing colder, saltier water from the continental shelf into Juan de Fuca Strait at depth. Crean and Ages (1971), for example, found that the mean salinity below 80 m depth at Station 72 (Figure 3.1) was approximately 33.5 psu in July compared to 33 psu in January of 1968.

The fresh water input is also greater in summer due to the freshet ($Q_f \approx 1.8 \times 10^4$ m^3 s^{-1} compared to 0.3×10^4 m^3 s^{-1} in winter). However, the mean salinity in the upper layer (i.e. above 80 m) is similar (Crean and Ages (1971) found a mean salinity of approximately 31 psu in both January and July), implying greater entrainment into the upper layer. The net result is that exchange rates are much larger in summer. While strictly valid only for two-layer flow, the Knudsen relations (2.2) suggest that for the July conditions, $Q_1 \approx 0.3$ Sv, where 1 Sv (Sverdrup) $\equiv 10^6$ $m^3 s^{-1}$.

Using data from a string of current meters across Juan de Fuca Strait from May 16 to July 15, 1975, Labrecque *et al.* (1994) found a volume flux of 0.27 Sv. In winter, on the other hand, $Q_1 \approx 0.06$ Sv. While the amount of deep water entrained into the upper layer ($Q_1 - Q_f$) was about five times larger in July, the surface was fresher (30.5 psu compared to 31 in January). Greater buoyancy forcing in the summer inhibits mixing near the surface, resulting in larger stratification in the upper layer.

Partly due to these seasonal differences, there has historically been some debate as to which type of estuary Juan de Fuca Strait is. Although generally thought to be a partially-mixed estuary, Dyer (1973) considers it a straight, deep fjord, while Stommel (1952) states that it does not fall into any of the main categories. In the summer, the estuarine Richardson number (2.1) is $Ri_e \approx 2$, well above the transition region from well-mixed to strongly stratified. In winter, on the other hand, $Ri_e \approx 0.5$, which classifies Juan de Fuca Strait as a partially mixed estuary. Using the two non-dimensional parameters (Section 2.1.1) proposed by MacCready (1999), the densimetric Froude number $F_m \approx 10^{-3}$ in summer and about one-fifth that in winter, while the Froude number $\Gamma \approx 0.1$ during both seasons. This places Juan de Fuca Strait in the parameter space for which the up-estuary salt flux is dominated by the exchange flow. That is, the diffusive fraction of the up-estuary salt flow is slightly greater than 0.1 in winter, and less than 0.1 in summer, implying that Juan de Fuca Strait is a partially-stratified to well-stratified estuary.

Indeed, rather than being an area of significant vertical mixing, Juan de Fuca Strait may be a region in which restratification occurs. Tidal currents are much stronger and water depths are smaller around the islands in the eastern portion of the strait, and one would expect a well-mixed condition to exist there. Mixing in the middle of Juan de Fuca Strait is not as effective and the density of the brackish water exported from the Strait of Georgia remains fairly constant throughout Juan de Fuca Strait (Figure 3.3). Any increase in stratification would act to further reduce instability mixing at the inflow/outflow interface, reinforcing stratification. Density

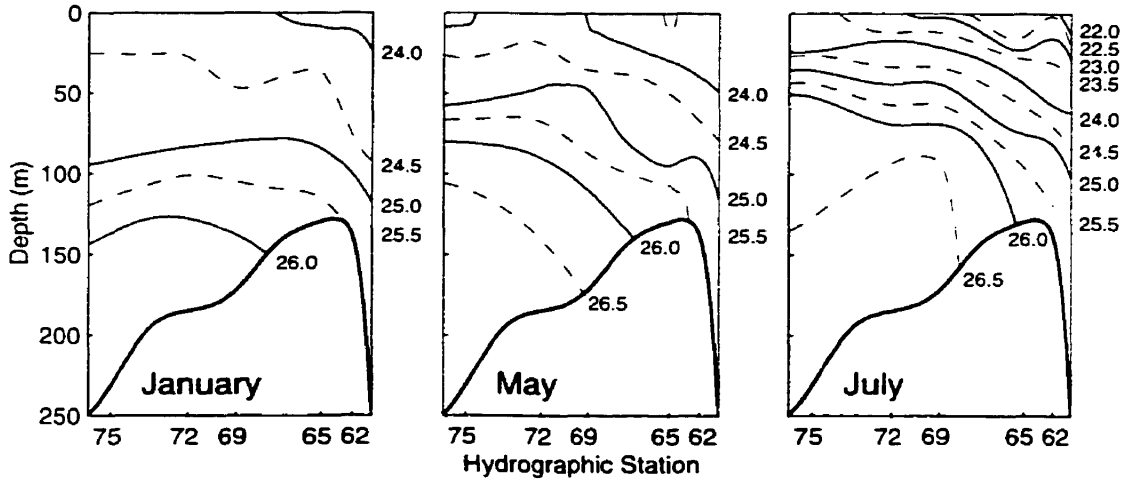

Fig. 3.3. Mid channel density (σ_t, in kg m^{-3}) along Juan de Fuca Strait in January, May, and July (Crean and Ages 1971).

profiles (Figure 3.3) seem to suggest a slight tightening of the pycnocline from mid-strait to the mouth.

The July profile suggests that there is also significant entrainment into the lower layer, contrary to the picture of one-way entrainment for highly-stratified estuaries (Dyer 1973). Were entrainment into the lower layer to exceed that into the upper layer, the volume transport would decrease toward the mouth. Current meter data (Labrecque *et al.* 1994) at the middle and mouth of the strait from 1975 and 1984, respectively, indicate that the volume flux decreased from 0.27 Sv to 0.16 Sv at the mouth. However, the 1984 currents are means over the period from June 20 to November 25, while those of 1975 are means over the period from May 26 to July 15. Although the volumetric Fraser River discharge is very similar for 1975 and 1984 between early June and late November, the freshwater input drops about 70% over that time, which should result in a much weaker estuarine circulation. Concurrent measurements at mid-strait and at the mouth of Juan de Fuca Strait are needed to determine whether recirculation is indeed occuring within the strait.

Labrecque *et al.* (1994) also found tilts in the interface, which they defined as the level of zero mean along-channel motion, between the upper and lower layers. In the along-channel direction, the interface on the central axis of the channel was found at a depth of 75 m in the middle of the channel and 65 m at the mouth. The interface slanted in the cross-channel direction, from 70 m depth at the southern side to over 90 m at the northern side, consistent with the Coriolis force.

Fissel (1976) examined the feasibility of using bottom pressure measurements to determine currents flowing through Juan de Fuca Strait, both for the dominant tidal currents and for the smaller low frequency residual currents. For the total current, he found that cross-strait pressure differences and average along-strait currents were well correlated and that the "gain" agreed with the theoretical value $\rho f W$ (with W the channel width), within experimental accuracy ($\pm 20\%$ of along-strait speed). At both 20 and 120 m depth, 80% of the variance in average along-strait speeds could be determined from the pressure records. For the residual currents (low-pass filtered with a cut-off frequency of 0.8 cycles per day), correlation between currents and pressure differences at 120 m depth was found to be poor; Fissel (1976) attributed this to the inaccuracy of the pressure gauges and inadequate spatial sampling of the currents. At 20 m depth, correlation coefficients ranged from 0.75 to 0.93, although the measured "gain" was 18% to 42% lower than the theoretical value. This reduction may be the result of reduced currents due to sidewall friction. He also noted that the residual currents at each depth were poorly correlated with one another (the current meter separation was typically 4 km).

Numerical models may be of benefit in answering some of the questions surrounding cross-channel flow by providing some ideas about the along-channel evolution. Masson and Cummins (1999) used the Princeton Ocean Model (POM) without tidal forcing to examine the role of buoyancy forcing in the dynamics of the summer coastal countercurrent found off the west coast of Vancouver Island. They found that the coastal current is driven by a barotropic pressure gradient at the mouth of Juan de Fuca Strait due to the outflow of brackish water from the channel. Bottom

friction and a baroclinic pressure gradient act to transform the coastal current into a surface-intensified flow.

Masson and Cummins (1999) examined the possible effects of enhanced vertical mixing due to tidal effects by increasing the vertical coefficients of viscosity and diffusion over the sill south of Victoria above the background values found elsewhere in the Strait of Georgia - Juan de Fuca Strait basin. They note that although the coastal current away from the mouth of the strait is largely unaffected, hydrography within Juan de Fuca Strait is changed considerably. Unfortunately, no details of the interior flow within the strait for either the nominal or enhanced mixing cases were reported, although at the mouth both the spatial structure of the estuarine flow as well as the volume flux of brackish water compare well with observations.

Motivated by data which reveal the presence of fortnightly freshwater pulses both within Juan de Fuca Strait (Griffin and LeBlond 1990) and in the coastal current itself (Hickey *et al.* 1991), a later study (Masson and Cummins 2000) examined the effects of a spring-neap cycle in tidal mixing over the Victoria sill and in Haro Strait. They were able to reproduce both the magnitude of the spring-neap cycle in the surface salinity at Race Rocks, about 1 psu, and its phase relative to the tide, with lowest salinities occuring 2 days after neap tide. Masson and Cummins (2000) showed that the volume transport across the central section of Juan de Fuca Strait is largest approximately two days after neap tide and smallest after springs, with a fortnightly modulation of nearly 20% of the mean.

The model results also suggest that mixing within Juan de Fuca Strait itself is larger during neap tide (Patrick Cummins, personal communication, 2000), likely due to the larger shears associated with the increase in estuarine exchange. In the following section, a momentum balance based in historical data suggests that friction is indeed large at the interface, motivating the further examination of mixing over a spring-neap cycle.

3.2 A Preliminary Analysis

The estuarine flow in Juan de Fuca Strait is highly seasonal in nature, as evidenced both by current meter data and hydrographic surveys. In the summer, when the exchange is largest, friction between the layers and along the bottom should be significant, leading to large values of the vertical eddy viscosity and strong cross-channel flows. After examining historical current and sea surface pressure data, the vertical eddy viscosity is determined by vertically integrating the along-channel momentum balance over the top layer.

3.2.1 Reanalysis of Historical Data

In 1968, Crean and Ages (1971) made 12 monthly surveys of the hydrography of the waters surrounding Vancouver Island. Each survey lasted three days and measured salinity and temperature at 79 stations within Juan de Fuca Strait and the Strait of Georgia. Oxygen profiles were also recorded at 33 of these stations. There were 13 stations west of the Victoria sill, with parallel transects running down the central axis (Figure 3.1) and northern and southern sides of Juan de Fuca Strait. The central transect is taken as representative of the mean hydrographic conditions in the strait. Strong seasonality can be seen in the stratification (Figure 3.3).

a) Sea Level Data

Monthly average sea level data between 1982 and 1994 from Port Angeles and Neah Bay, both on the southern side of Juan de Fuca Strait, were used to determine the seasonal variation in sea surface height along the strait (Figure 3.4). Concurrent sea level records on the northern side of the strait were not of sufficient length. About one quarter of the along-channel pressure difference due to sea surface height ($\delta p_{sea} = g\rho_o \delta h_{sea} \approx 500$ Pa, for a sea level difference of $\delta h_{sea} \approx 0.05$ m) is offset by a difference in sea level atmospheric pressure. The atmospheric pressure difference δp_{atm} is from hourly measurements from Tatoosh Island and a buoy north of Port Angeles (Figure 3.1) over a two year period. The total surface pressure gradient

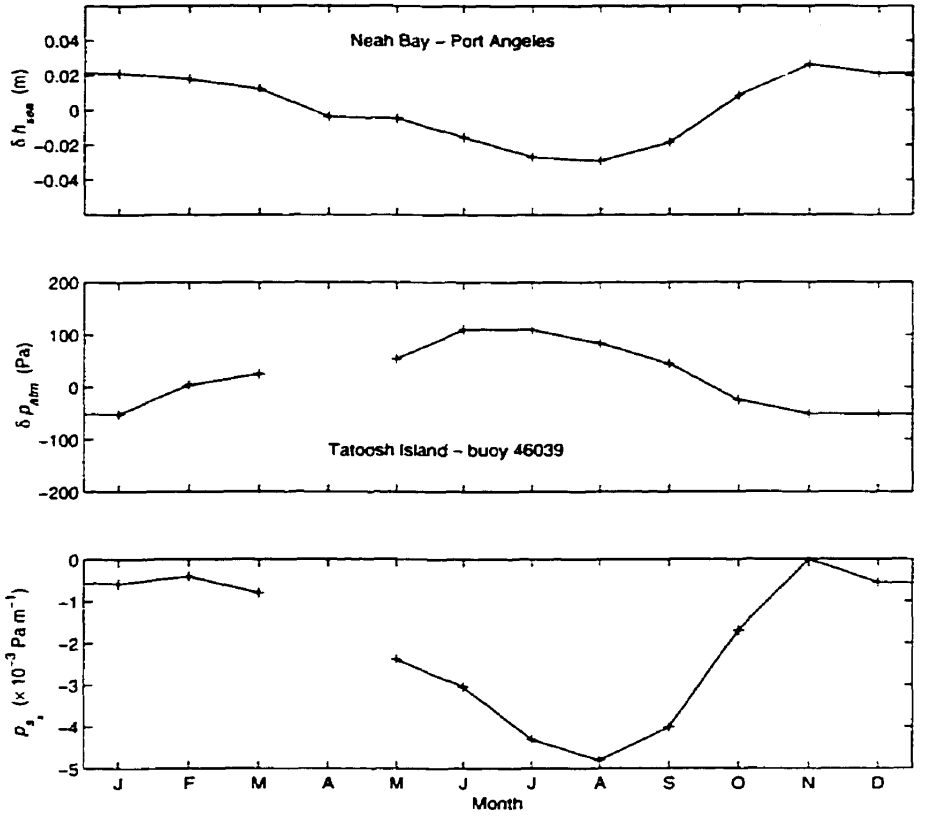

Fig. 3.4. Annual cycle of along-channel difference in mean tidal height, atmospheric pressure, and total surface pressure. The difference in the monthly average sea level height between Port Angeles and Neah Bay contains between 8 to 11 years of data from 1984 to 1992 for each month; the dotted line indicates the standard deviation. The atmospheric pressure difference uses hourly surface pressure values over a two year period. The net along-channel surface pressure gradient is assumed to be zero in November.

$p_{s_x} = \delta p_{sea}/D1 + \delta p_{atm}/D2$, with $D1 \approx 90$ km as the distance between the tidal gauges and $D2 \approx 100$ km as the distance between the meteorological stations, reaches a maximum in magnitude of $p_{s_x} \approx -5 \times 10^{-3}$ Pa m^{-1} in August if the total surface pressure gradient in the November is equal to zero (an assumption discussed later). The May surface gradient is about half that in August. This pressure gradient must be balanced by either lateral or internal friction.

b) Velocity Data

Current data were collected in two deployments: from March 6 to April 16 and from April 17 to June 14, 1973. The data for deployment 1 (hereinafter referred to as 73a) and deployment 2 (73b) were analysed separately, with mean dates (used in the comparison of hydrographic data) of March 27 and May 16, respectively. Each deployment consisted of six moorings across Juan de Fuca Strait (denoted by crosses in Figure 3.1), located halfway along the strait, roughly between Jordan River, British Columbia, and Pillar Point, Washington. The current meters were of two basic types, Anderaa recording current meters (RCM4) and Neyrpic current meter and direction recorders (CMDR), and were placed at depths of 15, 50, 100, and 150 m at each station, while some stations had additional current meters at 170 and 180 m depths. At certain depths, several of the stations recorded temperature, conductivity, and/or pressure as well.

There was some question regarding the reliability of the compass measurements, partly because, while the current speeds are ten minute averages of measurements taken every 30 s, the meters are non vector-averaging; the direction is measured only once every ten minutes. A tidal analysis of the horizontal current was performed at each depth independently and the magnitudes and relative phases of the along- and cross-channel tidal velocities were combined to form tidal ellipses for each tidal constituent. The major axes of these tidal ellipses were found to align well (within 2°) with the orientation of Juan de Fuca Strait, suggesting that the compass measurements are accurate.

In addition to occasions in which current meters ceased working or difficulties with saving data to tape occurred, the mooring arrays were known to experience a large amount of porpoising in strong currents due to the size and shape of the floats. This leads to significant tilts and large depth excursions, implying that the actual depths for strong currents are greater than the nominal depths of the instruments; unfortunately, pressure sensors were only attached to the bottom of the arrays. With along-channel flows generally decreasing with depth in the upper layer and increasing

with depth in the lower layer, the sensors at nominal depths of 50 m probably underestimated along-channel velocities, while currents at 100 m are likely overestimated. The effect on measured cross-channel flows is much harder to predict as not much is known about their vertical structure.

Overall and Tidal Currents

Current records for periods of longer than five days were used to calculate along-channel (u, positive seaward) and cross-channel (v, positive toward Washington State) velocity components. That is, the (x, y) axes are rotated 168° anticlockwise from $(east, north)$ to align with Juan de Fuca Strait. The $M2$ and $K1$ tidal constituents (with periods 12.4 and 23.9 hours, respectively) were found to be the largest components of the overall tidal current (with $K1$ about 60% as large as $M2$). The amplitudes generally decreased with depth.

Maximum overall speeds in the along-channel direction of between 1.0 and 1.5 m s^{-1} were found throughout the top 100 m at all locations, while deeper speeds never exceeded 0.8 m s^{-1}. Rms speeds were typically in the 0.5 to 0.6 m s^{-1} range in the upper 100 m, and between 0.2 and 0.4 m s^{-1} below that. In the cross-channel direction, maximum speeds were generally near 0.6 m s^{-1} on either side of the interface, and 0.3 to 0.4 m s^{-1} closer to the surface and bottom. Cross-channel rms speeds were relatively constant everywhere, about 0.1 m s^{-1}.

Residual velocities (Figure 3.5) were determined by averaging the detided currents. There is good agreement between the two deployments (73a and 73b) in the overall pattern and magnitudes of the flows in both the along- and cross-channel directions. Labrecque *et al.* (1994) used data from a similar study in 1975 between May 16 and July 15 (hereinafter referred to as 75, with a mean date of June 16). The line of five moorings in that survey was a little to the east of the 1973 line, but current measurements were made only at 20 and 120 m depths. They do not discuss cross-channel flows, but along-channel flows were similar to those of 1973.

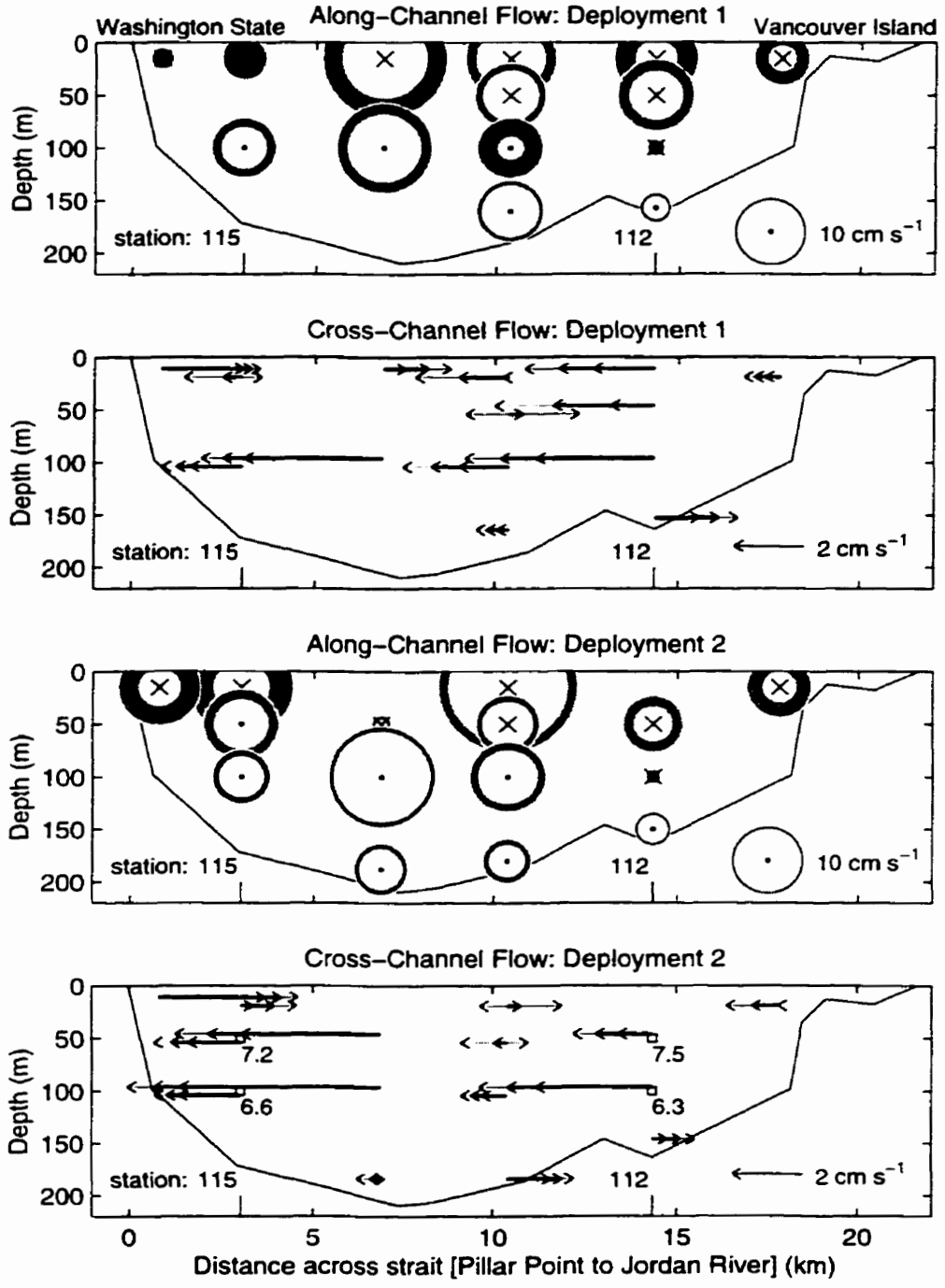

Fig. 3.5. Average, de-tided along- and cross-channel velocities in Juan de Fuca Strait based on 1973 deployments between Pillar Point and Jordan River (deployment 1: March 6 to April 16; deployment 2: April 17 to June 14). Standard deviations are indicated by the shaded regions for along-channel currents and by thin lines for cross-channel flows. The bottom panel also shows 32-day temperature averages (degrees Celsius), at locations marked with small squares, from records starting on 15 May, 1973.

Table 3.1. Seasonal Variability of the Mean Estuarine Flow in Juan de Fuca Strait

	March 6 - April 16 1973 (73a)	April 17 - June 14 1973 (73b)	May 16 - July 15 1975*
Maximum currents, m s^{-1}	0.15	0.18	0.24
Upper layer transport, Sv	0.12	0.15	0.27
Interfacial depth,† m	25-95	35-95	70-90
Measured $\Delta\rho$,‡ kg m^{-3}	1.0	1.5	3.0
Geostrophic Δu, m s^{-1}	-0.28	-0.36	-0.31
Measured Δu, m s^{-1}	-0.27	-0.33	-0.35

* Labrecque *et al.* (1994)

† cross-channel variation

‡ Crean and Ages (1968)

Along-Channel Residual Currents

Residual along-channel velocities (Figure 3.5) generally increased from the sides to the middle of the strait, with maxima for both the upper and lower layers occurring just south of the center, in agreement with the 1975 data. The interface (zero average along-channel flow) increased in depth from about 25 m on the Washington side to 80 m mid-strait and roughly 95 m on the north side for the 73a data; for the 73b data, the corresponding depths were roughly 35, 70, and 95 m. The cross-channel interfacial slope (for zero velocity) was steeper than that for the 75 data, where interfacial depths (based on linear interpolation between the two current meters to determine the level of zero along-channel flow) were 70 and 90 m on the south and north shores, respectively; earlier studies (Holbrook *et al.* 1980) had similar results.

Flatter cross-channel isopycnals are geostrophically consistent with slower along-channel flows. However, flows in June 1975 (with an overall outflow in the top layer of 0.27 Sv) were quite a bit larger than in the spring of 1973 (which had outflows

of 0.10 Sv, within about 30%, for both 73a and 73b). The differences between these data (summarised in Table 3.1) are due to the large increase in stratification from spring to summer as the Fraser River discharge increases. Integration of the thermal wind balance yields Margule's equation

$$f\,(u_2 - u_1) \;=\; -g'\,h_y \tag{3.1}$$

assuming that cross-channel isopycnal slopes equal the cross-channel interfacial slope h_y, with u_1 and u_2 the average velocities in the upper and lower layers, respectively, and $g' = g(\rho_2 - \rho_1)/\rho$ the reduced gravity. With $\rho_2 - \rho_1$ taken from along-channel density profiles (Crean and Ages 1971) as 1.0 kg m^{-3} (March), 1.5 kg m^{-3} (May), and 3.0 kg m^{-3} (June), predicted velocity differences between the upper and lower layers are -0.28, -0.36, and -0.31 m s^{-1} for the 73a, 73b, and 75 data, respectively. This agrees well with observed values (Table 3.1), given the poor resolution of the 75 data. In addition, the Crean and Ages (1971) stratification data do not allow for an evaluation of inter-annual variability. Though it has not been possible to obtain cross-channel sea surface slopes, it appears that the along-channel flow is in geostrophic balance.

Cross-Channel Residual Currents

The 1973 current meter data indicate that cross-channel flows in the northern half of the upper layer are generally southward, although the magnitude of the currents depends on the choice of along-channel direction. This direction is opposite to that of the expected geostrophic cross-channel velocity at the surface $v_g = p_{s_x}/f\rho_o$, with p_{s_x} the total along-channel surface pressure gradient (Figure 3.4). Assuming $p_{s_x} \approx 0$ in winter, $v_g \approx -0.02$ m s^{-1} (i.e. the geostrophic velocity is northward) at the surface in May (73b) and about half that in March (73a). Furthermore, observed upper layer along-channel isopycnal slopes (Figure 3.3) imply that the cross-channel geostrophic velocity should decrease as the interface is reached, while observations show that the largest cross-channel flows occur near the interface, reaching speeds of

over 0.06 m s^{-1}. This large southward flow is qualitatively consistent with an internal Ekman layer.

Below the interface, the cross-channel flow is also strong and to the south, although flows should be northward in an Ekman layer. One possible explanation for southward flowing water on both sides of the interface at the northern boundary is convergence of water in the sidewall Ekman layers, as discussed by Johnson and Ohlsen (1994). However, their results show that the water beneath the interface flows south for only a short distance (Figure 2.1) before meeting north-flowing water in the interfacial Ekman layer, where it is drawn down into the interior. As the closest current meters to the interface are at least 20 m below, it may be that the internal Ekman layer is missed, although this does not seem likely given the strong velocities seen. A more likely explanation is that mixing at the northern side raises the isopycnals in the upper layer, causing a cross-channel pressure gradient which, in the presence of internal viscosity, forces the newly formed water mass into the interior along the interface.

In the northern half of the Juan de Fuca Strait transect, there appears to be an overall cross-channel transport to the south, of about 3 m^3 s^{-1} per metre of coastline at Station 112, for example. This may be due to insufficient vertical resolution, or an overall movement of the water mass due to a bump in the side boundary. The Jordan River outflow, about 2 km downstream of this transect, is too small to have a significant effect.

3.2.2 Momentum Balance

Having seen that a simple geostrophic balance for the cross-channel flow does not seem to exist even in the interior of the upper layer away from sidewall and interfacial boundary layers, other terms in the along-channel momentum equation must be retained to balance the sea surface pressure gradient. The along- and cross-channel momentum equations are obtained by rotating the standard (east,north) axes for the Navier-Stokes relations (2.5) by 168° (i.e. clockwise) to align with the orientation of

Juan de Fuca Strait, so that (u, v, w) are positive in the out-channel, cross-channel (toward Washington State) and upward directions, respectively. The relative importance of the terms can then be determined by integrating the u-momentum equation over the basin width (W = 22 km) and upper layer depth (from the average interfacial depth of h_1 = 75 m to the sea surface) to obtain an area average.

The pressure term becomes $-h_1 W\overline{p_{1_x}}/\rho$, with $\overline{p_{1_x}}$ the average pressure gradient in the upper layer. A two-layer model would imply $\overline{p_{1_x}} = p_{s_x}$ (the surface pressure gradient), but the stratification in May (Figure 3.3) is approximately linear in the upper layer, implying an average pressure gradient of half the surface value since the pressure gradient reverses at the interface. The pressure term in the integrated u momentum equation then becomes $-h_1 W p_{s_x}/2\rho_o \approx 1.9$ m^3 s^{-2} for May. The other terms in the integrated equation are examined next.

The first term, u_t, disappears when using tidally averaged fields. The largest component of the second term is the Bernoulli-like $(h_1 W/2)\, \partial u^2/\partial x$. Using an along-channel flow $u = 0.1$ m s^{-1} for the area average and assuming that the change in u over the length of the straight section of the strait (L = 100 km) equals the current itself (which overestimates this term), the second term is at most 0.08 m^3 s^{-2}, more than an order of magnitude smaller than the pressure term. The third term is of the wrong sign: balancing the pressure term would require area average cross-channel speeds of -0.01 m s^{-1} (i.e. northward), while Figure 3.5 shows that upper layer cross-channel currents for deployment 2 (73b) are generally southward.

The first part of the fifth term, $h_1 W(A_h u_x)_x$, is dropped since along-channel variations in u are small; for a reasonable value of the horizontal eddy viscosity ($A_h \approx 10^2$ m^2 s^{-1}), this term is $< 10^{-2}$ m^3 s^{-2}. On integration across the strait, the second part of the fifth term becomes the sidewall friction and can be parameterised by $C_D\, u u_{\rm rms}\, 2h_1/s$, with $C_D \approx 0.0025$ as the drag coefficient and h_1/s as the sidewall length (s is the sidewall slope). Using $u = 0.05$ m s^{-1} for the average speed at current meters closest to the sidewalls, tidal $u_{\rm rms} = 0.5$ m s^{-1}, and $s \approx 0.08$, $C_D\, u u_{\rm rms}\, 2h_1/s \approx 0.1$ m^3 s^{-2}, about 5% of the pressure term.

The last term in the integrated u-momentum equation is $W(\tau_w/\rho_o - A_v u_{z\,int})$, representing the wind interfacial stresses. COADS (DaSilva *et al.* 1995) surface wind stress data for Juan de Fuca Strait suggest that the along-channel wind stress varies from -0.035 N m^{-2} in July to $+0.025$ N m^{-2} in December. In May $\tau_w \approx -0.025$ N m^{-2} and the wind stress term is ≈ -0.5 m^3 s^{-2}, about 25% of the surface pressure term. Balancing the interfacial stress term with the pressure and wind stress terms and using an interfacial shear of $+0.17$ m s^{-1} over 50 m implies a vertical eddy viscosity

$$A_v \approx \frac{-h_1 p_{s_x}/2\rho_o + \tau_w/\rho_o}{u_{z\,int}} \approx 0.02 \text{ m}^2 \text{ s}^{-1} \tag{3.2}$$

which is quite large and suggests significant friction between the outward bound surface layer and the deep return flow. Empirical formulae of the type

$$A_v = A_o F(\overline{Ri}) \tag{3.3}$$

lead to comparable, but slightly smaller values for the vertical eddy viscosity. According to Csanady (1976), in estuaries of sufficient depth (i.e. where the vertical length scale of eddies is less than the water depth, with bottom turbulence confined to a height $0.1u_*/f$ from the bottom)

$$A_o = u_*^2/200f \qquad u_* = \sqrt{C_D}\, u_{\text{rms}} \tag{3.4}$$

which, with $C_D = 0.0025$ and $u_{\text{rms}} \approx 0.5$ m s^{-1}, implies $A_o \approx 0.03$ m^2 s^{-1}. Bowden and Hamilton's (1975) formula $A_o = 1.5 \times 10^{-5}\, u_{\text{rms}}^2/f$ leads to roughly the same result. Bowden and Hamilton (1975) also propose a Richardson number dependence

$$F(\overline{Ri}) = (1 + 7\overline{Ri})^{-\frac{1}{4}} \qquad \overline{Ri} = \frac{gH\Delta\rho}{\rho_o u_{\text{rms}}^2} \tag{3.5}$$

with $\Delta\rho \approx 1.5$ kg m^{-1} as the density difference between the upper and lower layers and $H \approx 200$ m as the total water depth. This gives $\overline{Ri} \approx 11$ and suggests that, in

Juan de Fuca Strait, $A_v \approx 0.01$ m^2 s^{-1}. In comparison, Hansen and Rattray (1965) fit similarity solutions to observed mean velocity and salinity profiles and found $A_v \approx 0.0075$ m^2 s^{-1} for Juan de Fuca Strait.

The mean isopycnal slopes in the upper and lower layers can be determined from the surface pressure gradient and stratification. In a uniformly stratified upper layer of depth $h_1 = 75$ m with surface density $\rho_s(x)$, the horizontal pressure gradient at any depth $-z$ is $p_{1_x}(z) = p_{s_x} - \rho_{1_x} g z$, where the surface pressure gradient $p_{s_x} \approx -2.3 \times 10^{-3}$ N m^{-3}. Setting the horizontal pressure gradient at $z \approx -75$ m (the mid-channel depth of zero mean along-channel current) equal to zero implies $\rho_{1_x} \approx 3.1 \times 10^{-6}$ kg m^{-4}. With vertical stratification of $\rho_{1_z} \approx -0.023$ kg m^{-4} at station 72 in May (Figure 3.3), isopycnal slopes are $\approx 10^{-4}$, as found in the data and discussed earlier.

In a linearly stratified lower layer of depth $h_2 = 125$ (with stratification not necessarily equal to that of the upper layer) the pressure gradient is $p_{2_x}(z_2) = -\rho_{2_x} g z_2$, where $-z_2$ is the distance below the interface. Integrating the along-channel momentum equation in the lower layer in the same manner as the upper layer and using the average pressure gradient in the lower layer, one finds that the pressure term $\frac{1}{2}(W h_2/\rho_o) p_{b_x} = \frac{1}{2}(W h_2/\rho_o)\rho_{2_x} g h_2$. The u_t term is dropped for time-averaged currents, and an upper bound for the Bernoulli-like $(h_2 W/2)\partial u/\partial x \approx 0.1$ m^3 s^{-2} term is also small. As in the upper layer, $h_2 W(A_h u_x)_x$ is small, while the sidewall stress term ≈ 0.2 m^3 s^{-2}. The bottom stress $-C_D W u u_{\text{rms}} \approx 1$ m^3 s^{-2}, for $u \approx -0.06$ m s^{-1} and $u_{\text{rms}} \approx 0.3$ m s^{-1} at a depth of 180 m mid-channel (Figure 3.5, deployment 2).

Neglecting the Coriolis term because cross-channel flows are poorly resolved in the lower layer, a balance between the pressure, bottom stress, and interfacial stress terms, using $A_v \approx 0.02$ m^2 s^{-1} as found previously, implies an along-channel density gradient in the lower layer of

$$\rho_{2_x} = \frac{A_v u_{z_{int}} - C_D u u_{\text{rms}}}{g h_2^2/2\rho_o} \approx 1.5 \times 10^{-6} \text{ kg m}^{-4} \qquad (3.6)$$

which corresponds to a density difference of about 0.1 kg m^{-3} over the 70 km between stations 69 and 75. This is about one quarter the difference seen by Crean and Ages (1971) in May (Figure 3.3), although along-channel stratification in the lower layer was much weaker in each of the other 11 months. For example, typical lower layer horizontal density differences between stations 69 and 75 were about 0.1 kg m^{-3} in both April and June.

In summary, a momentum balance, where the surface pressure gradient is assumed to be constant in the along-channel direction, indicates that the interfacial eddy viscosity may be larger than values obtained from commonly used empirical formulae. The strong friction between the upper brackish and lower oceanic water, consistent with observed along-channel isopycnal slopes, should lead to elevated mixing rates and strong cross-channel flows. Large transverse currents are seen in historical data, although the vertical resolution is too low to properly examine the dynamics.

3.2.3 Stability to Internal Mixing

The gradient Richardson number ($Ri \equiv N^2/u_z^2$) in 1973, based on rms velocity differences between 50 and 100 m, ranged from two to six across the strait, with lower values found mid-channel and later in the season (73b versus 73a). Values based on the instantaneous shear dropped to 0.4, with $Ri < 1$ up to 5% of the time (again, at mid-channel for 73b), suggesting that vertical mixing is likely.

Temperature records collected at several locations during the 1973 study (Figure 3.5) appear to support the laboratory picture of the circulation (Figure 2.1) found by Johnson and Ohlsen (1994). Temperatures at nominal depths of 50 and 100 metres are 7.5 °C and 6.3 °C, respectively, at Station 112, and 7.2 °C and 6.6 °C, respectively, at Station 115. That the isotherms are more tightly packed in the north side is consistent with a lack of mixing and of a squeezing by the converging flow in the two layers. This picture is supported by the average flow fields (Figure 3.5), which show a bottom layer, which may be the Ekman layer, bringing water up to the interface,

and water travelling along both sides of the interface into the interior. At the south side, the spreading of isopycnals is as expected, given the divergent nature of the flow and the fact that warmer water from above may be mixing with colder ocean water from below. Water above the interface returns in the surface layer. While there are insufficient data below the interface on the south side, the picture is not inconsistent with water being drawn down at the solid wall boundary into an Ekman type flow. On the other hand, a uniform mixing rate along the entire interface, with the products being swept along by the existing cross-channel flow field to the south wall, is also consistent with the present data.

3.2.4 Summary

Historical data suggest that the interfacial vertical eddy viscosity coefficient $A_v \approx 0.02\ m^2\ s^{-1}$ in May, although much lower values may be more appropriate away from the interface. Later in summer, stronger Fraser River discharge and stratification in Juan de Fuca Strait may lead to higher mixing rates. However, given the limited vertical resolution of the data, neither the magnitude nor the spatial variance of vertical mixing can be established with any certainty.

Higher vertical resolution in both current and hydrography measurements are needed, particularly in the solid and interfacial boundary layers. Acoustic Doppler Current Profilers (ADCP's), deployed on the bottom, which can measure horizontal velocities with a range of 150 metres in the vertical would solve many of the problems with the current data, including that of large mooring depth excursions. High frequency (12 Hz) conductivity-temperature depth (CTD) profilers, with vertical resolutions of tens of centimetres- can do the same for hydrography.

Chapter 4

Observations from 1996

The 1996 observational programme in Juan de Fuca Strait was carried out aboard the MSV Strickland, the University of Victoria's 16 metre research vessel, and consisted of three stages: July 16 to 19 (deployment), July 24 to 26, and August 5 to 7 (recovery). Summer was chosen to coincide with the large runoff of the Fraser River and seasonal maximum surface currents in Juan de Fuca Strait, when cross-channel currents are also expected to be largest. Over the entire period, winds were very light, swell entering Juan de Fuca Strait from the Pacific Ocean was low, and the sky was nearly cloudless.

4.1 Hydrography

An Applied Microsystems STD-12 PLUS was used to obtain 147 conductivity temperature depth (CTD) profiles in order to determine the spatial and temporal variation of hydrography within Juan de Fuca Strait over a spring-neap tidal cycle. The temperature probe, a thermistor bead in a Be-Cu capillary tube, had a response time of 100 ms, an accuracy of 0.05 °C, and a resolution of 0.001 °C. Corresponding specifications for the conductivity probe were 25 ms, 0.01 S m^{-1}, and 0.0003 S m^{-1}, which resulted in an accuracy for the calculated salinity of 0.1 practical salinity units (psu). The pressure was measured with a semiconductor strain gauge which had a response time of 10 ms, an accuracy of 0.15% full scale (for the 200 dbar scale used, this translates to 0.3 dbar), and a resolution of 0.005% (0.01 dbar). The profiler had a maximum sampling rate of about 2 Hz, implying that each recorded measurement is statistically independent.

Unfortunately, the low frequency sampling limited vertical resolution to between 0.3 and 0.5 m for the descent rates used. Microstructure data reveal that

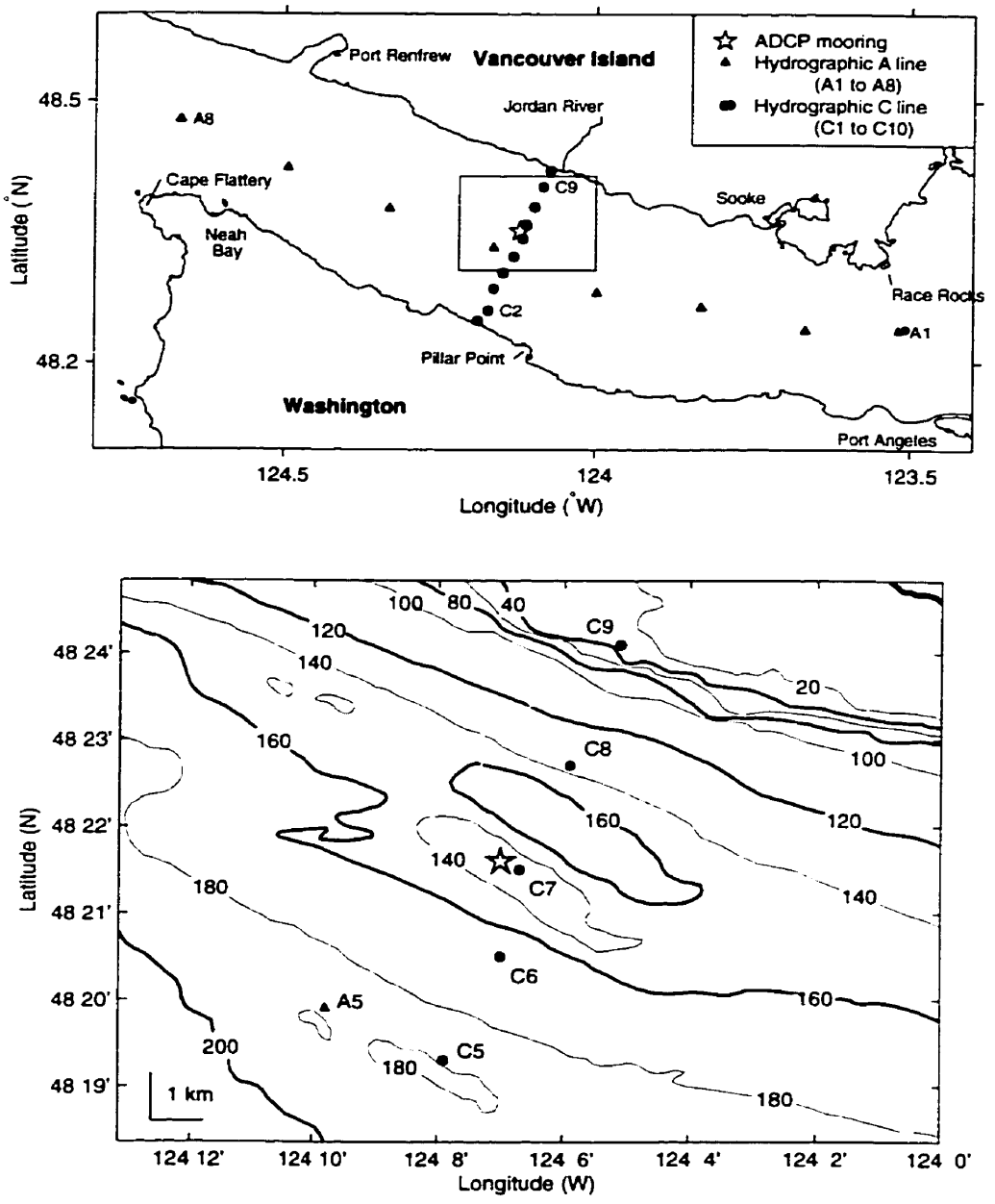

Fig. 4.1. 1996 CTD and ADCP mooring locations in Juan de Fuca Strait and a detailed section near the ADCP mooring showing the bathymetry in metres.

overturns are typically less than 0.5 m in vertical extent, implying that these CTD profiles are not suited to studying energy dissipation within Juan de Fuca Strait. Nevertheless, the hydrography can be used to determine the gradient of the geostrophic velocity through the thermal wind equation. Variations in the ageostrophic component with depth can then be compared to the various forcing terms, such as Reynolds stress, in the momentum balance. In addition, hydrography is needed to classify the estuary as per Hansen and Rattray (1966), to calculate the vertical structure of internal modes (of tides, for example), and to examine the effect of the spring-neap tidal cycle on mixing within the strait.

On each of the three cruise legs, one along-channel (A line) and at least one cross-channel (C line) transect were obtained (Figure 4.1). During the second leg, an additional C line was conducted, as well as a time series at the south ADCP mooring, with 60 profiles over a nine hour interval. The A line consisted of eight stations along the central axis of the channel, beginning south of Victoria and ending north of Cape Flattery, while the C line consisted of ten stations between Jordan River, British Columbia and Pillar Point, Washington.

4.1.1 Density Profiles in Juan de Fuca Strait

For temperatures and salinities typical of Juan de Fuca Strait, the thermal expansion coefficient of water ($\alpha \approx 1.4 \times 10^{-4}$ kg m^{-3} °C^{-1}) is considerably smaller than the density coefficient of salinity ($\beta \approx 7.7 \times 10^{-4}$kg m^{-3} psu^{-1}). Mean hydrographic profiles from Juan de Fuca Strait (Figure 4.2) reveal that horizontal density differences and the resulting pressure gradients are largely controlled by variations in salinity.

Along- and cross-channel transects from the deployment and recovery legs of the observational programme are qualitatively similar. The A-line from July 24 reveals isopycnal shallowing in the seaward direction, as required to drive the lower return flow (Figure 4.3). The cross-channel geostrophic tilt of the isopycnals is seen in the C-line transect of July 26. Isopycnal slopes, of the 26.0 kg m^{-3} isopycnal for

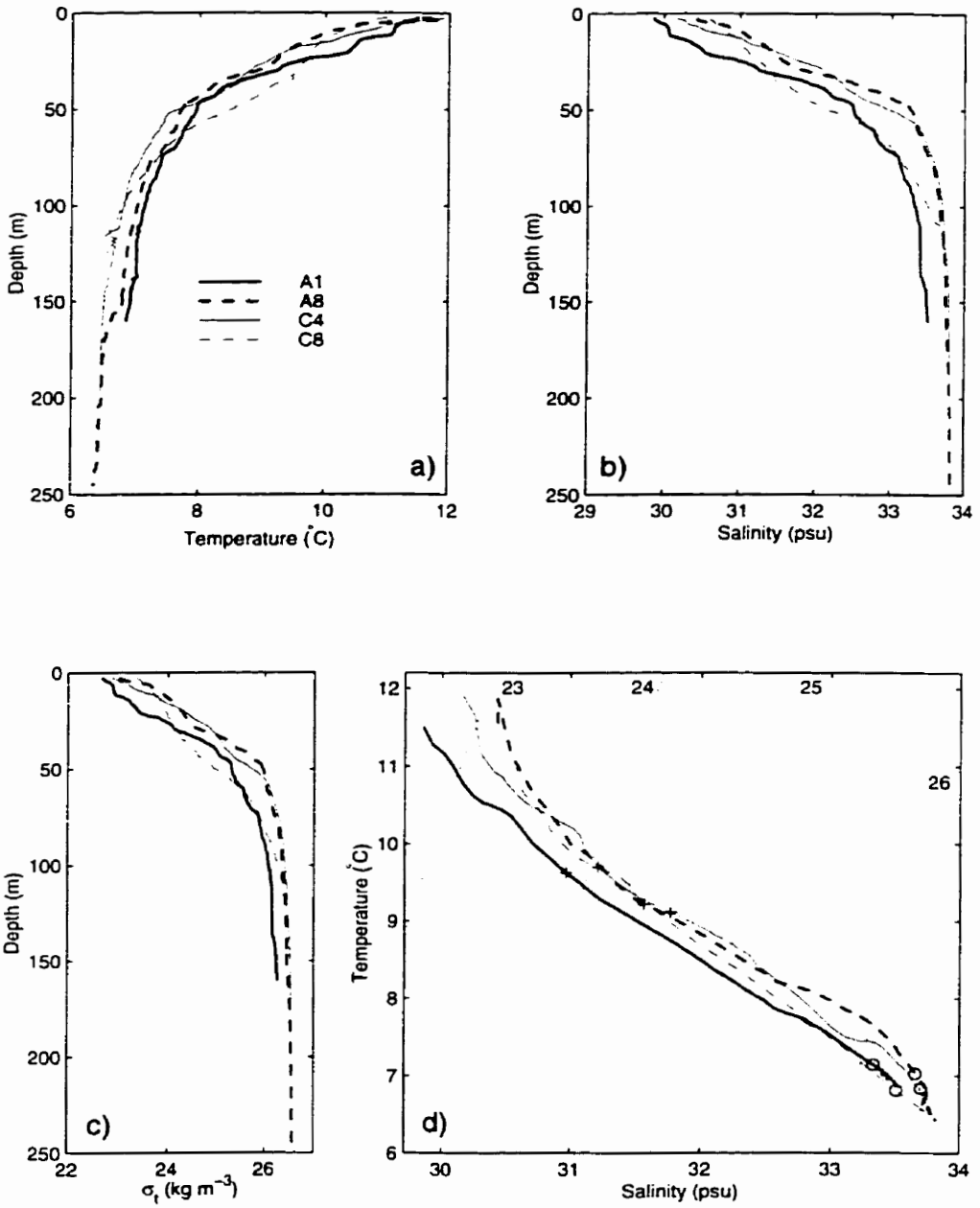

Fig. 4.2. Mean hydrographic profiles at CTD stations A1 (thick solid), A8 (thick dash), C4 (thin solid), and C8 (thin dash): a) temperature (°C), b) salinity (psu), c) density (σ_t, kg m^{-3}), and d) TS diagram, with plus signs and circles indicating depths of 20 and 100 m, respectively, and constant σ_t shown as dotted lines, with values given in kg m^{-3}.

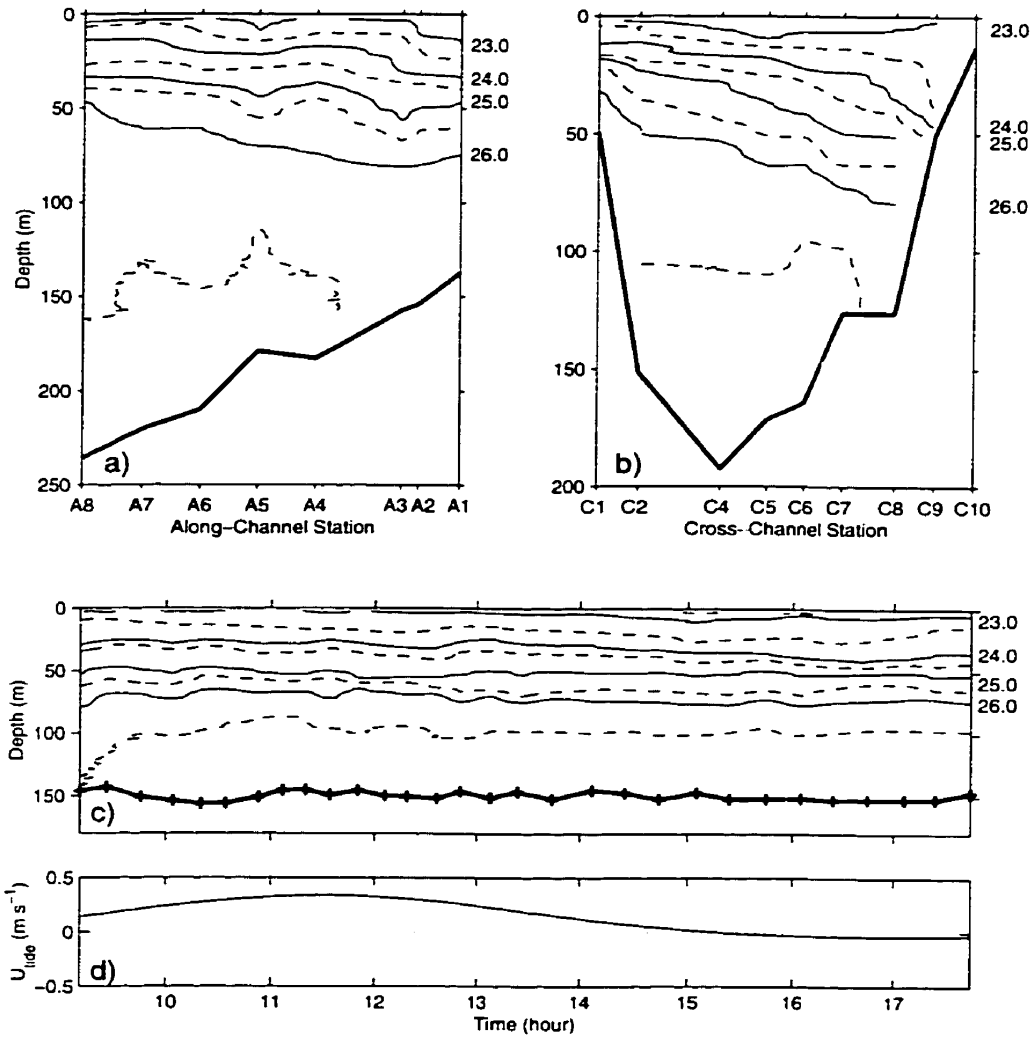

Fig. 4.3. Contours of σ_t for a) an along-channel transect, b) a cross-channel transect, and c) the time series taken at the ADCP station. The contour interval is 0.5 kg m^{-3}, with the numbers to the right of each plot corresponding to the solid lines. The bottom is indicated by the thick line. Plus marks in c) indicate individual profiles in the time series and the tide (positive to the east) at 80 m depth is shown in d).

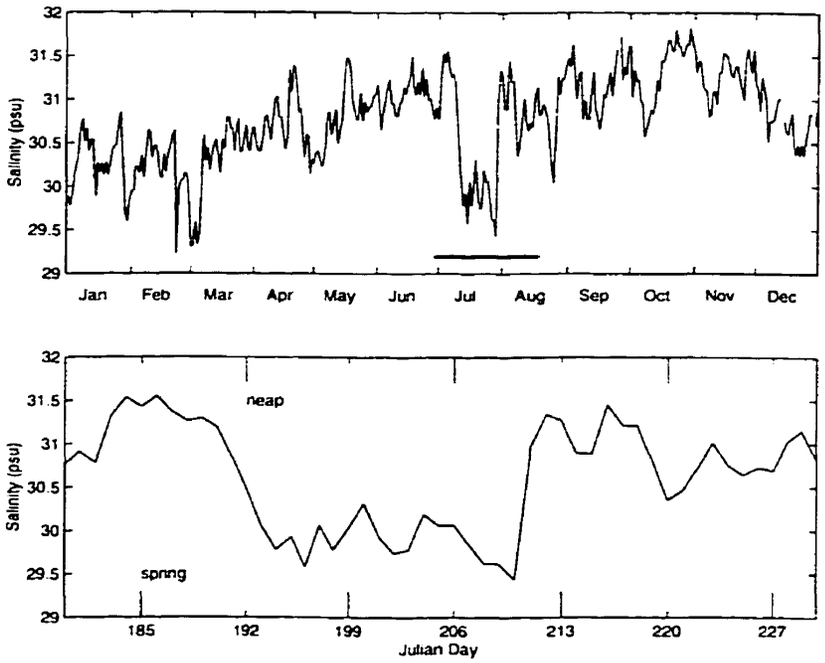

Fig. 4.4. Daily surface salinity recorded at Race Rocks for 1996, with detailed section during the current mooring deployment.

example, where $\xi_y \approx 2 \times 10^{-3}$, are comparable to that of the level of average zero along-channel flow found by Ott and Garrett (1998) using 1973 current meter data.

Although the strong tides within Juan de Fuca Strait undoubtedly affect the time-mean hydrography, the time series taken near the ADCP mooring site on July 25, one day after neap tide, suggests that there is little variation in mid-channel hydrography over much of the tidal cycle. Unfortunately, the time series does not include the transition from peak ebb at 0500, when along-channel speeds (positive now indicating up-channel) reached about -0.6 m s^{-1} throughout the water column, compared with 1.0 m s^{-1} at spring tide. During the weak ebb at 1700, near-surface velocities reached -0.2 m s^{-1}, while at depth the flow did not reverse.

4.1.2 Surface Salinity

Daily surface salinities recorded at Race Rocks (Figure 4.1) reveal that the surface water was anomalously fresh during the deployment of the Acoustic Doppler Current Profiler (Figure 4.4). These freshwater pulses occur on average once a year (Masson and Cummins 2000) and are generally when winds in the Strait of Georgia are from the northwest during weaker neap tides in summer (Griffin and LeBlond 1990). During these events, the estuarine exchange is enhanced beyond the increase normally associated with the neap-spring cycle.

4.2 Acoustic Doppler Current Profiler

For the present study, a bottom-mounted ADCP was deployed at 130 m depth on a submarine hill approximately 7 km off Jordan River (Figure 4.1) on July 17 and was recovered on August 7. The ADCP was gimballed in an aluminum housing which allowed independent rotations along the axes between transducers 1 and 2 (recorded as roll, where for an upward-facing ADCP unit, a positive angle indicates transducer face 2 is higher than face 1) and between transducers 3 and 4 (recorded as pitch, where a positive angle indicates face 3 is higher than face 4), while shielding the ADCP to prevent pitch and roll from varying with tidal currents. Fifty-four two-metre bins of averaged velocity (35 pings over ten seconds) were collected every 30 seconds for 21 days; pitch, roll, and heading were also recorded every 30 seconds.

The returned data were good throughout most of the 106 metre range (i.e. from 127 to 21 m depth), although the top four of 54 bins had "bad" data about half the time. (RDI flags data as bad if the reflected signal intensity is less than the cutoff threshold, which they suggest should be set to 60 counts). This range attenuation may be due merely to beam spreading and sound absorption, although the range attenuation generally occurred during the day. This is consistent with the diurnal migration of zooplankton, which descend from the euphotic zone at dawn to escape predation. The backscatter intensity will be used to show that the restricted range

in the daylight hours is due to a lack of scatterers in the upper water column and not to blocking of the acoustic signal by the large numbers of zooplankton in the lower water column (Section 5.3.2).

4.2.1 ADCP Theory

An Acoustic Doppler Current Profiler (ADCP) measures currents by emitting a sound pulse and measuring the Doppler shift of the returned signal. The original pulse is scattered at each vertical level by plankton and particulates, and possibly turbulence, in the water column which are, in theory, passively carried by background currents. A single pulse can be used to measure current over a range of depths by examining how the returned signal varies over time; the speed of sound in water is used to convert the delay into a distance above the ADCP unit. In addition to currents, the ADCP records the strength of the reflected pulse, or "backscatter intensity", a measure of the amount of particulate matter in the water.

Only the component of water velocity parallel to the sonar beam acts to compress or rarefy the returned signal, requiring multiple beams, each oriented in a different direction, to calculate the three-dimensional water velocity. The four-beam RD Instruments (RDI) 307 kHz broadband workhorse ADCP used in this study has its four beams oriented 20° below the vertical and at nominal azimuthal angles of 270°, 90°, 0°, and 180° (for beams 1, 2, 3, and 4, respectively), where beam 3 is aligned with the ADCP's magnetic compass (i.e. the heading recorded by the ADCP is the angle between magnetic north and the azimuth of beam 3). The actual azimuths are slightly different than the nominal angles for each ADCP unit, owing to the manufacturing process.

a) Instrument Coordinates

The actual ADCP unit used had azimuths of 271.44°, 91.43°, 358.57°, and 178.56°. The azimuths of beam pair 1 and 2, which measure u_I and w_I, where the subscript indicates the currents are in instrument coordinates, are within 0.01° of

being in the same "vertical" plane, which implies that contamination from the v_I current is minimal. The vertical direction in instrument coordinates is perpendicular to the ADCP face, which coincides with the true vertical only for zero pitch and roll angles. Transducers 3 and 4 are likewise within 0.01° of being in the same vertical plane, although this plane is not quite perpendicular to the first (being offset by 87.13°), indicating that the horizontal velocity measured, which should be v_I, is partly 'contaminated' with u_I.

That is, for a downward facing ADCP, the four "beam velocities" are

$$\boldsymbol{B} \equiv \begin{pmatrix} b_1 \\ b_2 \\ b_3 \\ b_4 \end{pmatrix} = \begin{pmatrix} \sin\alpha_1 \sin\gamma_1 & \sin\alpha_1 \cos\gamma_1 & \cos\alpha_1 \\ \sin\alpha_2 \sin\gamma_2 & \sin\alpha_2 \cos\gamma_2 & \cos\alpha_2 \\ \sin\alpha_3 \sin\gamma_3 & \sin\alpha_3 \cos\gamma_3 & \cos\alpha_3 \\ \sin\alpha_4 \sin\gamma_4 & \sin\alpha_4 \cos\gamma_4 & \cos\alpha_4 \end{pmatrix} \begin{pmatrix} u_I \\ v_I \\ w_I \end{pmatrix} \equiv \boldsymbol{M}_I \boldsymbol{U}_I$$

where α and γ are the actual elevations and azimuths for each beam. The three instrument velocities are then easily recovered from the beam velocities by inverting the $\boldsymbol{M}_I$ matrix. Rather than discard the additional information contained in the four beam velocities, however, a fourth column is added to the matrix before inversion to define a fourth "instrument velocity", the "error velocity", which is a measure of the inhomogeneity of the flow across the beam separation. In the RDI software, the vector represented by the fourth column in $\boldsymbol{M}_I$ is chosen to be orthogonal to each of the other three, and to have an rms magnitude equal to the average of that of the first two columns.

For nominal azimuths and elevations

$$\boldsymbol{U}_I^{\,\cdot} \equiv \begin{pmatrix} u_I \\ v_I \\ w_I \\ e_I \end{pmatrix} \equiv \boldsymbol{M}_I^{-1} \boldsymbol{B} \approx \begin{pmatrix} 1.46 & -1.46 & 0 & 0 \\ 0 & 0 & -1.46 & 1.46 \\ 0.266 & 0.266 & 0.266 & 0.266 \\ 1.034 & 1.034 & 1.034 & 1.034 \end{pmatrix} \boldsymbol{B}$$

which implies that the measured velocities, in instrument coordinates, are

$$\boldsymbol{U}_I^{\bullet} \approx \begin{pmatrix} +0.5(u_{I1}+u_{I2}) & & +1.37(w_{I1}-w_{I2}) \\ & +0.5(v_{I3}+v_{I4}) & +1.37(w_{I3}+w_{42}) \\ +0.09(u_{I1}-u_{I2}) & +0.09(v_{I3}-v_{I4}) & +0.25(w_{I1}+w_{I2}+w_{I3}+w_{I4}) \\ -0.35(u_{I1}-u_{I2}) & +0.35(v_{I3}-v_{I4}) & -0.97(w_{I1}+w_{I2}-w_{I3}-w_{I4}) \end{pmatrix}$$

where u_{I1} and w_{I3}, for example, are the u and w velocities (in instrument coordinates) at the location of the ensonified volume of beams 1 and 3, respectively. For flows that are homogeneous across horizontal levels (e.g. the u_{Ii} are identical), $\boldsymbol{U}_I^{\bullet} = \boldsymbol{U}_I$, and the error velocity $e_I \equiv 0$, as expected.

b) Error Velocity

When there are current inhomogeneities in the horizontal direction, the error velocity will not, in general, equal zero. The vertical angle of 20° implies that opposite beam pairs measure currents at a horizontal separation equal to 75% of the vertical height above the ADCP unit. The assumption of spatial homogeneity therefore becomes more unrealistic with height, and should result in increasing error velocities. For individual ensembles, the error velocity is often as large as the vertical velocity, but the rms values of the coefficients for e_I are arbitrarily set, and it is not immediately clear what the error velocity actually measures.

The size of the error velocity relative to the measured vertical velocity can be determined by considering opposing beam pairs individually. Since beams 1 and 2 lie in a vertical plane, they can be used to estimate u_I and w_{Iu}, where the latter is an estimate of the vertical velocity based on the beam pair measuring u. For nominal azimuths and elevations

$$\begin{pmatrix} u_I \\ w_{Iu} \\ v_I \\ w_{Iv} \end{pmatrix} = \begin{pmatrix} 0.50(u_{I1}+u_{I2}) + 1.37(w_{I1}-w_{I2}) \\ 0.18(u_{I1}-u_{I2}) + 0.50(w_{I1}+w_{I2}) \\ 0.50(v_{I3}+v_{I4}) + 1.37(w_{I3}-w_{I4}) \\ 0.18(v_{I3}-v_{I4}) + 0.50(w_{I3}+w_{I4}) \end{pmatrix}$$

where v_I and w_{Iv} are similarly estimated from beams 3 and 4. Assuming that u is unchanged between beams 1 and 2, and v is unchanged between beams 3 and 4, the two estimates of the vertical velocity are $w_{Iu} = 0.5(w_{I1} + w_{I2})$ and $w_{Iv} = 0.5(w_{I3} + w_{I4})$. The vertical velocity calculated from all four beams is the average of these two estimates, while the error velocity is seen to be $\epsilon_I = 1.94(w_{Iv} - w_{Iu})$, roughly twice the estimated difference. With Δw the magnitude of the difference between either of the two estimates and the mean estimate, $\epsilon_I = 3.88\Delta w$.

c) Earth Coordinates

Once in instrument coordinates, the velocities must be rotated to account for the heading, pitch, and roll angles. The conversion process is simply

$$U \equiv \begin{pmatrix} u \\ v \\ w \end{pmatrix} = \begin{pmatrix} \cos H & \sin H & 0 \\ -\sin H & \cos H & 0 \\ 0 & 0 & 1 \end{pmatrix} \begin{pmatrix} 1 & 0 & 0 \\ 0 & \cos P & -\sin P \\ 0 & \sin P & \cos P \end{pmatrix} \begin{pmatrix} \cos R & 0 & \sin R \\ 0 & 1 & 0 \\ -\sin R & 0 & \cos R \end{pmatrix} \begin{pmatrix} u_I \\ v_I \\ w_I \end{pmatrix}$$

where H, P, R are the corrected heading, pitch, and roll angles, respectively, and U is the three-dimensional velocity in earth coordinates (i.e. u positive towards the east, v toward the north, and w upward). The heading is corrected by adding the magnetic declination. The pitch sensor is fixed inside the roll sensor and does not measure the actual pitch: the correction is $P = \arcsin(\sin(p)\cos(r)/k)$, where $k = \sqrt{1 - (\sin(p) * \sin(r))^2}$, and p and r are the pitch and roll recorded by the ADCP, respectively. Finally, for an upward oriented ADCP unit, the roll must be corrected as $R = r + 180^\circ$.

d) Bin Mapping

A further complication introduced by non-zero pitch and roll angles is the fact that at the same instant each beam ensonifies water at different depths, and thus the vertical "bins," determined by the time delay of the returned signal, are no longer in the same horizontal plane. RDI's correction, termed "bin-mapping," is to map the nominal depth of each bin (as if there were no tilts) to the nearest actual depth, for each beam independently. This procedure can, for beams oriented closer to the

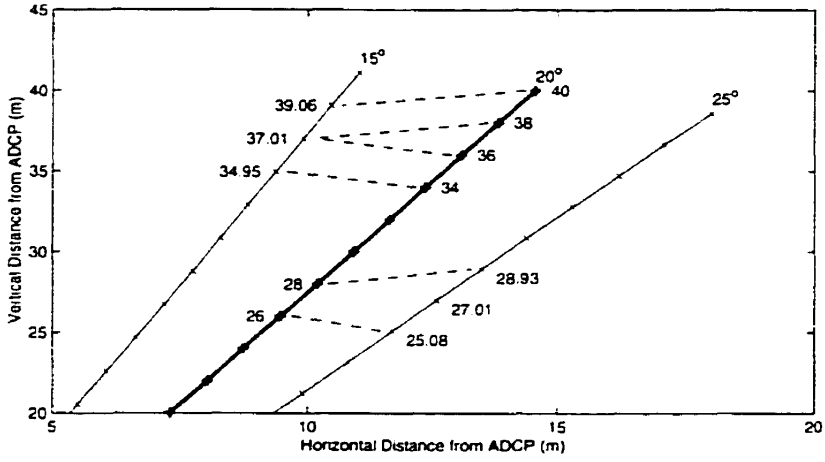

Fig. 4.5. The effect of non-zero tilt angle on bin height. Nominal bin centres (plus signs) are moved (crosses) higher and lower for smaller and larger declinations, respectively. Numbers indicate the height of the bin centre above the ADCP unit, in metres.

vertical, lead to two consecutive actual (i.e. corrected) bins using the same recorded beam velocity. For a pitch of 5° and two metre bins, for example, both bins 36 and 38 m above the transducer head (Figure 4.5) use the beam velocity measured 37.01 m above the ADCP unit. Conversely, for the opposite beam, which would be oriented closer to the horizontal, one recorded bin would be skipped over. That is (Figure 4.5), the bin at 26 m height uses the data recorded for 25.08 m, while the bin at 28 m uses the beam velocity at 28.93 m; the data at 27.01 m is not used. There is almost a four metre (vertical) distance between bin centres at this point.

In addition to omitting or duplicating data, this procedure combines beam velocities averaged over different depth ranges for each beam. As an alternative to this method, the bin heights were corrected by linearly interpolating. For example, for a beam oriented 15° below the vertical, the beam velocity for a bin centred at 38 m is the interpolation between the data recorded at 37.01 and 39.06 m. Inherent in this method is the assumption that the beam velocities, and therefore the actual currents, vary smoothly between bin levels. Were this not true, the built-in "nearest neighbour" scheme would also prove incorrect. However, the beam velocities measured

are actually weighted averages over a depth range equal to 130% of the bin size, implying an overlap of 0.6 m between adjacent two-metre bins. Therefore, significant smoothing of the actual currents is already present in the beam velocities.

The difference between the velocity calculated using RDI's nearest neighbour bin mapping and that using linear interpolation should be largest at depths where strong vertical shear exists and at depths where the difference between the actual depth and the nearest neighbour are greatest. To estimate the magnitude of the difference, the beam velocities for the calculated mean three-dimensional velocity (Figure 4.6) were determined. The given velocity, the mean residual (i.e. non-tidal) measured by the ADCP, was rotated back into instrument coordinates, using the mean ADCP angles: 1.0° (pitch), 4.6° (roll) and 335° (heading). The beam velocities corresponding to the bin centres were determined at the appropriate height for each beam, and earth velocities were recalculated using each of the bin mapping routines. Finally, the original given velocity was subtracted to determine the bias.

Whereas biases for the linear interpolation scheme are less than 0.001 m s^{-1} (i.e. the precision with which the ADCP records velocities) in magnitude at all depths, the RDI routine produces biases approaching 0.01 m s^{-1} in the horizontal velocity (Figure 4.6). Peaks in the biases occur near 30 and 40 m depth because the differences between the nominal and actual depth of the bin centres are maximal there: the roll used (4.6°) is slightly less than the 5° in Figure 4.5.

c) Measurement errors

According to the manufacturer, RDI, the single ping standard deviation for each beam velocity is 0.02 m s^{-1}. Lu (1997) calculated it to be between 0.02 and 0.03 m s^{-1}, using measurements in "almost slack water" after subtracting second-order polynomials from each beam velocity to account for the ship's drift. In addition, although the recorded ADCP angles (pitch, roll, and heading) have a precision of 0.1°, the accuracies of these measurements are only 1°. With the vertical velocity, w, an order of magnitude smaller than horizontal velocities, small biases in pitch and roll may contaminate w sufficiently to render data products such as the Reynolds stress

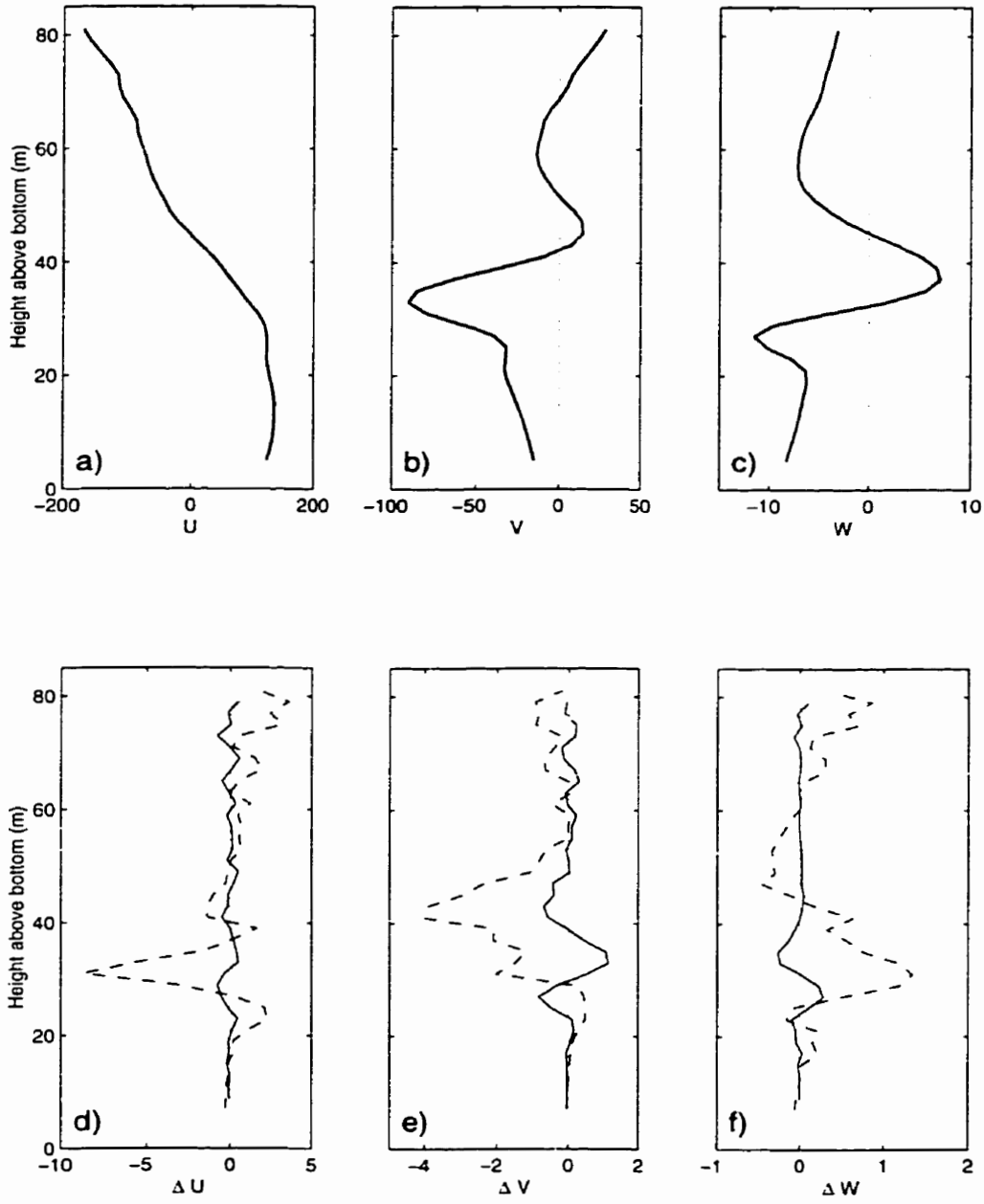

Fig. 4.6. The effect of the bin mapping algorithm on calculated velocities. For the three-dimensional velocity shown in a), b), and c), the corresponding biases are shown in d), e) , and f), with dashed lines for the RDI nearest neighbour bin mapping and solid lines for linear interpolation. All currents are in units of 10^{-3} m s^{-1}.

$\overline{u'w'}$ useless. Finally, in rotating the horizontal plane into suitable along-channel (x, with velocity u, positive up-estuary) and cross-channel (y, with velocity v, positive northward) directions, the overall channel orientation and local bathymetry must be accounted for. Bottom slopes cause the local "vertical" axis (in matching measured bottom boundary layer Reynolds stresses to theoretical expectations based on tidal speed, for example) to vary from the slope angle at the bottom to true vertical at the surface.

f) Reynolds Stress Measurements

For nominal beam azimuths and elevations, it can be shown (e.g. Lu and Lueck 1999) that the average Reynolds stress can be calculated as

$$\overline{u'w'} = \frac{b_1'^2 - b_2'^2}{2\sin 2\alpha} \tag{4.1}$$

where b_i' is the variance associated with the ith beam. Initially, it was assumed that the velocity field must be uniform across the beam spread, but Plueddemann (1987) showed that the result is also valid when only the statistics of the turbulence are assumed to be uniform (e.g. $\overline{u'_{I1}\,u'_{I1}} = \overline{u'_{I2}\,u'_{I2}}$). Van Haren *et al.* (1994) then showed that (4.1) is equivalent to

$$\begin{aligned} \overline{u'w'} &= \overline{u'_I\,w'_{Iu}} = \overline{u'_I(w' - \epsilon')} \\ \overline{v'w'} &= \overline{v'_I\,w'_{Iv}} = \overline{v'_I(w' + \epsilon')} \end{aligned} \tag{4.2}$$

where w_{Iu} is the estimate of the vertical velocity obtained from the beam pair associated with the velocity u, w_{Iv} is that from the beam pair associated with v, w is the mean of these estimates, and $\epsilon = (w_{Iu} - w_{Iv})/2$ is half the difference.

Lohrmann *et al.* (1990) measured currents with an ADCP within 2 m of the bottom in a boundary layer, demonstrating that the variance of the beam velocities can be used to directly calculate the Reynolds stress. Stacey *et al.* (1999a) used a vessel-mounted ADCP to measure Reynolds stresses in an unstratified flow and

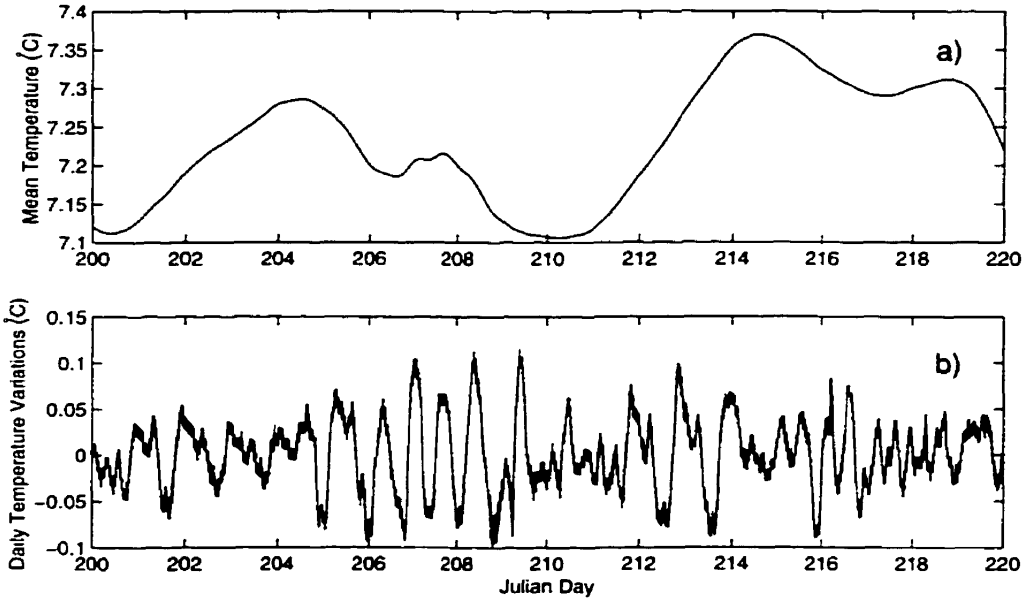

Fig. 4.7. Temperature record from the ADCP, in degrees Celsius: a) the 24 hour running mean, b) the residual (i.e. actual temperature - running mean).

showed that the errors and biases associated with the measurements were sufficiently small to enable significant estimates of turbulence profiles to be made and that these errors and biases were "consistent with those predicted by the application of statistical error analysis." Lu and Lueck (1999) used measurements from an ADCP mounted at the bottom of a tidal channel to demonstrate that significant covariance of turbulent eddy velocities could be calculated over a range of 25 m above the bottom. It is only recently, however, that direct measurements of Reynolds stresses have been made in stratified flows (Lu and Lueck 1999, Stacey *et al.* 1999b).

4.2.2 ADCP Temperature Measurements

The temperature record from the ADCP (Figure 4.7) contains both diurnal and semi-diurnal signals; spectral analysis shows the energy to peak at frequencies corresponding to 23.8 ± 3 hour and 11.9 ± 1 hour periods. These variations are likely the result of the tidal excursion in Juan de Fuca Strait, which can be as large as 5 km

along the channel, although the magnitude of temperature fluctuations within any 24-hour period, which ranges from 0.05°C to 0.2°C, does not appear to be related to the spring-neap cycle. An observed linear trend of +0.13°C in the bottom temperature over 20 days may be a result of solar heating, both inside and outside the strait; during July and August, skies were nearly cloudless, air temperatures were very warm, and winds were light. The running mean also shows a decrease in bottom temperature over the six days centred on neap tide (Julian day 206) of nearly 0.25°C and a similar rise over the six days around spring tide (Julian day 213). This is consistent with an increase in bottom mixing at spring tide, and the temperature equation can be used to estimate the vertical eddy diffusivity of temperature. Neglecting horizontal mixing and cross-channel advection and assuming that the vertical eddy diffusivity of temperature is independent of depth, (2.10) reduces to

$$T_t = \kappa_T T_{zz} - \overline{u} T_x \tag{4.3}$$

where $\overline{u}$ is the mean velocity at the bottom. Between Julian days 206 and 208 (neap tide), the mean ADCP current in the lowest bin is $\overline{u} \approx 0.16$ m s^{-1}, while $\overline{u} \approx 0.13$ m s^{-1} between days 213 and 215 (spring tide). The trend in temperature (Figure 4.7) is $T_t \approx -0.5 \times 10^{-6}$ °C s^{-1} after neap tide and $T_t \approx +1 \times 10^{-6}$ °C s^{-1} after spring. The mean hydrography (Figure 4.2) is used to estimate the vertical temperature derivative. Between 80 and 130 m, $T_z \approx 8 \times 10^{-3}$ °C m^{-1}, while that between 50 and 80 m is $T_z \approx 17 \times 10^{-3}$ °C m^{-1}, implying $T_{zz} \approx 2 \times 10^{-4}$ °C m^{-2}. The horizontal derivative in temperature, however, is difficult to estimate from either the mean temperature profiles or the along-channel transects (Figure 4.3).

With three unknowns (the eddy diffusivity at spring tide, κ_s, is assumed to be different from that at neap tide, κ_n) and two equations, a relationship between κ_s and κ_n is needed. Assuming that κ is proportional to the mean of the current magnitude, which is 0.35 m s^{-1} at neap and 0.46 m s^{-1} at spring, $\kappa_s \approx 1.3\kappa_n$. Eliminating T_x, $\kappa_n \approx 0.014$ m^3 s^{-1} and $\kappa_s \approx 0.018$ m^3 s^{-1}. The calculated horizontal temperature gradient is $T_x \approx 2 \times 10^{-5}$ °C m^{-1}, equivalent to a change of 2 °C over the length of

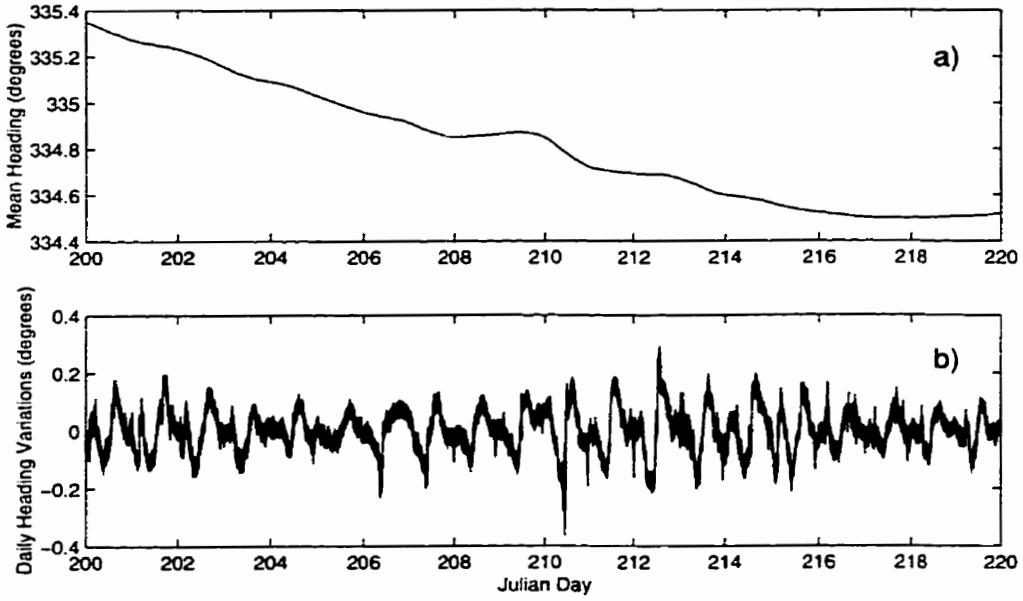

Fig. 4.8. Compass heading of the ADCP, in degrees clockwise from true north: a) the 24 hour running mean, b) the residual (i.e. actual heading - running mean).

Juan de Fuca Strait. Both the July 1968 temperature transect (Crean and Ages 1971) and the mean CTD temperature profiles 4.2 suggest that the along-strait difference in bottom temperature is closer to 0.5 °C. There are large uncertainties both in the measured temperatures and in the dependence of the eddy diffusivity on the current however. For example, for κ proportional to the square of the current, the calculated along-channel temperature gradient is reduced by half.

4.2.3 ADCP Compass and Tilt Angle Measurements

The compass heading (Figure 4.8) record also contains diurnal and semi-diurnal signals (spectral analysis revealed the same frequencies as for the temperature record), with the amplitude of tidal fluctuations over a day increasing from about 0.3° during neap tide to nearly 0.5° during spring tide. The trend of approximately -1° is likely the result of battery depletion over the deployment; as the voltage decreases, less current is drawn to power the transducers, decreasing the local magnetic field.

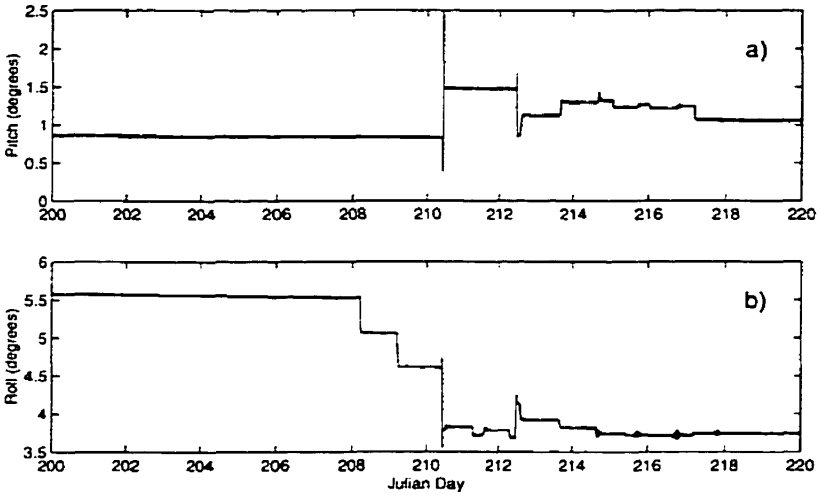

Fig. 4.9. Tilt angle records from the ADCP, in degrees a) pitch, b) roll.

The slight rise in bottom temperature over the deployment is not likely to have a noticeable effect on the compass, as the mean temperature decreased during neap tide and increased during spring tide, while the mean compass heading decreased over both time periods. Indeed, the variations in heading at tidal frequencies were also inconsistent with those of temperature, both in magnitude (e.g. heading variations were relatively small between Julian days 205 and 208) and in phase. Unlike temperature, however, changes in the local magnetic field can arise from outside Juan de Fuca Strait. Variations in the Earth's magnetic field due to daily lunar variations in the ionosphere could be expected to account for at most 0.02° fluctuations, and motional induction due to the tides passing above the ADCP would be of the same order (Rob Tyler, personal communication, 2000). At any rate, the phase difference between the compass heading and tide did not remain constant over the deployment. However, variations of 0.2° could be caused by non-local fields generated by deep water tides in the Pacific (Rob Tyler, personal communication, 2000).

The average pitch and roll measured by the ADCP over the 21-day deployment were 1.0° and 4.6°, respectively. Neither an overall drift nor a diurnal or semi-diurnal signal is found in either the pitch or roll record (Figure 4.9). Instead, sudden jumps

in tilt angles occur on several occasions throughout the deployment and are unrelated to the tidal phase. There are smaller jumps, of about 0.5°, during peak flood and ebb, but the two largest events, at Julian days 210 and 212, occur at slack tide. On day 210, for example, there are small variations in pitch of about 0.2° starting at 0950, followed at 1030 by a large increase of 3° over 1 minute and a subsequent reduction of 1° over the next minute; the net jump in pitch is 2.1°. Over that same two minutes, net jumps in roll and heading of 0.8° and 0.2°, respectively, were measured, with activity similar to that seen in the pitch record during the preceding 40 minutes. These sudden upward shifts in the measured angles are likely due to settling of the ADCP housing into the bottom (mud was found trapped within the housing upon recovery), followed by a slight decrease as the ADCP unit righted itself within the gimbals somewhat.

4.2.4 Calculated Earth Velocities

The calculated east, north, and vertical velocities at maximum spring tide (July 31, Julian day 213) show large tidal flows and strong vertical shear (Figure 4.10). The inequality in subsequent ebbs or flows is indicative of the mixed diurnal - semidiurnal nature of the tides in Juan de Fuca Strait. Current magnitudes reach 1.5 m s^{-1} on both flood and ebb. The largest outflows (inflows) occur in the upper (lower) layer as expected for the combined tidal and estuarine circulation. Inflows (outflows) in the upper (lower) layer reach only +0.8 m s^{-1} (−0.9 m s^{-1}). Over the 21-day deployment, maximum daily currents varied considerably. During neap tide (Julian day 206) inflows never exceeded +0.65 m s^{-1}, while outflows reached −0.85 m s^{-1}.

Twenty-four hour running means of the current (Figure 4.11) reveal positive (negative) up-channel velocities in the lower (upper) layer, as expected for estuarine exchange flow. Along-channel flows increase at neap tide (Julian day 206), as predicted by the model of Griffin and LeBlond (1990) following the periodic removal of the mixing barrier. At the same time, mid-depth cross-channel and vertical currents intensify considerably. Generally, these low-frequency currents are smallest at spring

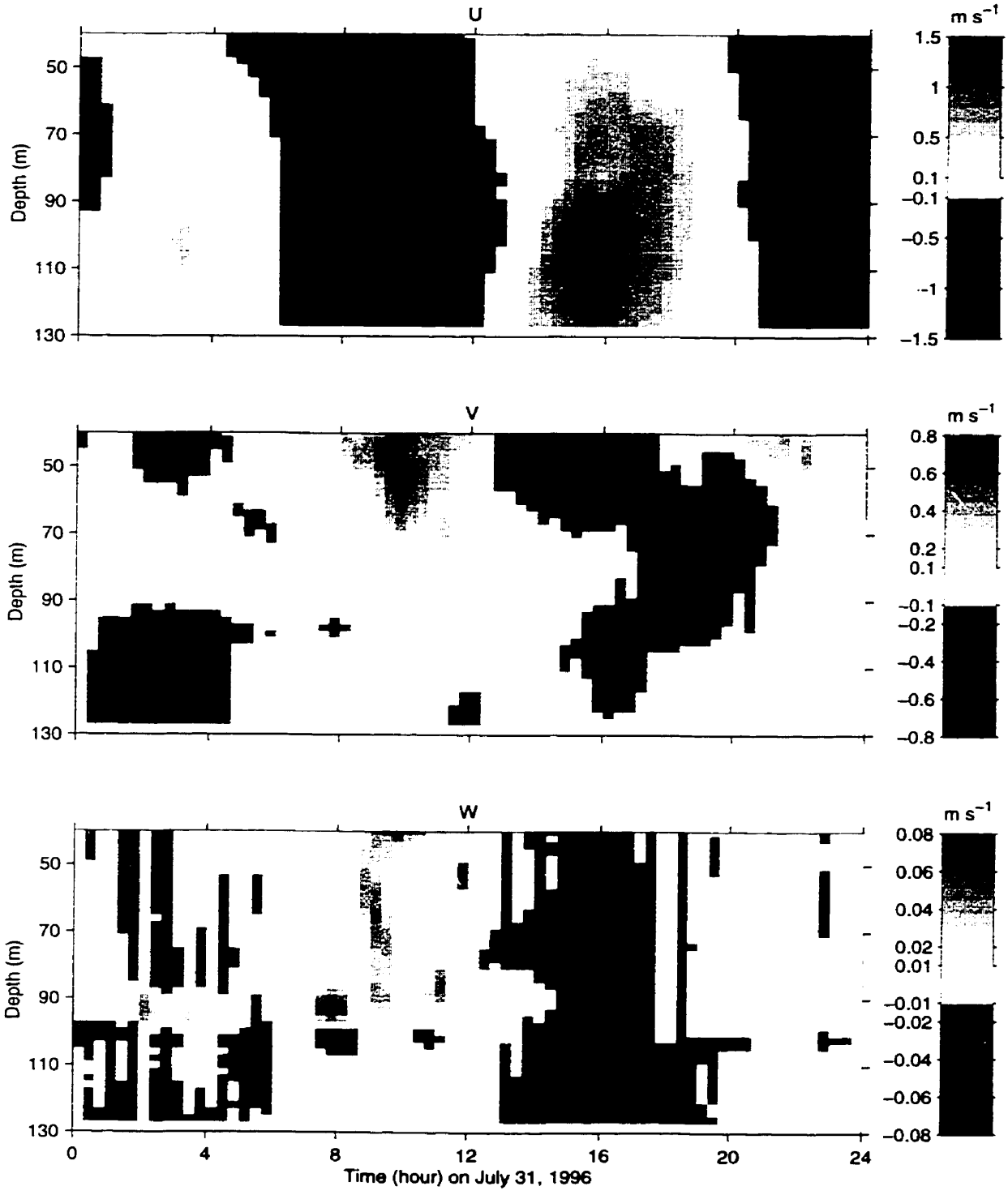

Fig. 4.10. Twenty minute means of east, north, and vertical velocities on Julian day 213, maximum spring tide.

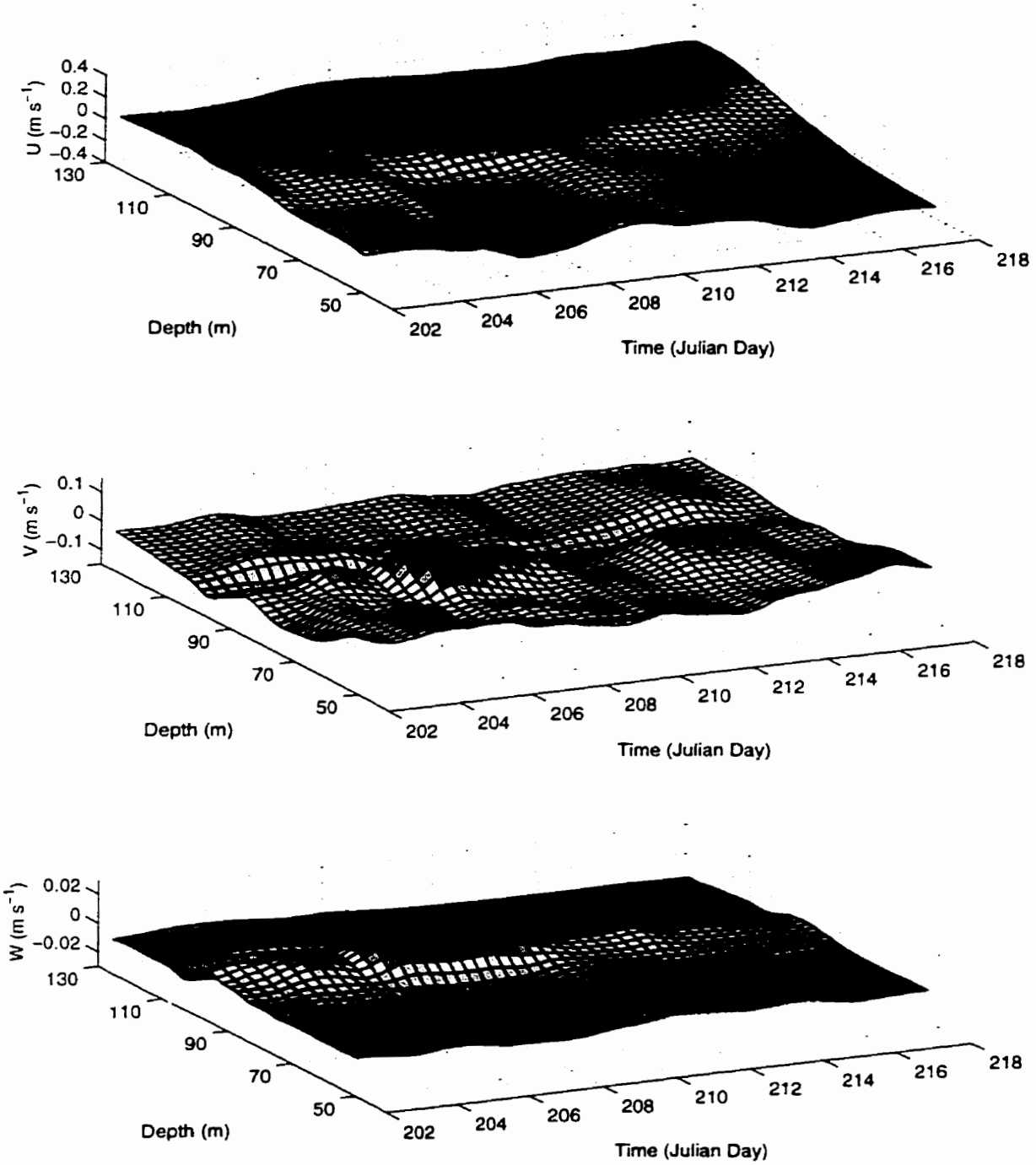

Fig. 4.11. Twenty-four hour running mean of two-hour averaged east, north, and vertical currents.

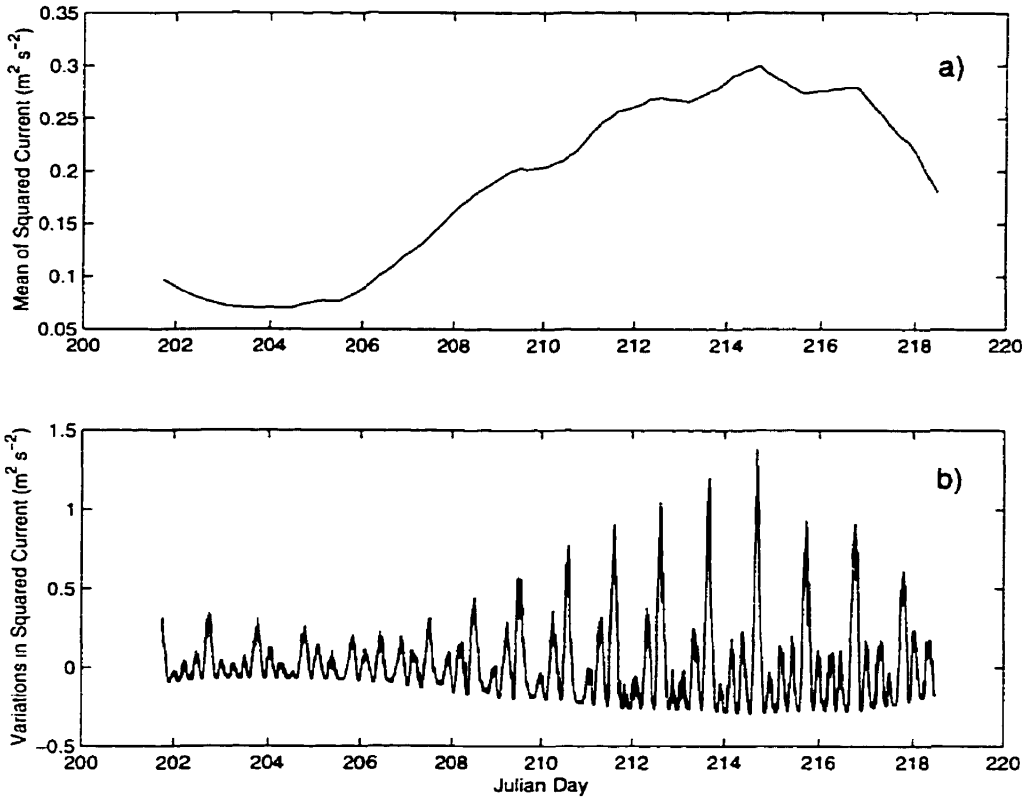

Fig. 4.12. Square of bottom current: a) the 48 hour running mean, b) the residual (i.e. actual - running mean).

tide (Julian day 213), after which flows above 106 m strengthen in the out-channel direction. As the interface, the depth of zero mean along-channel current, is lowered, less oceanic water enters Juan de Fuca Strait and reaches the Strait of Georgia.

The spring-neap tidal inequality can be seen by examining the kinetic energy associated with the horizontal current of the lowest depth bin (Figure 4.12). The low-passed energy, obtained by calculating the 48-hour running mean of the along-channel current magnitude closest to the bottom, is about three times larger during spring tide than neap tide. Variations within 24-hour periods are also about three times larger at spring tide. The inequality in subsequent ebb and floods is especially noticeably at spring tide, where the largest peaks each day are associated with one of the daily floods.

Chapter 5

The Vertical Velocity

In the past, traditional current meters have generally only measured the horizontal component of the flow. The vertical velocity is much smaller and requires more accurate measurements. Although Acoustic Doppler Current Profilers are able to measure the three-dimensional velocity field, the vertical velocity component may be susceptible to errors inherent in the measurement process.

As the ADCP beams spread with height, they sample different water parcels, and spatial inhomogeneity of the flow can introduce errors in the measured current. Small errors in the measured pitch and roll can also lead to significant contamination of the vertical velocity. The tilt sensors on the ADCP are accurate to within 1°, which may not be sufficient if Reynolds stress estimates are to be made. Moreover, the vertical velocity may be affected by differential zooplankton movement. At dawn, the zooplankton in Juan de Fuca Strait descend from the euphotic zone above 50 m to depths of about 100 m to escape predation. At dusk, they migrate upwards again in order to feed on phytoplankton. These movements show up clearly in the backscatter intensity record of the ADCP, travelling at a rate of about 0.01 m s^{-1}. Although there is high correlation between the vertical motion of individual zooplankton at dusk and dawn, there is no correlation in differential zooplankton movement in the horizontal direction, and horizontal current measurements are unaffected.

5.1 Spatial Inhomogeneity

The error velocity is a measure of the spatial inhomogeneity of the flow over the ADCP beam separation. If the current changes significantly over this distance, the estimates of velocity, particularly the vertical component, are not representative of the true flow. The magnitude of the error velocity is less than the vertical velocity

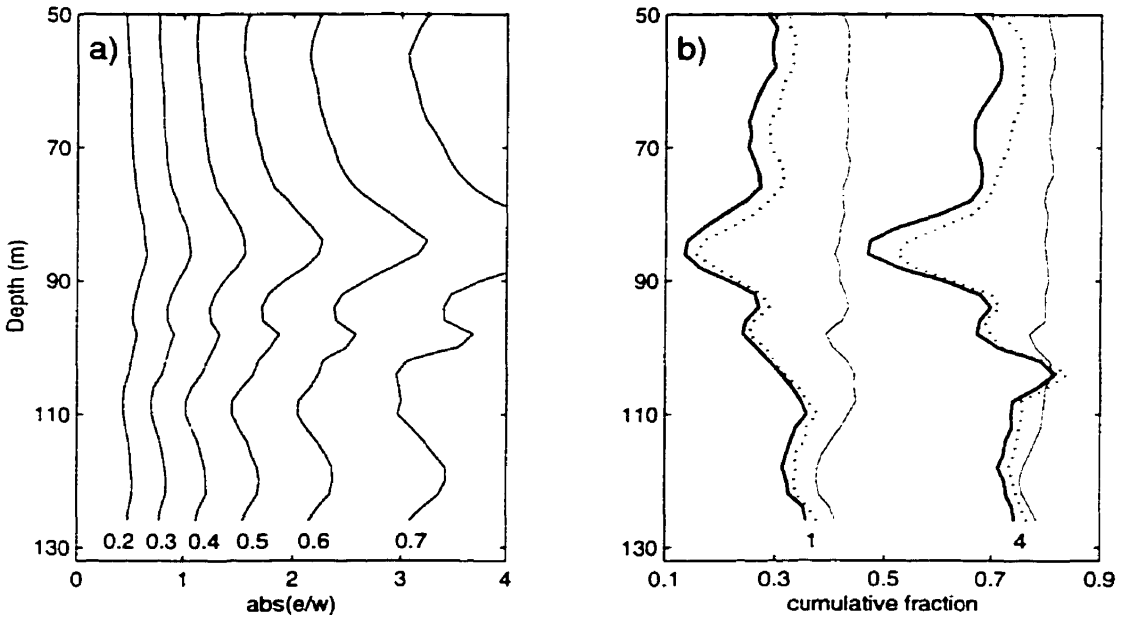

Fig. 5.1. Cumulative fraction for the value of the error velocity e to vertical velocity w ratio: a) contours for entire record, with contour labels at the bottom, b) mean cumulative fraction below unity and 4 for three days after neap tide (Julian days 206 to 208, thick lines) and three days after spring tide (Julian days 213 to 215, thin lines). The three-day means are indicated by solid lines, while dotted lines denote the mean plus standard deviation.

estimate approximately 35% of the time at all depths (Figure 5.1). However, the differences in vertical velocity estimates between each pair of orthogonal beams and the mean velocity was shown to be approximately one quarter the error velocity. About 75% of the recorded w estimates are above this value. Excluding the interfacial region (i.e. 80 to 90 m depth) where the error velocities are relatively larger, the error to vertical velocity ratio does not increase significantly with height.

The error to vertical velocity ratio does change throughout the spring-neap cycle however (Figure 5.1), being larger at neaps. During neap tides when freshwater pulses escape the mixing region in the Gulf Islands, one would expect currents, and therefore shear, to be larger inside Juan de Fuca Strait. Increased shear leads to more turbulence, and therefore a decrease in the horizontal length scale over which currents

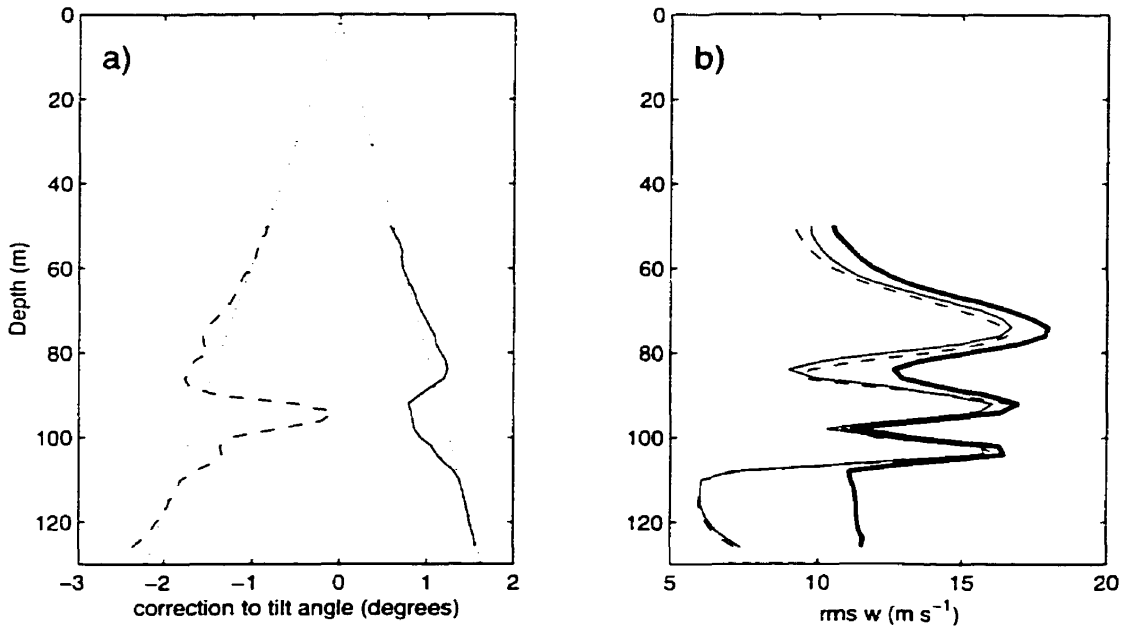

Fig. 5.2. Minimisation of the root-mean-square vertical velocity to determine the ADCP tilt angle biases: a) the depth variation in roll (solid line) and pitch (dashed line) angle "corrections" which minimise the rms vertical velocity, b) the resulting rms w, with thick line indicating the rms vertical velocity using the recorded tilt angles. The dotted lines in a) are the best linear fit to the calculated angles over the depth ranges 50 to 60 m and 110 to 120 m.

are correlated. Horizontal currents are also slightly larger at spring tide, which tends to further reduce the error velocity by decreasing the time over which eddies travel between the ADCP beams.

5.2 Horizontal Contamination of Vertical Velocities

Biases in the measured pitch and roll angles also lead to errors in the measured velocities. The effect on the horizontal components is very small, because the vertical velocity is an order of magnitude less than (u, v). The vertical velocity, on the other hand, can be greatly affected. Estimates of the biases can be made by examining the depth variation in the angles with which the (u, w) and (v, w) currents deviate from the horizontal. A constant variation with height is indicative of a bias in the

measured tilt angles, whereas a linear variation which tends to zero at the surface suggests that bottom topography is important in directing the current.

Rotating the measured (u, v) currents by the negative corrected heading returns the horizontal currents to the frame of reference relative to the ADCP. That is, u and v are directly computed from beam pairs (1,2) and (3,4), and each use only the roll and pitch, respectively. Possible contaminations of the vertical velocity by the horizontal components are investigated by examining the effect of altering the tilt angles from those measured by the ADCP. The pitch and roll "corrections" at each depth which minimise the root-mean-square vertical velocity vary from -2.5° to $+1.5^{\circ}$ (Figure 5.2). Both the roll and pitch tend to zero as the surface is approached, revealing no bias constant with height.

Between 60 and 100 m depth, the rms value of the measured vertical velocity fluctuates considerably with height, and over much of the range there is almost no reduction in the rms w. This suggests that interfacial processes are dominating the dynamics of the vertical velocity, making it difficult to determine the effects of either a bottom slope or a bias in the angle measurements. Above 60 m, the rms w falls to values comparable with those in the lowest 20 m, suggesting that interfacial effects are no longer felt. In the bottom 20 m the large reduction in rms w clearly reveals the presence of a bottom slope and the variation in the pitch "correction" indicates that there may be two separate regimes. Below 120 m, the fall-off in pitch is much greater, suggesting the effects of small-scale topography. This should not affect currents in the upper water column to the extent that large scale topography will.

The best linear fits between 110 and 120 m and above 60 m to the calculated roll and pitch corrections (Figure 5.2) have surface intercepts of -0.03° and $+0.02^{\circ}$ for the roll and pitch, respectively. For a horizontal current of 1 m s^{-1}, a tilt error of 0.03° corresponds to a bias of less than 10^{-3} m s^{-1}, which is the precision of the recorded velocity estimates. Given the uncertainties in the measurements then, there is no evidence to suggest that a bias in either tilt angle exists and no corrections are made to the measured pitch and roll. The bottom slope at the ADCP site is estimated

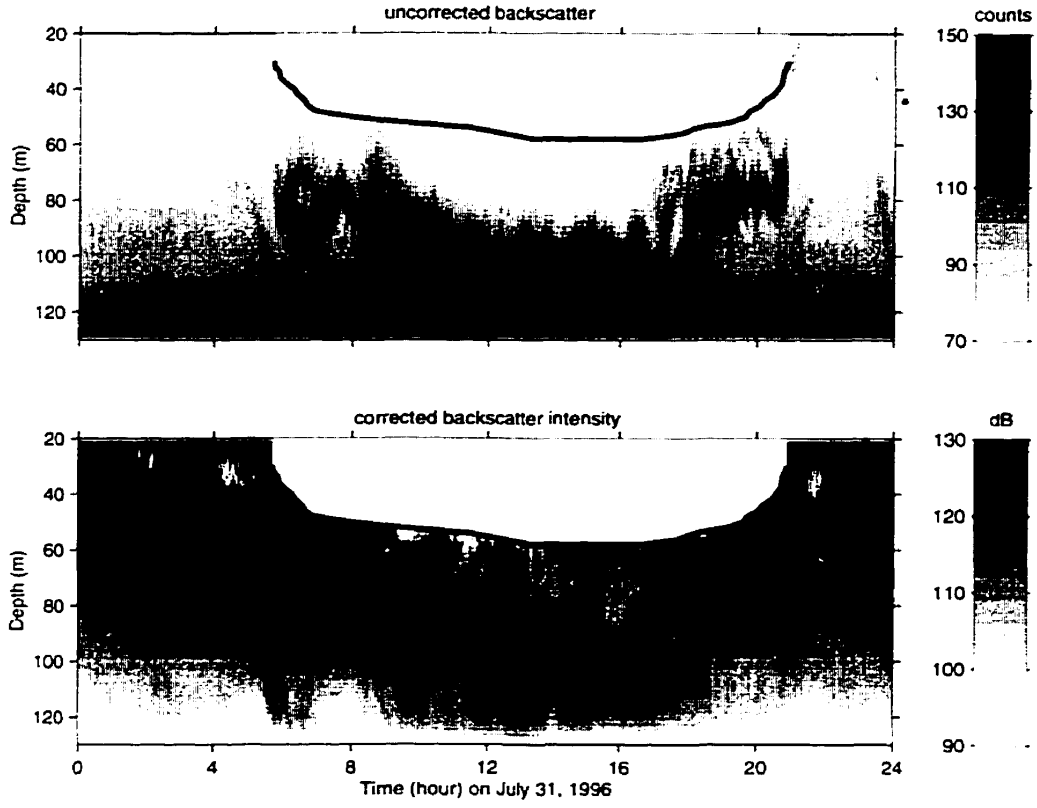

Fig. 5.3. Backscatter intensity on Julian day 213, maximum spring tide. The solid line indicates the depth above which the uncorrected backscatter is less than 60 counts).

to be approximately 2° (i.e. a 30 m rise over nearly 1000 m), not inconsistent with the roll and pitch corrections of −2.2° and 1.8°, respectively, at the bottom (Figure 5.2).

5.3 Backscatter Intensity and Target Strength

The use of the ADCP to measure water movement requires that sound-reflecting particles be passively advected by the background current; active movement by zooplankton, for example, may lead to erroneous current measurements. This problem should be most significant during the dawn and dusk vertical migrations of zooplankton in Juan de Fuca Strait, clearly seen in the backscatter strength of beam 1 on July 31 (Figure 5.3). Zooplankton migrate upwards at dusk to feed on phytoplankton

and downwards at dawn to escape predation in the euphotic zone. In the horizontal, however, active motion between individual zooplankton is uncorrelated, so possible biases are examined only in the measured vertical velocity. Sustainable swimming speeds are typically 1 to 2 body lengths per second (Dave Mackas, personal communication, 1999), with body lengths varying from 0.001 to 0.02 m, although the smaller zooplankton do not migrate as much. The maximum expected migration speeds are therefore approximately 0.02 to 0.04 m s^{-1}.

5.3.1 Correction of Backscatter Intensity Measurements

Obtaining target (i.e. zooplankton) concentrations from measured backscatter strength requires both that the relative backscatter at each level be corrected to allow for comparisons between vertical levels and that the resulting absolute backscatter strength be calibrated to target concentrations through plankton tows. No plankton tows were done in Juan de Fuca Strait in 1996, and the ADCP does not store the emitted signal strength, so neither the transmission losses due to particulate absorption or scattering nor an absolute measure of target strength can be determined. One can analyse relative target concentrations throughout the water column to determine how zooplankton movement affects the measured current, although this still requires that the relative backscatter at each depth be corrected for beam spreading and the absorption of sound in sea water.

Neglecting additional divergence (or convergence) of the sonic beam due to the differential speed of sound across the beam face, the area ensonified by the transmitted pulse is a section of spherical shell with constant solid angle Ω. This area is proportional to r^2, where r is the distance from the transducer to each of the depth bins. Holding the total power passing through each successive bin constant (transmission loss is accounted for below), the power per unit area decreases as r^{-2}. With the reference intensity defined as the intensity 1 m above the transducer, the loss in intensity (in dB) with distance, relative to the intensity I_o at $r_o = 1$ m, is $10 \log_{10}(I_r/I_o) = 20 \log_{10}(r/r_o)$.

Loss of intensity as a sound pulse travels through a medium is caused by thermal conductivity and viscosity of the medium, as well as by scattering and absorption by particulates in the water. The effect of thermal conductivity is negligible for water, and, excluding scattering and absorption by particulates, "the significant losses in water are caused by shear viscosity and bulk viscosity." (Clay and Medwin 1977) The latter, due to molecular rearrangements over a sound wave period, are more important in water than the former, which are due to friction caused by shear in the medium. The loss per cycle is maximum when the relaxation time, the amount of time molecular re-ordering takes in response to varying pressure, equals the sound wave period and gets smaller as the difference increases. In the ocean, sound absorption is mostly due to the relaxation times of freshwater (10^{-11} s), magnesium sulfate (10^{-5} s), and boric acid (10^{-1} s). At 307 kHz the latter is negligible, while magnesium sulfate dominates.

The combined effect is that the loss in pressure (intensity is proportional to pressure squared) with distance is found to be proportional to the original pressure p_o, yielding $p = p_o e^{-\alpha_e r}$, where α_e is the exponential pressure attenuation rate. The intensity loss (in dB) is then $20\log_{10}(p/p_o) = \alpha r$, where $\alpha = \alpha_e \; 20\log_{10}(e^1)$ is the absorption, or attenuation, coefficient. The rate of absorption in seawater is a function of pressure, temperature, salinity, pH, and sound frequency. Using the empirical equation derived by Francois and Garrison (1982) for a depth of 100 m, T = 7 °C, S = 33 psu, and pH = 8.0, $\alpha \approx 0.070$ m^{-1} for the ADCP frequency of 307 kHz. The corrected intensity, I_c, is then simply

$$I_c = I_m + 2 * (20\log_{10}(r) + \alpha r) \qquad (5.1)$$

where both I_c and the measured backscatter intensity I_m are in decibels, relative to the intensity of the transmitted pulse, and the extra factor 2 accounts for the return trip the sound pulse must make. As mentioned, the original intensity is not recorded by the ADCP unit, so relative intensities cannot be converted to absolute intensities. Indeed, without knowing whether the strength of the transmitted pulse varied over

the deployment, as it might as the battery is drained, comparisons between different times might not be meaningful. Finally, it should be noted that the RDI software records 'counts', a volumetric measurement of the echoes returned from scatterers in the water. The scale factor to convert to intensity is 0.45 dB/count, so that $I_m = 0.45 I_r$, where I_r is the backscatter strength recorded by the ADCP.

5.3.2 The Diurnal Zooplankton Migration

Using the corrected intensity (Figure 5.3) as a relative measure of target strength, the vertical migrations of zooplankton at dawn (downward) and dusk (upward) can be clearly seen. Between 0900 and 1000, the mean corrected backscatter intensity from the bottom to 60 m (above which the data are bad during daylight hours) is 5 dB larger than between 1500 and 1600 in each of the four beams. Although the attenuation rate is smaller between 1500 and 1600, the ADCP range is decreased by 4 m, suggesting that the lack of scatterers above 60 m is the main reason for the bad data during daylight hours.

The vertical speeds of the zooplankton reach peaks of about 0.02 m s^{-1} at 40 m depth between the hours of 0500 and 0600 and 2000 and 2100 (Figure 5.3). This agrees well with the values previously mentioned as typical of sustainable swimming speeds for zooplankton within Juan de Fuca Strait. The twenty-minute mean of the vertical velocity (Figure 4.10) shows no noticeable diurnal signal indicative of zooplankton migration, suggesting that the measured vertical velocities are not biased by the active migration of zooplankton.

a) Estimated Bias

To estimate the effect that zooplankton are expected to have on the vertical velocity, the measured velocity can be modelled as a weighted sum of the true water velocity and the zooplankton velocity, with weights proportional to the scattering cross-sectional area. At 50 m depth, the corrected intensities during dawn and dusk migrations are approximately 10 dB (i.e. a factor of 10) greater than at midnight

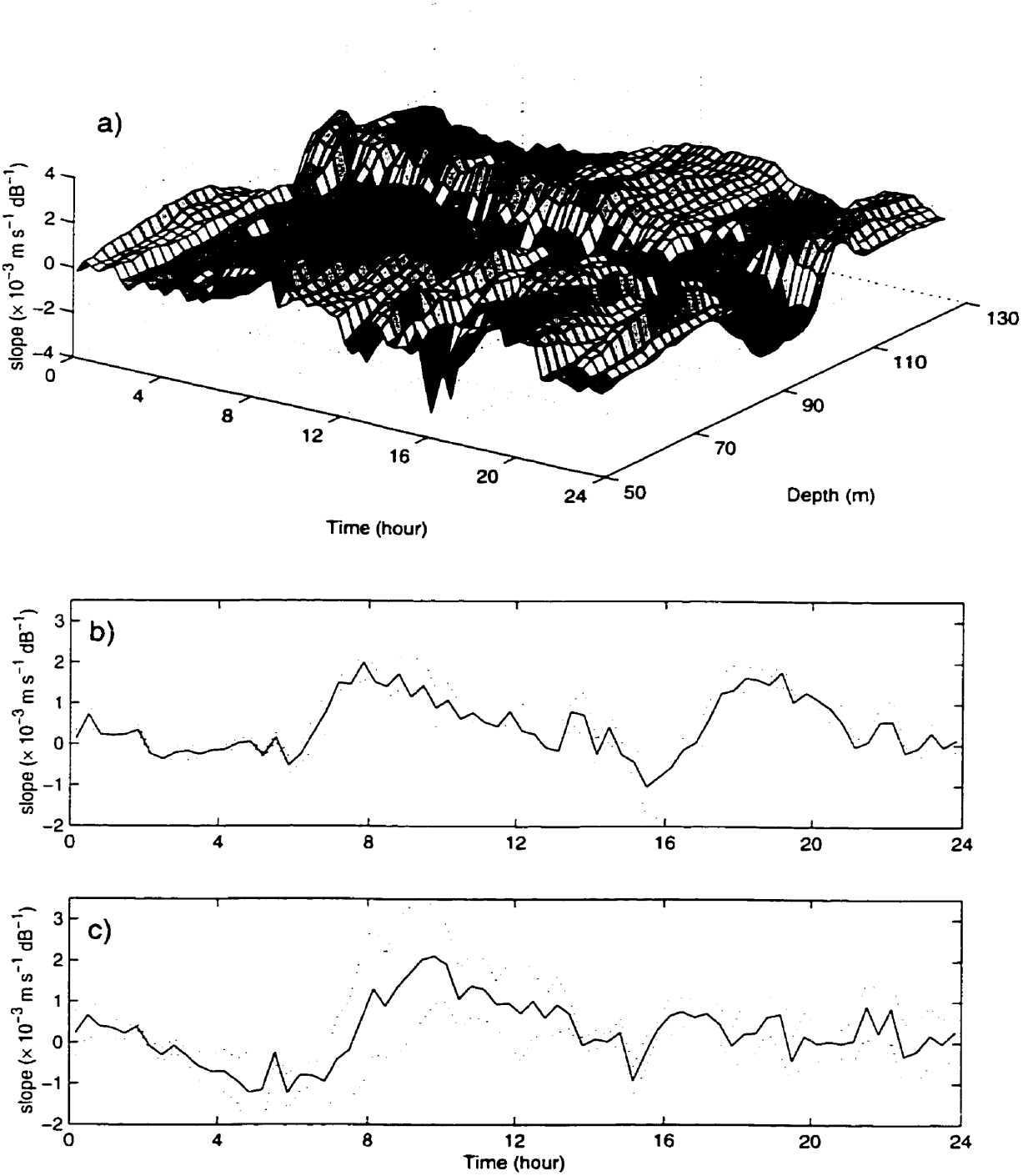

Fig. 5.4. The slopes of total vertical velocity versus corrected backscatter intensity scatterplots with time: a) in 20 minute sections over all depths for all 20 days combined, and depth average with ± 1 standard deviation from b) 50 to 70 m and c) 70 to 90 m.

(Figure 5.3). The measured vertical velocity, w_M, may then be expected to be $w_M \approx 0.1w_T + 0.9w_{zoo}$, where w_T is the true vertical velocity and w_{zoo} is the zooplankton velocity. For $w_{zoo} \approx 0.02$ m s^{-1}, a reasonable (i.e. non-averaged) migration velocity, active migration of zooplankton would lead to a bias in the recorded vertical velocity of about 0.02, 0.01, and -0.03 m s^{-1} for true vertical speeds w_T of 0, 0.01, and 0.05 m s^{-1}, respectively. In comparison, a bias of approximately 0.01 m s^{-1} would result from a pitch or roll error of 1°, given a horizontal velocity of 0.5 m s^{-1}. The migration of zooplankton is theoretically therefore just as important in causing biases in the measured vertical velocity as possible errors in the recorded tilt angles, although only at depths and times associated with the diurnal migration.

b) Backscatter versus Velocity Scatterplots

The possible effects of differential zooplankton motion can be further examined by comparing the slopes of vertical velocity against backscatter intensity scatterplots throughout the day. If zooplankton migration does affect the measured vertical velocity, these slopes should be most negative at dawn and most positive at dusk. The corrected backscatter intensity for July 31, 1996 (Figure 5.3) reveals that the strongest migrations at depth 80 m occur between the hours of 0600 and 0800 and 1800 to 2000, when zooplankton movement is downward and upward, respectively. This is true throughout the deployment, as shown by images from other days, as well as in averaged images of backscatter intensity.

An upper bound on the expected backscatter intensity versus vertical velocity slopes can be made by assuming that the true water velocity, w_T, is measured in the absence of the migrating zooplankton, i.e. for intensities of 100 dB (Figure 5.3), and the zooplankton velocities, w_{zoo}, are measured for intensities of 130 dB. Using the maximum measured vertical velocity, i.e. $w_T = 0.05$ m s^{-1}, and $w_{zoo} = -0.02$ m s^{-1}, the magnitude of the slope is at most 2×10^{-3} m s^{-1} dB^{-1}.

The backscatter intensity and vertical velocity data for the entire deployment are binned into 20-minute segments to create 72 scatterplots per depth bin. The variation in slope with depth and throughout the day reveals that slopes are most positive at 70 m depth around 0800 and negative at 90 m depth throughout a large portion of the day (Figure 5.4). Depth averages over 50 to 70 m (Figure 5.4, middle panel) and 70 to 90 m (lower panel) show that the slopes are most negative between 0300 and 0700, whereas the dawn migration begins after 0500. Likewise, while the slopes between 1800 and 2000 are positive, they are not significantly more so than between 0800 and 1000. Thus, scatterplot slopes also suggest that the effect of zooplankton migration on vertical velocities is small.

c) Composite Anomalies

Plueddemann and Pinkel (1989) examined vertically migrating layers of zooplankton in the open ocean using a ship-mounted 67 kHz ADCP. They found three distinct layers, situated at depths of 300, 560, and 1000 m during the day. Each scattering layer was found to migrate upwards a different distance over different times. Diurnal migration velocities for each layer were estimated from the backscatter data and matched well with the measured vertical velocities in regions of significant vertical motion in layers of elevated backscatter intensity (i.e when the "ratio of the intensity of migrating scatterers to that of non-migrating scatterers" (Plueddemann and Pinkel 1989) was large). That is, the vertical velocities measured the zooplankton motion.

The technique they used was to examine the standard deviation and anomaly (i.e. the difference from the time mean) of the backscatter intensity and vertical velocity fields at each depth. The advantage of removing the time mean at each depth is that there is no need to correct for sound absorption and beam spreading. The standard deviation fields are computed at each depth and time of day and measure the amount of variance throughout the length of the deployment. The standard deviation of the intensity, for example, is the square root of the log intensity variance

$$\sigma_I^2(z,t) \equiv \frac{1}{N}\sum_{n=1}^{N}[I'_n(z,t) - I'(z,t)]^2 \qquad (5.2)$$

where the backscatter intensity anomaly for the nth day, $I'_n(z,t)$, is the intensity at time t and depth z minus the mean value at that depth over all times and all N days. The composite intensity anomaly, $I'(z,t)$, measures the difference at one time of day and depth from the overall mean at that depth, $\overline{I}(z)$. That is,

$$\begin{aligned} \overline{I}(z) &\equiv \frac{1}{J}\sum_{j=1}^{J}\frac{1}{N}\sum_{n=1}^{N} I_n(z, j\Delta t) \\ I'_n(z,t) &\equiv I_n(z,t) - \overline{I}(z) \\ I'(z,t) &\equiv \frac{1}{N}\sum_{n=1}^{N} I'_n(z,t) \end{aligned} \tag{5.3}$$

with J the number of measurements per day, and Δt the time between measurements. The standard deviation and anomaly fields for the vertical velocity are calculated in a similar manner.

For the Juan de Fuca data, where ensembles are recorded every 30 seconds, the results are averaged over 20-minute intervals. The standard deviation in backscatter intensity over the 20 days of the deployment reveals that the variations in backscatter below 50 m are larger during the day than at night (Figure 5.5). The relatively small deviations between 2200 to 0300 coincide with the periods when the zooplankton are higher in the water column. The standard deviation in w at depth, on the other hand, is low at all times compared to the major deviations between 70 and 90 m and 0800 to 1200. The standard deviation of the intensity at this time and depth is relatively small, however, and there appears to be no clear relation between the deviations.

The daily migration is clearly represented in the intensity anomaly for July 31 (Figure 5.6). The vertical velocity anomaly is very small during the evening migration and is upward during the morning downward migration, even though maximum zooplankton speeds are 0.03 m s^{-1} (from 70 to 110 m depth from 0800 to 0900). The temporal variation in the concentration of zooplankton throughout the water column is best seen in the composite intensity anomaly (Figure 5.6). The zooplankton reside above 50 m during the evening and below 90 m during daylight hours. At 60 m depth,

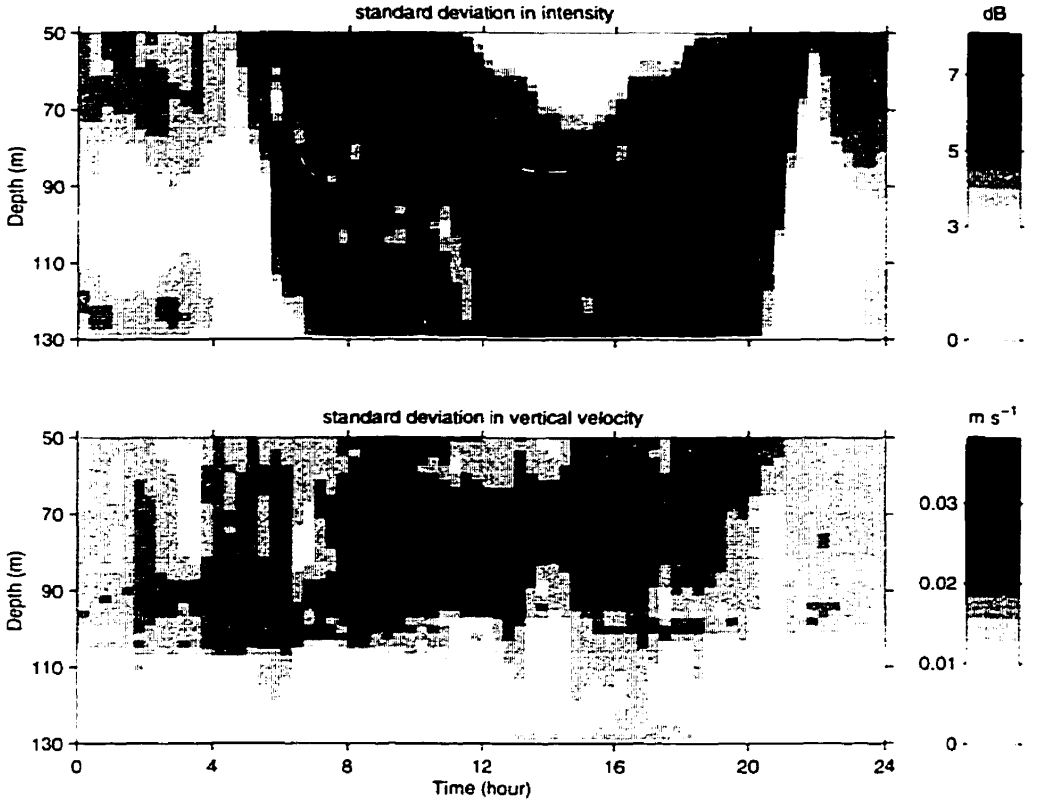

Fig. 5.5. Standard deviation in backscatter intensity and vertical velocity fields over the entire 20-day deployment.

the mean migration speed is about 0.01 m s^{-1}; the averaging inherent in the calculation of the composite anomaly fields reduces the zooplankton velocities, which were, for example, calculated to be closer to 0.02 m s^{-1} on Julian day 213 (Figure 5.3). The downward dawn migration centred at 0600 is again coincident with upward vertical anomalies. While the upward migration at 2100 between 50 and 70 m depth is mirrored in the vertical velocity, the peak in w is smaller in magnitude than peaks at 0500 and 0900 at 90 m depth for which no downward migration of zooplankton is expected. Unlike the findings of Plueddemann and Pinkel (1989) therefore, in Juan de Fuca Strait the bias in the measured vertical velocity due to migrating zooplankton is small, and is not important over much of the water column throughout most of the day.

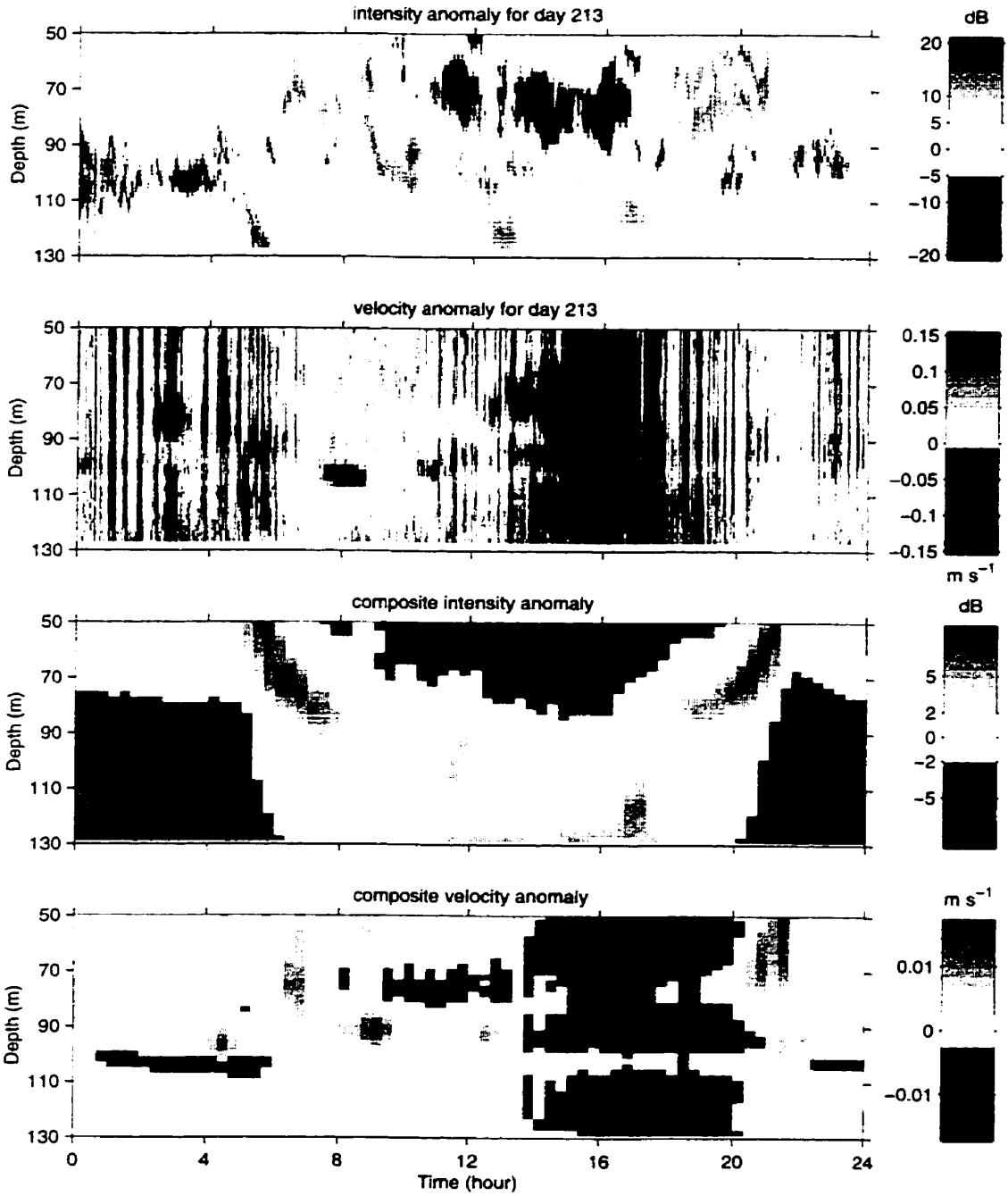

Fig. 5.6. Backscatter intensity and vertical velocity anomaly fields for July 31, 1996 and composite anomaly fields over the 20-day deployment.

5.4 Internal Waves

Layers of backscatter intensity can also be followed over much shorter time scales, when zooplankton motion is assumed to be passive and where internal waves can be used as a test of the measured vertical velocity. During late afternoon on July 17, 1997 (Figure 5.7), one such large internal wave passed above the moored ADCP, appearing as a regular undulation in a layer of anomalously large backscatter intensity. Here, it is assumed that the zooplankton do not move en masse relative to the water over vertical amplitudes of 10 m with periods of 10 minutes. These internal wave motions were observed at various depths and times of the day during which the diel migration does not occur, making it unlikely that differential zooplankton motion exists. It is further assumed that the observed undulating structure is associated with vertical displacements of density surfaces rather than horizontal advection past the ADCP site. A sinusoidally-shaped layer of increased backscatter intensity of amplitude 10 m and wavelength 200 m (i.e. vertical slopes in the elevated intensity layer of 0.2) advected by an along-channel velocity of 0.2 m s^{-1}, typical of several of these internal wave episodes, would mimic the observed structure, but it is unlikely such a spatial pattern would exist over several wavelengths. The zooplankton are thus believed to model the movement of truly passive tracers in the flow field.

Superimposed on the upper image (Figure 5.7) are lines indicating the integrated vertical velocity. If the vertical velocity measurements are accurate, these η surfaces will also track passive tracers. Below 90 m, the surfaces closely follow the layers of different corrected backscatter intensity, implying that the ADCP vertical velocity is a good measure of the true vertical current. That is, the vertical velocity was not greatly contaminated by the horizontal velocity, and there is no bias in the ADCP roll and pitch measurements. As a further example, consider the η surfaces which converge at 70 m depth at 16.8 hours past midnight (Figure 5.7). The expected rise in the local concentration of particulates is clearly seen in the increase of

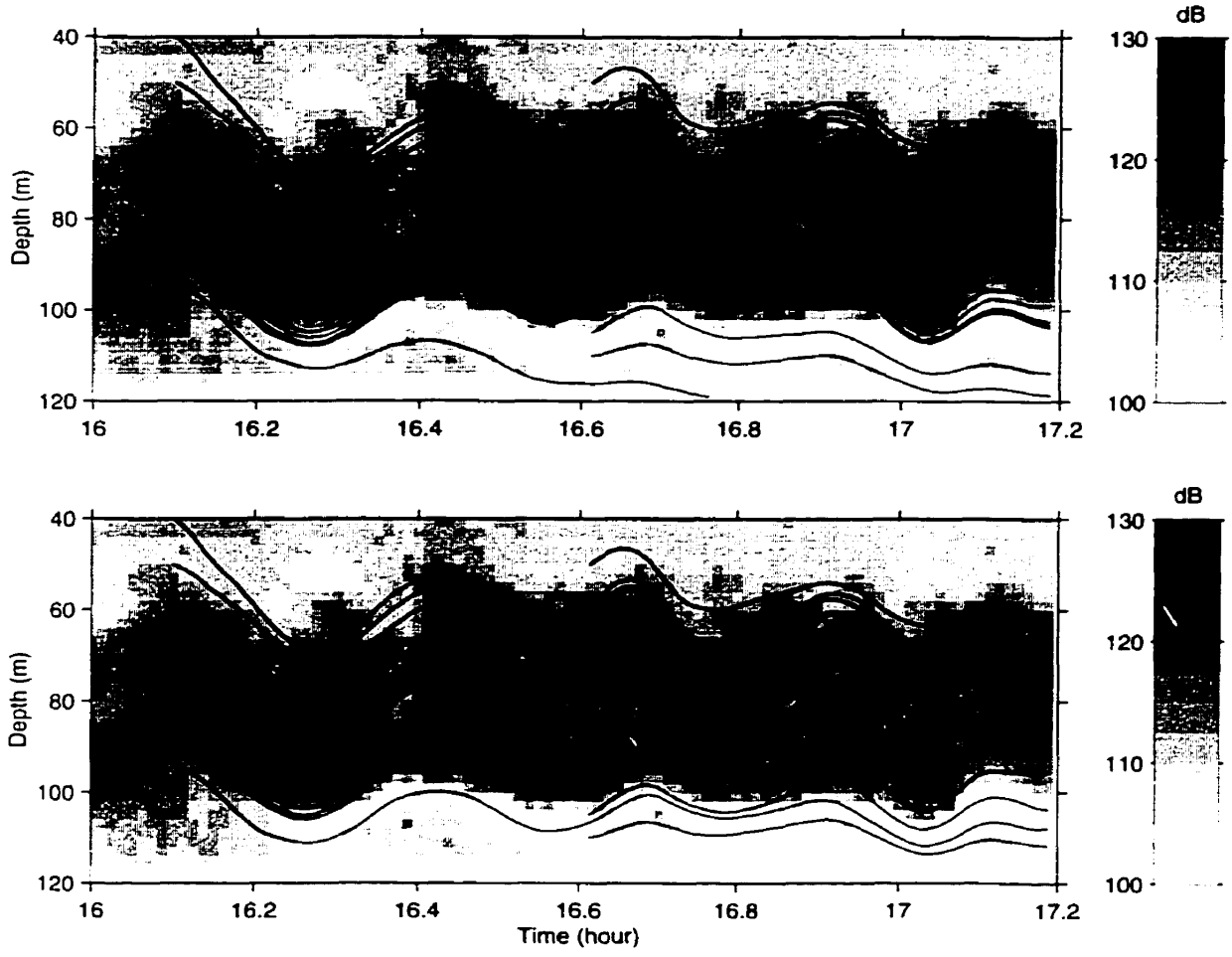

Fig. 5.7. Backscatter intensity and integrated velocity surfaces. In a) the measured vertical velocity is used, while in b) the vertical velocity is contaminated with horizontal currents by rotating it 0.5° degrees from the vertical.

the backscatter intensity. This layer then oscillates vertically, as do the integrated η surfaces around it.

Unfortunately, internal waves are only observed near slack tide, and a similar analysis cannot be performed at peak flood or ebb. At these times, errors in pitch or roll would lead to the largest contamination of w by the horizontal velocities. Comparing the upper and lower panels (Figure 5.7), however, one can see considerable differences in the integrated η surfaces for small rotations of the along-channel vertical

axes. In the lower panel, the vertical velocity used is purposely 'contaminated' with the horizontal current by rotating the (x, z) axes 0.5°. The η surfaces around 90 m depth diverge considerably between 1600 and 1700, despite the fact that large intensity layers appear in this region (at 90 m depth and 1700, for example). Further integration (i.e. until 2100, during the initial transition to a weak ebb) reveals that, for the rotated axes, all of the η surfaces dive into the bottom, while for the original orientation, the surfaces remain at mid-depth. Rotations of -0.5° lead to even worse results, with the η surfaces rising above 40 m before 1700. The ADCP vertical velocity is thus seen to be free of contamination from horizontal velocities and therefore a true measure of the actual vertical velocity.

5.5 Summary

It has been shown that the measured vertical velocity accurately describes the movement of high-intensity backscatter regions at times when the zooplankton are not actively migrating. Furthermore, no obvious bias in the measured velocity was seen during times of migration compared to non-migration periods, even though the ten-fold increase in the backscatter intensity during migration regimes should lead to large biases. The reasons for this are not known, but the reliability of w measurements gives confidence in the following analysis of vertical tides and residual velocities, as well as in the estimation of Reynolds stresses.

Chapter 6

Tides

Tides were obtained from the 21-day ADCP current meter records using a standard tidal analysis package (Foreman 1976) which includes spectral analysis to determine the confidence intervals for constituent magnitudes and phases. In a harmonic analysis, the number of constituents which can be independently determined increases with the record length of the data. The Rayleigh criterion requires that only constituents separated from each other by at least a complete period over the length of the data be included in the analysis, although "it has been argued that the Rayleigh criterion is unnecessarily restrictive where instrumental noise and the background meteorological noise are low" (Pugh 1987). In fact, Godin (1972) suggests that for oceanic tides, it is "routine" to use a Rayleigh coefficient of 0.8 (i.e. requiring that constituents be separated by only 80% of a complete period over the deployment), and that it is possible to go lower still, depending on the noise intensity and measurement accuracy available. In practical terms, the Foreman analysis involves inverting the constituent matrix: increasing the rank by reducing the Rayleigh coefficient also increases the degree to which it is ill-conditioned.

For analysis of the 1996 ADCP current data the Rayleigh coefficient was reduced from 1 to 0.75. This increased the number of tidal harmonics evaluated from 18 to 30: 11 astronomical, 18 shallow-water, and the mean (Table 6.1). Unacceptably low return signal strength was found over a significant fraction of the day (when zooplankton are outside the euphotic zone) above 40 m depth (Figure 5.3). The RDI software considers these beam velocities to be unreliable, and the resulting three-dimensional velocity is flagged as bad. Evaluation of tidal and residual currents is therefore restricted to depths below 40 m.

Table 6.1. Tidal Constituents Used in Tidal Analysis

Harmonic	Period (hr)	Harmonic	Period (hr)	Harmonic	Period (hr)
MSF	354.367	N2	12.658	MS4	6.103
2Q1	28.006	M2	12.421	S4	6.000
Q1	26.868	S2	12.000	2MK5	4.931
O1	25.819	ETA2	11.754	2SK5	4.797
NO1	24.833	MO3	8.386	2MN6	4.166
K1	23.935	M3	8.280	M6	4.140
J1	23.098	MK3	8.177	2MS6	4.092
OO1	22.306	SK3	7.993	2SM6	4.046
UPS1	21.578	MN4	6.269	3MK7	3.530
		M4	6.210	M8	3.105

A two-dimensional (i.e. horizontal) tidal constituent can be modelled either by resolving the current into two components along perpendicular axes or by representing the current as two current magnitudes rotating in opposite directions. In the former case, with the axes rotated through an inclination θ, positive anticlockwise, from (east,north),

$$u_h \equiv u + iv = u_{maj} \cos(\omega t + o) + iu_{min} \sin(\omega t + o) \qquad (6.1)$$

where u_{maj} and u_{min} are the semi-major and semi-minor axes, respectively, ω is the frequency, and o is the phase difference, or lag, relative to time $t = 0$. Here, $u_{min} > 0$ indicates that the current vector is rotating in the anticlockwise sense, $u_{min} = 0$ for a rectilinear current, and $u_{min} < 0$ represents a clockwise rotating current; by convention, u_{maj} is positive. Alternatively,

$$u_h = R^+ e^{i(\omega t+\psi^+)} + R^- e^{-i(\omega t+\psi^-)} \quad (6.2)$$

where the positive real numbers R^+ and R^- are the magnitudes of the anticlockwise and clockwise rotating vectors, respectively, and ψ^+ and ψ^- are the corresponding phase leads, relative to the x axis, which is generally taken to be eastward. The relationship between the two representations is straightforward: $R^+ = (u_{maj} + u_{min})/2$, $R^- = (u_{maj} - u_{min})/2$, $\psi^+ = \theta + \phi$, and $\psi^- = \theta - \phi$. Anticlockwise, rectilinear, and clockwise rotating currents are denoted by $R^+ > R^-$, $R^+ = R^-$, and $R^+ < R^-$, respectively.

6.1 Tidal Constituents

The $M2$ harmonic (Figure 6.1) is the largest in magnitude at all depths. Maximum along-axis flows occur at 110 m depth, 5 m below the zero in cross-axis flow (indicating rectilinear flow). The minimum at 85 m is likely due to the presence of internal tides, while the decrease below 110 m reveals the effects of bottom friction. Cross-axis currents are large both near the bottom, where the $M2$ current rotates in an anticlockwise sense ($u_{min} < 0$), and at mid-depths, where rotation is clockwise. The along-axis direction (inclination) of the $M2$ tidal ellipse rotates with depth from 9° to 2° south of due east from the bottom to mid-depth (86 m), and then back to 20° south of east at 40 m. The tidal lag increases with height above the bottom until 86 m depth, at which point the tide arrives approximately 35 minutes later than at the bottom. The tidal lag then decreases with height, and at 40 m, the tidal phase is approximately zero relative to that of the bottom current, with the $M2$ tide at 40 m leading in time by 3 ± 6 minutes.

$K1$ (Figure 6.1) is the next largest tidal constituent, with maximal along-axis currents occuring at both 110 and 70 m depths. The $K1$ tidal current is near-rectilinear throughout much of the water column, with significant cross-channel flows

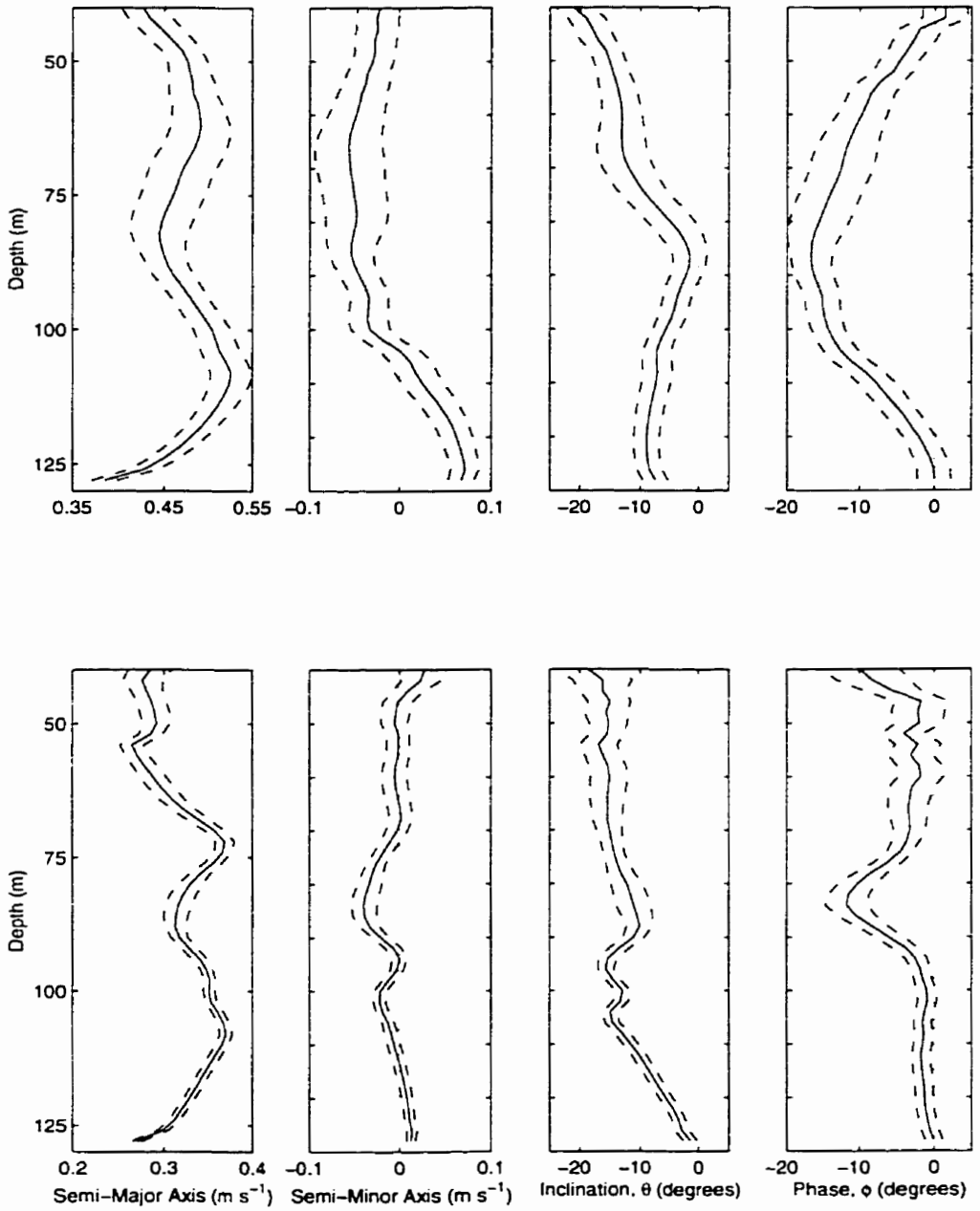

Fig. 6.1. Tidal ellipse parameters for the $M2$ (upper panels) and $K1$ (lower panels) constituents of the horizontal velocity. Dashed lines indicate the 95% confidence intervals. The inclination is the angle between the semi-major axis and due east, with positive angles implying anticlockwise. Negative relative phases indicate the current at depth lags that at the bottom.

at 85 m, and weaker maxima near both 100 m (where $M2$ is rectilinear) and the bottom. As with the $M2$ constituent, the $K1$ tidal current rotates in an anticlockwise sense near the bottom, and is essentially clockwise at all depths (where there is significant cross-axis flow) above 110 m. The ellipse orientation also rotates from 3° to 20° south of east, though not in a manner consistent with the $M2$ ellipse: the along-axis direction is most nearly east-west at the bottom. The tidal lag also increases with height, although to a much lesser extent than for the $M2$ constituent. The phase difference between $K1$ at the bottom and at 96 m is less than 2°, or 8 minutes, which is comparable to the size of the error bars. The tide turns latest at 86 m depth, 45 minutes after the bottom. Thereafter, the lag is diminished; above 56 m, the phase appears to be unreliable.

Of the remaining harmonics, only the astronomical constituents $O1$, $N2$, and $S2$ have along- and cross-axis currents consistently larger than 0.10 m s^{-1} and 0.02 m s^{-1}, respectively, with cross-axis tides reaching 0.07 m s^{-1} for $S2$ at 80 m depth. Rotation of the along-axis direction with depth and depth dependence of the current magnitudes, both along- and cross-axis, are prevalent in all three constituents. The $N2$ tide is rectilinear at the bottom, but otherwise rotates in a clockwise sense throughout the water column. In contrast, the $O1$ tide appears to flip its rotation sense several times, although negative values of the minor axis are never significantly different from zero (similar to the $K1$ tide).

6.2 Bottom Friction

The presence of bottom friction is clearly seen in the phases and amplitudes of the $M2$ and $K1$ (Figure 6.1) tidal constituents. In each case, the tide turns first at the bottom, and the amplitude maximum occurs 22 m above the bottom, below which the tidal currents weaken at a rate which increases with proximity to the solid boundary, as expected for a log-layer.

6.2.1 Log-Layer Fitting

Log-layer fits to the 20-minute averaged total current are found by minimising the rms difference between the measured currents and those predicted by (2.12). Initially, only three current bins (of 2 metre depth each and centred at 5, 7, and 9 m above the bottom) were used to estimate u_* and z_o. For fits in which the difference at any one depth is greater than 1% of the actual current, the log-layer is assumed to be less than 9 m high, if it exists at all. Otherwise, additional bins are added one at a time, and new fits are determined, until the difference of 1% is exceeded. This method of fitting was used by Lu (1997) who argued that the "1% criterion is compatible with the confidence intervals of the mean velocity estimates". Only average velocities from each 35 ping burst over 10 seconds were recorded by the ADCP, so it is not possible to determine the degrees of freedom (i.e. the decorrelation time) within an ensemble. The decorrelation time for the high-passed along-channel velocity was found to be between 30 and 60 seconds on both the accelerating and decelerating stages of flood and ebb tides. That is, the number of degrees of freedom is roughly half the number of measurements in an average. Specifically, V, the "variance inflation factor" (Wilks 1997) which is given by

$$V = 1 + 2\sum_{k=1}^{n-1}\left(1 - \frac{k}{n}\right) r_k \tag{6.3}$$

where n is the number of measurements in a sample and r_k is the estimated auto-correlation at lag k, is $V \approx 2.2$ for the measured velocity in Juan de Fuca Strait, for spring, ebb, and slack tide. This factor is a measure of the effective sample size, n_e, with $n_e = n/V$ (Wilks 1997).

Assuming that the uncertainty in an ensemble measurement is 0.02 m s^{-1}, the uncertainty claimed by RDI and found by Lu (1997) for an individual ping, averaging 18 (i.e. 40/2.2) independent measurements reduces the uncertainty to approximately 0.005 m s^{-1}. This is approximately 1% of a typical mean velocity used in the log-layer fitting.

Over the 20 complete days of deployment, a log-layer of at least 9 m height was found on 1086 occasions of the 1440 20-minute mean current profiles, although for 84 of these fits z_o exceeded 0.1 m. In a compiled list taken from many sources, Soulsby (1990) shows that z_o values vary from 5×10^{-5} m for silt to 3×10^{-3} m for gravel to 6×10^{-3} m for rippled sand, suggesting that large values of z_o are indicative of a mathematical rather than a physically reasonable log-layer fit. Although large roughness parameters can be indicative of processes other than roughness-generated turbulence, such as form drag on larger scale bedforms, the effect should be felt more strongly for stronger flows. There was, however, low correlation ($r = -0.22$) between the roughness scale and the magnitude of the reference velocity in general, with all large values of z_o found during weak currents (i.e. the magnitude of U_{11} was less than 0.15 m s^{-1} for all cases where $z_o > 1$ m).

The friction and reference velocities were well correlated ($r = 0.97$) for all fits where $z_o < 0.1$ m (Figure 6.2), with the square of the slope ($C_D = u_*^2/U_{11}^2$) for the best fit line having zero intercept implying $C_D = 3.1 \times 10^{-3}$. There was essentially zero correlation between z_o and the magnitude of the reference velocity, indicating that the roughness scale is indeed independent of the overlying flow. The drop in the number of log-layer fits with increasing log-layer height (Figure 6.2) suggests that some of the profiles which did not satisfy the log-layer analysis may have, in fact, been logarithmic with log-layer heights less than 9 m. Decreasing the ADCP bin size to 1 m, for example, would have enabled the log-layer analysis to be performed to heights within 6 m of the bottom. The log-layer height z_h was found to be correlated with both U_{11} ($r = 0.54$) and u_* ($r = 0.57$). This is to be expected, as the log layer is destroyed every time the tide turns and regrows as the tide strengthens. The correlation is not exact, however, because the ever changing current does not allow the layer height to reach equilibrium. The slope for the z_h to u_* fit implies that the log-layer height satisfies $z_h = 0.020u_*/f$, or $z_h = 0.025u_*/\omega_{M2}$, where ω_{M2} is the frequency of the dominant tidal constituent. Tennekes (1973) suggested that

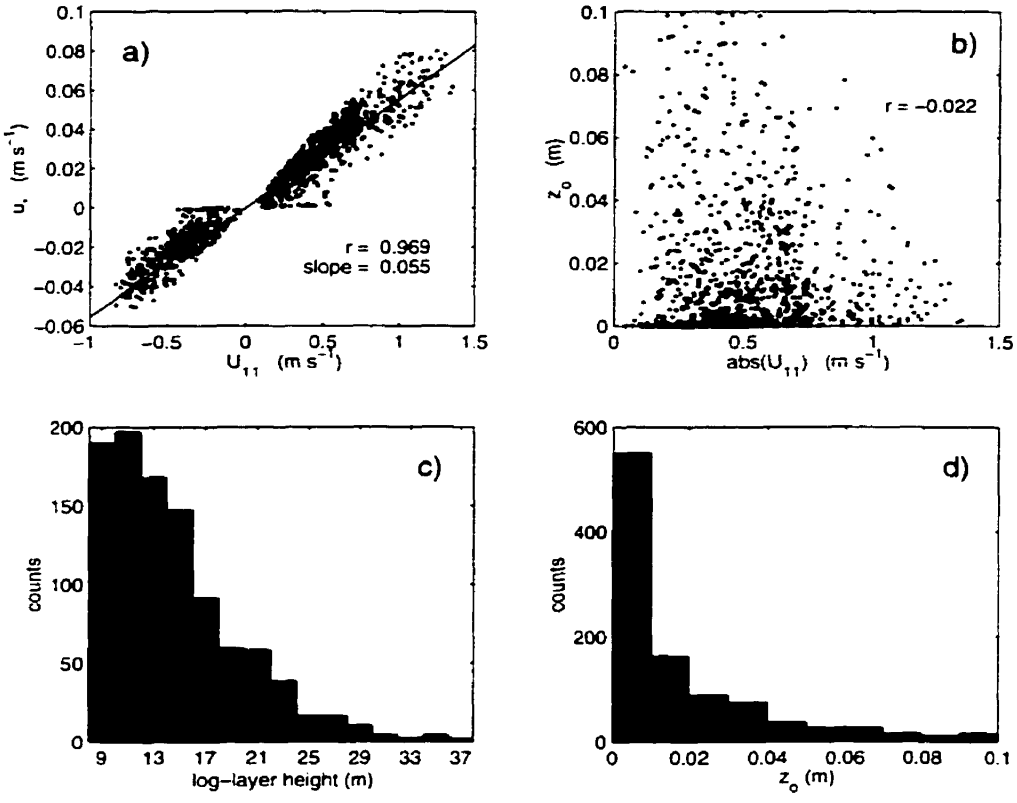

Fig. 6.2. Log-layer fit to the bottom current: a) the friction velocity versus the reference velocity (measured 11 m above the bottom), b) the roughness parameter versus the magnitude of the reference velocity, c) histogram of the log-layer height, and d) histogram of the roughness parameter. Fits for which z_o exceeds 0.1 m have been omitted, leaving 1002 log-layer fits out of the 1440 20-minute mean current profiles.

the log-layer height for a steady planetary boundary layer is $z_h = 0.030u_*/f$, while Soulsby (1983) found $z_h = 0.040u_*/f$.

For the 609 log-layer fits out of 862 20-minute means where $U_{11} > 0$, the correlation coefficient between u_* and U_{11} was $r = 0.90$, and the slope for zero intercept implied $C_D = 3.6 \times 10^{-3}$, while $r = 0.82$ and $C_D = 2.9 \times 10^{-3}$ for the 393 fits out of 578 where $U_{11} < 0$. When z_o is set to 0.006 m (the roughness parameter which gives the most log-layer fits), 38% of the current profiles can be matched to log-layers within the 1% criterion. Ignoring instances when the reference current is less than

0.2 m s^{-1} in magnitude, for which there are very few fits, a full 50% of the mean velocity profiles can be fit to log-layers of height 9 m or greater for $z_o = 0.006$ m. The calculated drag coefficients are $C_D = 2.9 \times 10^{-3}$ during flood and $C_D = 2.8 \times 10^{-3}$ during ebb.

In summary, the log-layer fits for which z_o was not constrained appeared to show that the drag coefficient is substantially larger on flood tides than during ebbs. The drag coefficients found when the roughness parameter was set to 0.006 m, however, are very similar. This is consistent with the fact that while z_o was uncorrelated with the reference velocity for both flood and ebb, the few large values were associated with weaker currents. This is unlikely to be due to suspended sediment, which is expected to increase z_o, because the turbidity should increase with larger currents. The roughness parameter can also vary as the length scale of the current increases, changing the topography which the current feels. Although this cannot be quantified as bottom mapping was not done in the region in which the ADCP was deployed, this effect is also likely to be felt primarily during stronger flows. Further evidence of erroneous fits is provided by the scarcity during weak currents of log-layer fits for which $z_o = 0.006$ m. Log-layers may not yet be established or may not extend to a height (9 m in the present study) which allows for log-layer analysis just after the tide turns, and because the tide turns first at the bottom, a log-layer analysis may not be realistic on the decelerating tide.

In determining the drag coefficients from the slopes of the friction velocity to reference velocity fits, the intercept was set to zero. For each of the above fits the intercept of the polynomial fit of u_* to the reference velocity was found to be extremely small (e.g. between 7×10^{-5} m s^{-1} for ebb tide with $z_o \equiv 0.006$ m and 2×10^{-3} m s^{-1} for the combined ebb and flood fits with z_o unconstrained). This is reassuring, as the bottom stress should vanish as the overlying current approaches zero. The drag coefficients are not altered to the precision with which they were calculated (i.e. 10^{-4}).

A roughness parameter of $z_o = 0.006$ m is consistent with a bottom composed of rippled sand (Soulsby 1990), slightly larger than one of gravel, for which $z_o = 0.003$ m, and over an order of magnitude larger than one of mud. The bottom in the region surrounding the ADCP was at least partly made up of mud as evidenced by the amount stuck within the ADCP housing upon recovery. The large roughness parameter suggests that the mud may be rippled, although no bottom surveys were done so the exact composition and bathymetry of the region is unknown.

6.2.2 The Bottom Boundary Layer

Soulsby (1983) built upon the log-layer literature to analyse tidal currents in a well-mixed bottom boundary layer. He simplified the analysis by parameterising the Reynolds stress, and considered both rectilinear flow and flow where the Coriolis effect leads to veering with height.

a) The Oscillatory Boundary Layer

For rectilinear oscillatory flow in deep (non-rotating) unstratified fluid over a flat bed, Soulsby (1983) rewrote the equation of motion

$$\frac{\partial U}{\partial t} = \frac{1}{\rho}\frac{\partial \tau_{xz}}{\partial z} - g\frac{\partial \zeta(t)}{\partial x} \tag{6.4}$$

where τ_{xz} is the Reynolds stress and $\zeta(t)$ is the sinusoidally varying surface slope, by using the eddy viscosity parameterisation ($\tau_{xz} = A_v\, \partial U/\partial z$), as

$$i\omega \boldsymbol{U} = \frac{\partial}{\partial z}(A_v \frac{\partial \boldsymbol{U}}{\partial z}) - g\boldsymbol{S} \tag{6.5}$$

where $\boldsymbol{U}$ and $\boldsymbol{S}$ are the complex amplitudes such that $U = \Re[\boldsymbol{U}\exp(i\omega t)]$ and $\partial\zeta/\partial x = \Re[\boldsymbol{S}\exp(i\omega t)]$, and bold is used for the complex terms to distinguish them from the real component. The eddy viscosity, A_v, varies with height above the bottom as well as over the tidal cycle. Analytic solutions, however, require that A_v be held constant in time, since time dependence leads to non-linearities. For quasi-steady flow, $A_v \approx \kappa z u_*(t)$, although models with time-varying A_v (Lavelle and Mofjeld

1983: Davies 1986) show that A_v values midway between these two parameterisations (i.e. between fully time-varying and time-independent) are most appropriate. For oscillatory planetary flow, discussed in the next section, Fang and Ichiye (1983) found that the eddy viscosity lagged the tidal current by up to 30 minutes.

Using a time-invariant eddy viscosity of the form $A_v = \kappa u_{*m} z$ (with u_{*m} the friction velocity at maximum tide), the solution for $\boldsymbol{U}$ is given by (Soulsby 1983)

$$\boldsymbol{U} = \boldsymbol{U}_\infty \left\{ \left[1 - \frac{ker\xi ker\xi_o + kei\xi kei\xi_o}{ker^2\xi_o + kei^2\xi_o} \right] + i \left[\frac{ker\xi kei\xi_o + kei\xi ker\xi_o}{ker^2\xi_o + kei^2\xi_o} \right] \right\} \tag{6.6}$$

where *ker* and *kei* are the Kelvin functions, $\xi^2 = 4\omega z/\kappa u_{*m}$ is the scaled height above the bottom, $\xi_o^2 = 4\omega z_o/\kappa u_{*m}$ is the scaled roughness, and $\boldsymbol{U}_\infty = (ig/\omega)\,\boldsymbol{S}$ is the free-stream solution (i.e. outside the boundary layer whose height is given by $\delta_U = u_*/\omega$).

Fitting a log-layer to the semi-major axis of the $M2$ tide (Figure 6.3), in the same manner done previously for the total current, yields $u_* = 0.024$ m s^{-1} and $z_o = 0.003$ m, i.e. a roughness scale half of that estimated in the previous section for the total current. The observed $M2$ profile matches the log-layer within 1% up to 108 m depth, a 22 m range. $\boldsymbol{U}_\infty$ is set to 0.555 m s^{-1} to best match the solution (6.6) to the observed $M2$ constituent, and differences below 108 m depth are less than 1.3% (0.006 m s^{-1}). The Soulsby fit is improved slightly when z_o is set to 0.006 m. In this case, $u_* = 0.026$ m s^{-1}, and $\boldsymbol{U}_\infty = 0.565$ m s^{-1} (Figure 6.3). The maximum surface slope corresponding to either fit is $\partial\zeta/\partial x \approx 8 \times 10^{-6}$, equivalent to a pressure gradient of $\partial p/\partial x \approx 0.08$ Pa m^{-1}, about 100 times larger than that due to Fraser River discharge, as determined from atmospheric pressure and sea level data (Figure 3.4).

Although $\delta_U = u_*/\omega \approx 170$ m ($u_* = 0.024$ m s^{-1}) is greater than the water depth, the profile reaches 99% of its free-stream value $\boldsymbol{U}_\infty$ at 78 m depth (i.e. 52 m above the bottom), and 95% at a depth of 100 m. Above 100 m, however, the water column is no longer well-mixed (Figure 4.2). The oscillatory boundary layer is

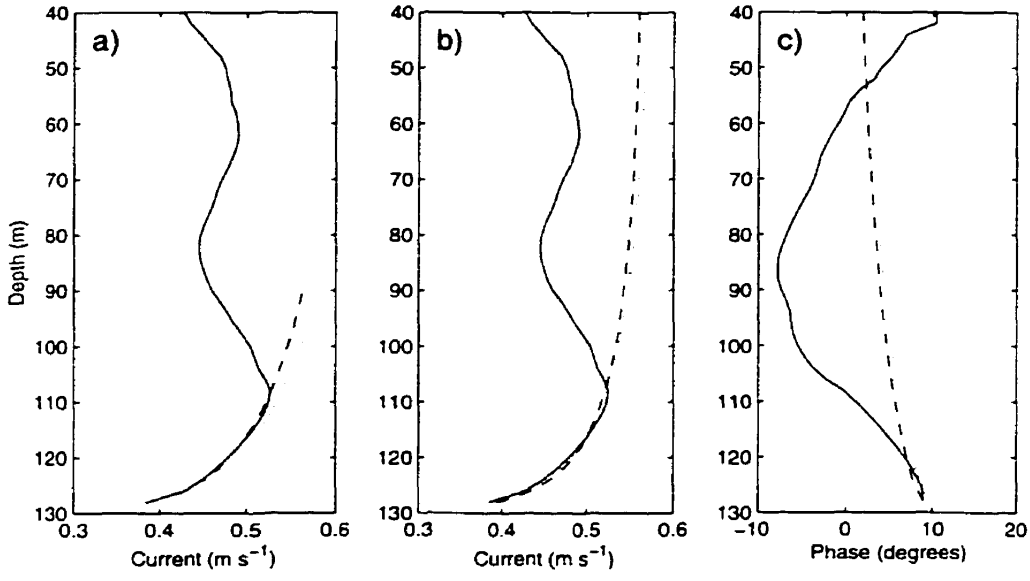

Fig. 6.3. Oscillatory boundary layer fit to the semi-major axis of the $M2$ tidal ellipse. In a), log-layer fits to the measured $M2$ (solid line) yield $u_* = 0.024$ m s^{-1} and $z_o = 0.003$ m (dashed line) when z_o is unconstrained and $u_* = 0.026$ m s^{-1} when z_o is set to 0.006 m (dotted line). The resulting magnitude and phase of the Soulsby (1983) oscillatory boundary layer solution to the tide is shown in b) and c), respectively.

capped at 100 m and the results are not applicable higher in the water column since the Soulsby analysis assumes constant density. While the model and measured tidal magnitude agree very well in the lower part of the well-mixed layer, the theoretical phase prediction, $\tan^{-1}\{\Im(\boldsymbol{U})/\Re(\boldsymbol{U})\}$, is not as good (Figure 6.3). In the lowest 7 metres, the model overpredicts the rate of change of phase with height, and at 7 m above the bottom, the predicted phase is about 0.5° less than that observed. Above 120 m depth, the model underpredicts the phase difference relative to the bottom by as much as 10°. This may be a consequence of the fact that the well-mixed bottom layer is not truly homogeneous or of the fact that the total current only partly consists of the $M2$ tidal component.

Strictly speaking, rotational effects are negligible only where $\omega \gg f$, whereas at the latitude of Juan de Fuca Strait, $\omega/f \approx 1.3$. Nevertheless, the effect of the Coriolis force on barotropic tides within sea channels whose width is small compared to the Rossby radius of deformation is often of secondary importance, and the "existence [of a purely oscillatory boundary layer] is commonly assumed in the modelling of tidal estuaries" (Soulsby 1983). However, other assumptions made in the development of the model are more troublesome. The advective terms were omitted from (6.5), although a mean estuarine circulation clearly exists in Juan de Fuca Strait. In addition, the current is measured above a submarine hill as opposed to a flat bottom.

b) The Effect of Rotation

The flip in rotation sense of the $M2$ tidal ellipse below 105 m can be due neither to linear combinations of the internal modes (the horizontal currents associated with the first three baroclinic modes are nearly constant below 100 m) nor to friction acting on the cross-channel flow directly. Rather, it may be the result of a breakdown in the geostrophic balance inside the well-mixed bottom layer, where the tidally induced pressure gradient remains constant with depth while the along-channel $M2$ tide is retarded by bottom friction. Accelerations in the cross-channel direction can be determined from the simplified v–momentum equation: $v_t + fu = -p_y/\rho_o$, where subscripts indicate derivatives. Consider the balance at 105 m (Figure 6.1) during maximum flood tide, with the along-channel $M2$ current $u \approx 0.55$ m s^{-1}, and $v \approx 0$ (implying $v_t \approx 0$). The pressure gradient is thus $p_y \approx -0.55 f \rho_o$. Stratification below 100 m is sufficiently small at station C7 (Figure 6.5) that the cross-channel pressure gradient is essentially constant with depth. Therefore, at 125 m depth, where $u \approx 0.45$ m s^{-1}, $v_t + 0.45f \approx 0.55f$. Integrating over three hours, v is of the order $0.1f \times 3 \times 3600$, or 0.1 m s^{-1}, roughly the difference in cross-channel velocity between these depths (Figure 6.1). The northward acceleration implies that the ellipse should rotate in an anticlockwise direction in the bottom boundary layer, in agreement with the data.

c) Oscillatory Planetary Flow

The previous analysis of rectilinear oscillatory boundary layer flow can be extended to include the Coriolis effect (Prandle 1982; Bowden *et al.* 1959). In this case, the clockwise and anticlockwise rotary components of the tide are modelled separately, and the equation of motion analogous to (6.5) becomes

$$\frac{\partial \boldsymbol{Q}}{\partial t} + if\boldsymbol{Q} = \frac{\partial}{\partial z}(A_v \frac{\partial \boldsymbol{U}}{\partial z}) - g\boldsymbol{S} \tag{6.7}$$

where $\boldsymbol{Q} = U + iV$, and $\boldsymbol{S} = \partial\zeta/\partial x + i\partial\zeta/\partial y$. For the two rotary components, this becomes

$$\begin{aligned} i(\omega + f)\boldsymbol{R}^+ &= \frac{\partial}{\partial z}(A_v \frac{\partial \boldsymbol{R}^+}{\partial z}) - g\boldsymbol{S}^+ \\ -i(\omega - f)\boldsymbol{R}^- &= \frac{\partial}{\partial z}(A_v \frac{\partial \boldsymbol{R}^-}{\partial z}) - g\boldsymbol{S}^- \end{aligned} \tag{6.8}$$

where $R^+ = \Re[\boldsymbol{R}^+ e^{i\omega t}]$, $R^- = \Re[\boldsymbol{R}^- e^{-i\omega t}]$, $S^+ = \Re[\boldsymbol{S}^+ e^{i\omega t}]$, and $S^- = \Re[\boldsymbol{S}^- e^{-i\omega t}]$. The freestream values are given by $\boldsymbol{R}^+_\infty = ig\boldsymbol{S}^+/(\omega + f)$ and $\boldsymbol{R}^-_\infty = -ig\boldsymbol{S}^-/(\omega - f)$. For a linear eddy viscosity distribution (i.e. $A_v = \kappa u_* z$), the solutions are again given by (6.6), although the parameters are somewhat different. For the (anticlockwise,clockwise) rotating components, $\boldsymbol{U}$, $\boldsymbol{U}_\infty$, $\boldsymbol{S}$, and ω (in ξ and ξ_o) in (6.6) become $(\boldsymbol{R}^+, \boldsymbol{R}^-)$, $(\boldsymbol{R}^+_\infty, \boldsymbol{R}^-_\infty)$, $(\boldsymbol{S}^+, \boldsymbol{S}^-)$, and $(\omega + f, \omega - f)$, respectively.

The solutions for the two rotating components (Figure 6.4) are found using u_* and z_o parameters from log-layer fits to each component separately. As the magnitudes of the two components are different in Juan de Fuca Strait, one would expect the friction velocities to be different. The roughness scales, however, should be reasonably similar in value. The log layer fits are indicated by the shorter lines, extending to 90 m depth, in Figure 6.4, while the boundary layer magnitudes and phases are denoted by the longer lines. The results are summarised in Table 6.2.

The boundary layer height is sensitive to the choice of friction velocity and roughness parameter, but in both cases, the prediction is somewhat closer to the observed data for the anticlockwise ($\boldsymbol{R}^+$) as opposed to the clockwise component.

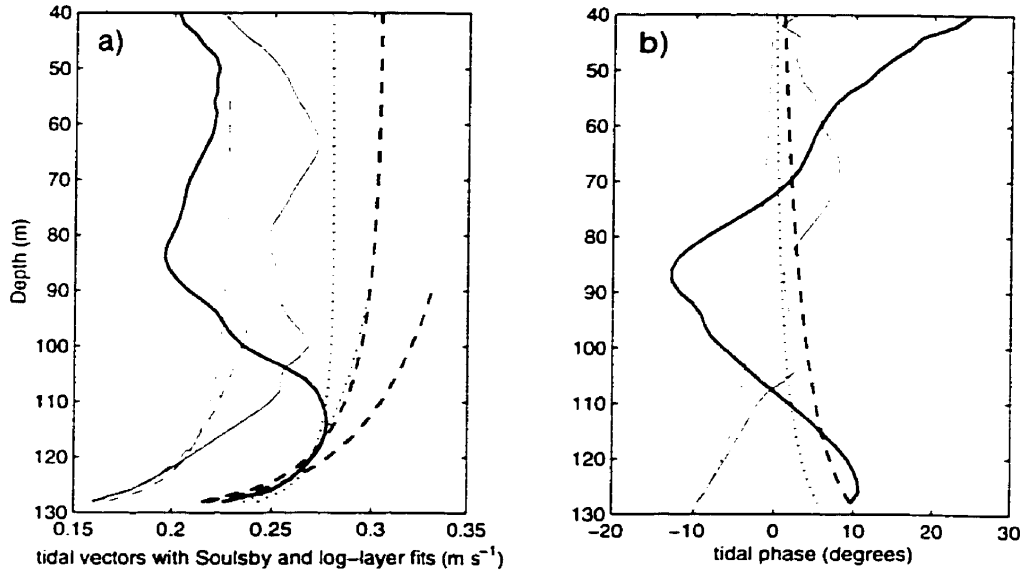

Fig. 6.4. Oscillatory boundary layer fit to the anticlockwise (thick lines) and clockwise (thin lines) rotary components of the $M2$ tidal ellipse: a) magnitude and b) phase. Solid lines are data, dashed lines represent the best model fit, and dotted lines represent the fit for z_o set to 0.006 m. The shorter lines in a) represent the log-layer fit to the magnitude only, used to determine u_* and z_o.

For the best fit log-layer (the first two data columns in Table 6.2), the boundary layer height $\delta^+ = u_*/(\omega + f) \approx 30$ m is an order of magnitude smaller than $\delta^- = u_*/(\omega - f) \approx 450$ m. This fit, however, does not appear to be physical. Not only is the roughness parameter three orders of magnitude larger for the clockwise rotary component, but the frictional velocity is larger as well, even though the data suggest that the near bottom stress is smaller (Figure 6.4).

Setting $z_o = 0.006$ m for both rotary components leads to more reasonable values for the friction velocity (Table 6.2). The anticlockwise boundary layer thickness is doubled to $\delta^+ \approx 60$ m, but is still much smaller than δ^-. The freestream velocities ($\boldsymbol{R}_\infty^+$ and $\boldsymbol{R}_\infty^-$) are not very sensitive to changes in the u_* and z_o parameters.

In the lowest 10 metres, the clockwise phase is fairly well predicted for both choices of the u_* and z_o parameters (Figure 6.4). (The measured phase is relative, and since stratification above the bottom layer means the phase need not go to zero

Table 6.2. Oscillatory Boundary Layer Model for the $M2$ tide

	$\boldsymbol{R}^+$	$\boldsymbol{R}^-$	$\boldsymbol{R}^+$	$\boldsymbol{R}^-$
u_* ($\times 10^{-3}$ m s^{-1})	8.26	13.78	15.03	11.03
z_o ($\times 10^{-3}$ m)	0.02*	23.32*	6.0†	6.0†
log-layer height (m)	17	13	9	9
boundary layer height δ (m)	33	451	60	362
99% velocity height (m)	17	37	35	27
free stream velocity (m s^{-1})	0.28	0.23	0.30	0.22

* free parameter

† constrained

with height, the measured phase can be shifted to coincide with the prediction for $z_o = 0.006$ m.) The mismatch in the anticlockwise phase is similar to that of the earlier results for rectilinear flow (Figure 6.3) but the magnitude of the error is larger.

Both components reach 99% of their freestream values close to the top of the well-mixed layer, although $\boldsymbol{R}^-$ is less than typical measured mid-depth values, while $\boldsymbol{R}^+$ is considerably greater. In other words, the predicted along-channel and cross-channel $M2$ tidal magnitudes of 0.52 and 0.08 m s^{-1}, respectively, are not seen throughout most of the water column. Above the well-mixed bottom layer, however, the structures of the internal tidal modes vary with depth and the model cannot be expected to account for internal modes. In addition, baroclinic modes are caused by the interaction of the main tide with topography, belying the earlier assumption of a flat-bottom. That internal tides exist in the along-channel direction can be seen in the deviation of the actual $M2$ tide from that predicted by the simpler analysis of rectilinear oscillatory flow (Figure 6.3). The second panel suggests that the combined magnitude of the internal $M2$ tides should be of the order 0.1 m s^{-1}.

6.3 Internal Tides

Spectra of residual (de-tided) currents show considerable energy at frequencies both slightly higher and lower than those associated with the main tidal periods. This smearing of energy is indicative of internal tides (Wunsch 1975; Pugh 1987). While internal tides are necessarily generated at tidal frequencies through the interaction of deep-sea tides with topography, their phase relative to the barotropic tide may vary in time owing to the changing hydrographic structure within the strait. This effect increases with distance from the generation site(s), because phase speeds also depend on the density profile, resulting in the further broadening of spectral bands in the tidal energy spectra around tidal frequencies. Internal tides are fairly strong in Juan de Fuca Strait, as clearly seen in the variation with depth (above the bottom boundary layer, where bottom friction retards flow, altering even the barotropic component) of the magnitude of individual harmonics such as $M2$ and $K1$ (Figure 6.1); the $O1$, $N2$, $P1$, and $S2$ harmonics exhibit similar variations in magnitude with depth.

The vertical structure of the modes is calculated by numerically integrating the Taylor-Goldstein relation (2.36). The first and second derivatives (w_z and w_{zz}) are each discretised using a second-order centred scheme, and the shooting method is used to find the eigenvalues of c which satisfy the boundary conditions. With N typically of order 10^{-2} s^{-1} within Juan de Fuca Strait, the hydrostatic approximation ($\omega^2 \ll N^2$) is clearly satisfied for the $M2$ tidal component, where $\omega \approx 10^{-4}$ s^{-1}. Similarly, the Coriolis parameter f varies by only 0.4% from its mean value of 1.1×10^{-4} s^{-1} within the strait, justifying the use of the f-plane assumption.

The actual density profiles used in calculating the vertical modes at each CTD station are the mean of at least 4 CTD casts taken at each site over the two week deployment. Prior to averaging, spikes in the individual calculated σ_t, caused by mismatches in the response times of the thermistor and conductivity sensors, are removed and the profiles are sorted (increasing density with depth) to obtain the equilibrium density. Spike removal involves identifying large jumps in density (greater

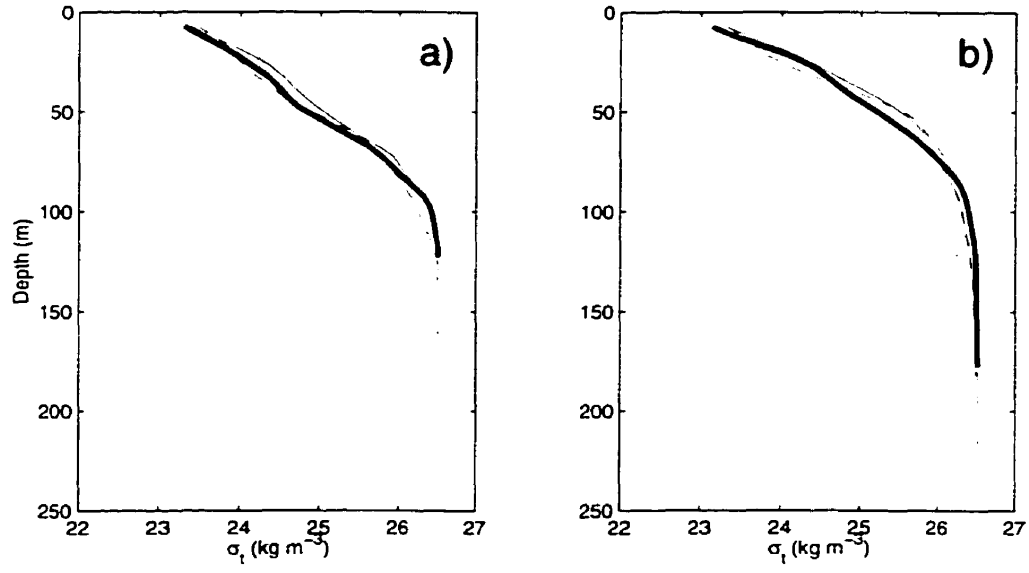

Fig. 6.5. Variation in the mean density profiles in the a) cross-channel direction: Stations C6 (thin solid), C7 (thick solid), and C8 (thin dash), and b) along-channel direction: A4 (thin solid), A5 (thick solid), and A6 (thin dash).

than 0.2 kg m^{-3}) over regions of small (less than 2 m) vertical extent and replacing them with values interpolated linearly from values just above and below.

The variation in density profiles in the along- and cross-channel directions (Figure 6.5) is small over the 27 km separating CTD Stations A4 and A6 and the 5 km separating Stations C6 and C8, respectively. The lack of a strong along-channel dependence in the stratification in the central part of Juan de Fuca Strait is consistent with the constancy of density profiles during the time series taken above the ADCP site (Figure 4.3) and indicates that the modal structure is relatively independent of the along-channel location. There is slightly more variation in the cross-channel direction, due to the sloping interface and the effect of the sidewall just to the north of Station C8, but the effect on the first few baroclinic modes for the $M2$ tide is small (Figure 6.6).

The $M2$ tidal harmonic is reconstructed from the tidal results (major axis, minor axis, phase, and inclination) of Foreman's analysis of the 21-day 1996 ADCP

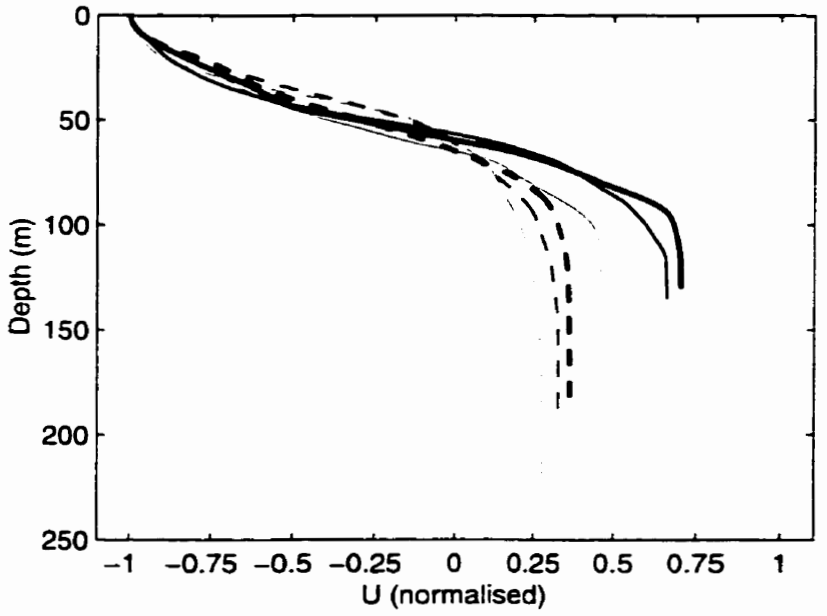

Fig. 6.6. Variation in the vertical structure of the second along-channel mode at the $M2$ frequency. The modes are calculated by integrating the Taylor-Goldstein equation with no background flow at each CTD Station: C7 (thick solid), C8 (solid), C6(thin solid), A5 (thick dash), A4 (dash), and A6 (thin dash).

current. For the purposes of fitting to the theoretical tidal modes, only currents between 108 m and 40 m depth are used: below 108 m, friction clearly affects the measured currents (Figure 6.1, first panel) and above 40 m, gaps in the current data undermine the reliability of the tidal analysis. The fit to theoretical modes is accomplished by minimising the root mean square difference between the measured $M2$ current and a linear combination of the barotropic and baroclinic modes over one tidal cycle and allows each mode to have an independent phase as well as magnitude. The results are independent of the timestep (i.e. of the number of points in the $M2$ cycle) used to recreate the tidal current.

The vertical structure of the modes calculated using the hydrography at the CTD station nearest the ADCP site (i.e. C7) changes in the presence of a background flow (Figure 6.7). The background flow used is the mean measured by the ADCP

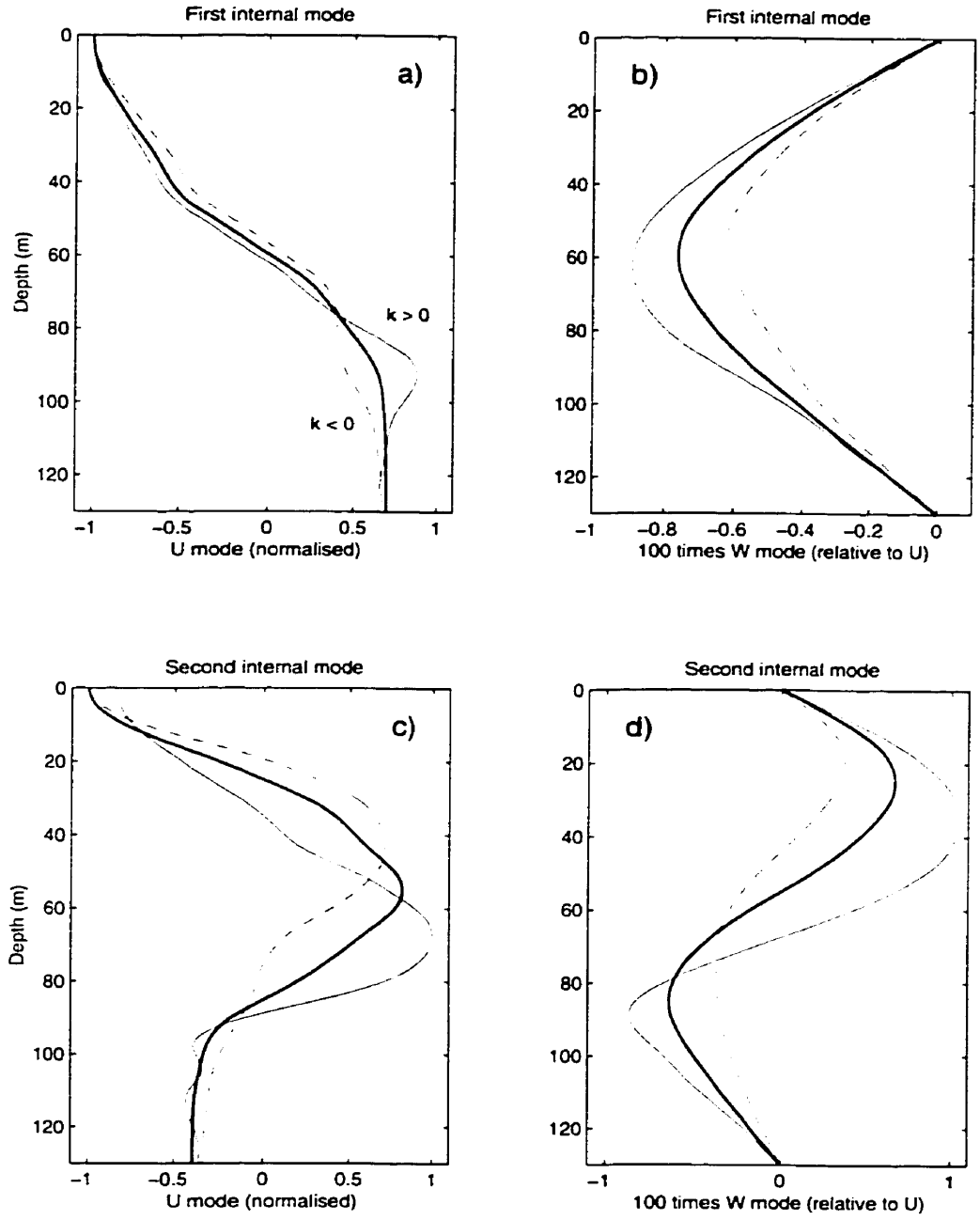

Fig. 6.7. Variation in vertical structure of $M2$ baroclinic modes at CTD station C7: a) first along-channel, b) first vertical, c) second along-channel, and d) second vertical. The modes are calculated by integrating the Taylor-Goldstein equation for no background flow (thick solid), for waves travelling in the positive x-direction (eastward) in the presence of the mean estuarine flow (thin solid), and for waves travelling in the negative x-direction (thin dashed).

(Figure 7.1) and affects incoming tidal waves differently from outgoing tides, particularly between depths of 80 to 100 m. There are, therefore, three possible profiles for each internal mode (no background flow, and $k > 0$ or $k < 0$ for a background flow).

The tidal analysis, on the other hand, does not resolve directional differences in the $M2$ tide; the resulting tidal components are in effect an average of the incoming and outgoing waves. This effect becomes more important as the asymmetry of the baroclinic tides becomes greater. Therefore the resulting modal fit can give only an approximate estimate of the strengths of the various modes.

Inviscid wavelike perturbations on a mean flow are discontinuous at critical levels, the heights at which the phase speed equals the background current (Kundu 1990). The rapid spatial variations in the perturbation currents magnifies the importance of viscosity such that "the small frictional and non-linear effects, elsewhere negligible, can play a significant role" (Pedlosky 1979). A critical layer is formed around the critical level due to viscous effects, within which wave energy and momentum is absorbed. Waves created as the mean current flows over topography cannot propagate beyond the critical layer and the resulting non-uniform momentum flux can alter the mean current. The Taylor-Goldstein modes in the presence of background velocity have critical layers for the fourth and higher baroclinic modes. The vertical resolution and measurement accuracy of the currents does not allow for mode-fitting beyond the first one or two baroclinic modes, however, so this instability cannot be examined.

In Juan de Fuca Strait, with $f \approx 1.1 \times 10^{-4}$ s^{-1}, $W \approx 2 \times 10^{4}$ m, and $H \approx 200$ m, the minimum frequency allowed for barotropic Poincaré waves corresponds to a period of about 16 minutes (2.27). The barotropic diurnal and semi-diurnal tides are therefore Kelvin waves, and have no cross-channel components. Although internal Poincaré modes do not exist at diurnal frequencies ($\omega < f$), they may exist at semi-diurnal frequencies, provided the integration constant c in (2.36) is such that the resulting wavenumber (2.32) is real. This criterion is not satisfied for the first baroclinic mode calculated with or without background flow, so the first internal modes are also Kelvin waves, just as Forrester (1974) found in the St. Lawrence. The

Table 6.3. Modal Fit (in m s^{-1}) to the Along-Channel $M2$ Tidal Amplitude

	barotropic	with 1st baroclinic		with 2nd baroclinic		
no background flow	0.47	0.48	0.08	0.65	0.38	0.19
background flow, $k > 0$	0.47	0.48	0.05	0.56	0.15	0.07
background flow, $k < 0$	0.47	0.48	0.12	0.38	0.38	0.32

second baroclinic mode has a real wavenumber for no background flow (for $m = 1$ only) and for $k > 0$ in the presence of the measured current (for $m = 1$ to 5), but not for $k < 0$ (i.e. seaward propagating). Without horizontal resolution of the tidal currents, the Kelvin and Poincaré modes cannot be separated.

6.3.1 The Along-Channel $M2$ Tide

The along-channel tidal modes (Figure 6.7) are fit to the semi-major axis of the (u, v) rotary tide (Figure 6.1) between the depths of 60 and 100 m. Using only a barotropic mode (i.e. one amplitude and phase, independent of depth), the tidal magnitude is 0.47 m s^{-1} (Table 6.3). The largest difference between the analysed $M2$ tide and the fit is 0.041 m s^{-1} (Table 6.4). This error, about 10% of the barotropic tide, is slightly larger than the mean uncertainty (based on the 95% confidence interval between 60 and 100 m depth) in the amplitude of the semi-major axis of approximately 0.027 m s^{-1} (Figure 6.1).

A minimisation involving the first baroclinic mode in addition to the barotropic mode does not reduce the largest difference. The amplitude of the barotropic mode is essentially unchanged from that found for the barotropic fit, while the strength of the baroclinic mode varies from 0.05 to 0.12 m s^{-1}. Adding the second internal mode reduces the errors considerably, although the fact that the baroclinic modal

Table 6.4. RMS and Largest Difference (m s^{-1}) to the Along-Channel Modal Fit

	barotropic		with 1st baroclinic		with 2nd baroclinic	
no background flow	0.017	0.041	0.014	0.041	0.010	0.027
background flow, $k > 0$	0.017	0.041	0.013	0.040	0.004	0.017
background flow, $k < 0$	0.017	0.041	0.015	0.041	0.013	0.033

magnitudes are of the order of the barotropic tide suggests that the fits for no background flow and for $k < 0$ are erroneous. The remaining fit is also the one with the lowest errors, less than those associated with the measurement of the $M2$ tide. The barotropic magnitude, 0.56 m s^{-1} is in rough agreement with the oscillatory planetary model, i.e. $\boldsymbol{R}^{+} + \boldsymbol{R}^{-} = 0.52$ m s^{-1} (Table 6.2). However, an eastward moving Kelvin wave would be largest at the southern coast and the phase speed of $c_2 \approx 0.3$ m s^{-1}, obtained as the constant of integration (2.36), corresponds to an internal Rossby deformation radius of $R_2 \approx 3 \times 10^3$ m. That is, the horizontal velocities associated with this mode would be over 10 m s^{-1} (2.30) at the south coast. The data, then, are not adequate to analyse the second internal modes, and only the first baroclinic mode is considered.

Errors inherent in the hydrography and current measurements ensure that there are differences between the measured tidal currents and the modal fit. Furthermore, the Taylor-Goldstein modes assume uniform topography and stratification, and are therefore themselves estimates. Horizontal resolution of the currents would provide an independent method of determining the direction of propagation of the internal modes. While there are several historical data sets in the same area comprised of a number of current meter stations across the strait, they unfortunately have low vertical resolution.

Table 6.5. $M2$ Parameters from 1973 data (with 95% confidence interval)

station	semi-major axis (m s^{-1})	semi-minor axis (m s^{-1})	phase	orientation
115 (50 m)	0.46 (0.01)	+0.002 (0.01)	336°	154°
115 (100 m)	0.24 (0.05)	+0.004 (0.05)	262°	154°
112 (50 m)	0.51 (0.01)	−0.033 (0.01)	332°	159°
112 (100 m)	0.34 (0.10)	−0.028 (0.10)	288°	172°

In 1973, for example, a line of six stations was occupied between Jordan River, B.C. and Pillar Point, WA. with CMDR current meters at depths of 15 and 50 m at each station, as well as at 100 and 150 m for the inner four. Ignoring current meters that failed or that were within 20 m of the bottom (where friction significantly alters the tides), concurrent hourly currents at more than one depth per station were found only at stations 112 and 115 (Figure 3.5). Deployment 2 was chosen to more accurately reproduce the 1996 conditions. The records at 50 and 100 m depth were 33 days in duration, although the data at 100 m from station 115 had a 9-day gap in the middle. A tidal analysis using the Foreman routines was used to determine the magnitude and phase of the $M2$ components (Table 6.5) and the barotropic and baroclinic modes calculated using 1996 hydrography from CTD stations C3 and C8 were then fit to the $M2$ tide.

Fitting only the barotropic mode to the observed $M2$ tide, the magnitudes were found to be 0.29 and 0.40 m s^{-1} at stations 115 and 112, respectively (Table 6.6). As the width of the strait is much less than the (barotropic) Rossby radius of deformation ($Ro \approx 400$ km), inviscid theory states that the magnitude of the barotropic tide should be essentially uniform ($e^{-W/Ro} \approx 0.95$, where W is the width of the strait). However, station 115 is only 3.3 km away from the southern boundary, while station 112 is 6.6 km south of the northern side of the strait, and sidewall friction may reduce the

Table 6.6. Modal Fit (in m s^{-1}) to the 1973 $M2$ Tide

	barotropic	with 1st baroclinic	
115	0.29	0.35	1.55
112	0.40	0.43	0.42

barotropic tidal magnitude from that in the middle of the channel. For an oscillating flow, horizontal boundary layers extend a distance $\delta \approx \sqrt{A_h/\omega}$ from the sidewalls, with ω the tidal frequency. For a horizontal eddy viscosity of $A_h \approx 10^3$ $m^2 s^{-1}$, $\delta \approx 3$ km, while $\delta \approx 8$ km for $A_h \approx 10^4$ $m^2 s^{-1}$. This suggests that the barotropic tide at station 115 may be retarded by the southern coast. While the effect on station 112 is likely to be small, the barotropic magnitude found is similar to that from 1996, with the difference likely due to the fact that the currents are measured at only two depths.

Fitting the barotropic and first baroclinic tides reveals larger baroclinicity at the south mooring (Table 6.6). The decrease in baroclinic mode strength from station 115 to station 112 is that expected by inviscid theory, given a Rossby radius of deformation for the first baroclinic mode, $R_1 \approx 10^4$ m and a station separation of 1.3×10^4 m (i.e. $e^{-1.3} \approx 0.42/1.55$). That is, the situation is consistent with the existence of an inviscid baroclinic mode trapped against the southern wall with none against the northern wall. This result is unrealistic, however, as the baroclinic mode is much larger than the barotropic mode, and a factor of five (i.e. at station 112) larger than was found in 1996. Furthermore, the measured difference in magnitude of the total $M2$ tide between 50 and 100 m depth (Table 6.5) is very similar for stations 112 and 115. With only two currents at each station, the fits become 'perfect' in the sense that all the variance can be explained by only two modes. The vertical

resolution in the historical data is insufficient to accurately determine the strength of the along-channel baroclinic tides.

6.3.2 The Cross-Channel $M2$ Tide

Although the along-channel $M2$ currents are relatively unchanged with small angle rotations, the choice of orientation significantly alters the magnitude of the much smaller cross-channel components (Figure 6.1). Given the large uncertainty in the calculated semi-major axes (50% as measured by the 95% confidence interval), determination of the cross-channel modal magnitudes is less reliable than is the case for the along-channel direction.

Another difficulty is that although bottom currents in the along-channel direction are energetic enough to supply the potential energy needed to rise above the submarine hill underneath the ADCP unit, tidal currents in the cross-channel direction, which are maximum when the along-channel component is zero, are more likely to be deflected around the bump. (The blocking height, or maximum height that can be overcome is $H_{max} = U/N$, where U is the current speed and N is the buoyancy frequency.) With $N \approx 10^{-2}$ s^{-1} between depths of 100 and 150 m at the nearest deeper CTD station (station C8), bottom along- and cross-channel currents of 0.4 and 0.1 m s^{-1} (Figure 5.1), respectively, lead to blocking heights of 40 and 10 m, whereas the topography underneath the ADCP rises approximately 30 m above the surrounding depths). Thus, modal structures calculated for the ADCP site may not accurately reflect the true cross-channel current structure.

As Forrester (1974) noted, the barotropic and first baroclinic cross-channel modes do not exist in a channel of width and latitude similar to Juan de Fuca Strait. The best-fit second baroclinic mode on the semi-minor axis $M2$ current (Figure 6.1) has a magnitude of 0.05 m s^{-1}, where for reasons explained above, the structure without background flow has been used. However, the amount of variance explained, about 60%, is comparable to that for a first baroclinic mode of magnitude 0.06 m s^{-1} (i.e. similar to that found for the along-channel tide) and is less than that for

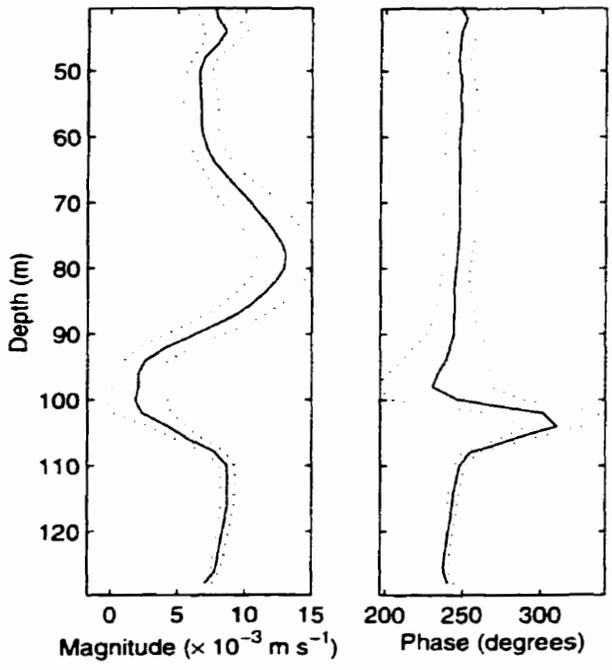

Fig. 6.8. Tidal parameters for the $M2$ constituent of the vertical velocity (with 95% confidence intervals).

a cross-channel barotropic tide of magnitude 0.04 m s^{-1}. That is, the structure of the measured tidal current cannot distinguish between the barotropic and first two baroclinic modes. Additional data, such as currents above 40 m depth or measurements at more than one location, are needed to properly fit the modes to the observed cross-channel currents at tidal frequencies.

6.3.3 The Vertical $M2$ Tide

The measured $M2$ vertical velocity is roughly two orders of magnitude less than the along-channel component (Figure 6.8), and the phase above the bottom mixed layer is much more uniform (Figure 6.1). If the best fit first baroclinic vertical mode is out of phase with the associated horizontal mode, as should be the case for a Kelvin wave, the direction of propagation can be determined.

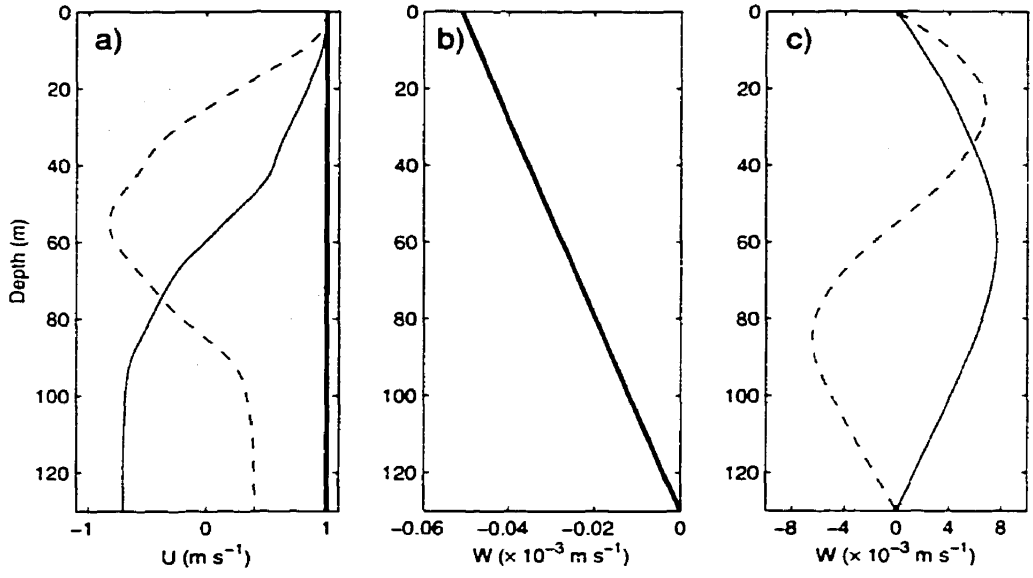

Fig. 6.9. Magnitude of the a) horizontal and corresponding b) barotropic and c) baroclinic vertical modes (from the Taylor-Goldstein equation) at station C7. For a tidal wave travelling in the positive (negative) direction, the vertical velocities shown occur a quarter period after (before) the horizontal velocities.

Multiplying the calculated vertical barotropic Taylor-Goldstein mode (Figure 6.9) by the barotropic horizontal tidal magnitude, about 0.5 m s^{-1}, implies a maximum vertical velocity of 3×10^{-5} m s^{-1} at the surface, negligible compared to both the mean of, and depth variations in, the observed vertical tide of roughly 5×10^{-3} m s^{-1}.

Fitting the first baroclinic mode yields a magnitude of 1.34 (compared to 0.05 to 0.15 for the along-channel component, Table 6.3) and a phase lag of 66° relative to the horizontal baroclinic tide. The large magnitude is due to the fact that the observed vertical tide (Figure 6.8) has a substantially non-zero depth mean. Clearly the vertical tide has been affected by the horizontal tide, since the baroclinic vertical modes go to zero at the bottom (Figure 6.9). It was shown in Chapter 5 that horizontal contamination of the vertical velocities by the horizontal components due to possible biases in the measured pitch and roll angles does not occur. This

can also be seen by comparing the vertical tide (Figure 6.8) to the along-channel tide (Figure 6.1). While the maximum in the vertical tide at 80 m depth roughly coincides with an extremum in the horizontal tide, the extremum at 95 m is offset from that in the horizontal tide by about 10 m.

The non-uniform topography and stratification in Juan de Fuca Strait may cause the vertical structure of the (horizontal) internal modes to vary in both the along- and cross-channel directions in a manner unlike the wavelike variation assumed in governing equations such as the Taylor-Goldstein relation. The spatial variation of the horizontal internal tides near regions where topography or stratification vary rapidly can lead to vertical currents of tidal frequency which are much larger than those given by the governing equations. It is therefore not possible to determine the direction of propagation for the internal tides in Juan de Fuca Strait using the relative phase of the vertical and horizontal components.

A proper examination of the tidal modes in Juan de Fuca Strait, as was done in the St. Lawrence (Forrester 1974), therefore requires both horizontal and vertical resolution in the measured currents. In addition, the velocities associated with the calculated internal modes are typically of one sign below 60 m. Therefore, currents in the upper part of the water column would be beneficial to distinguish between the various baroclinic modes, as noted particularly in the analysis of the cross-channel tide, which appeared nearly barotropic.

Chapter 7

Mean and Non-Tidal Fluctuations

7.1 Residual Estuarine Circulation

The mean residual (de-tided) along-channel current (Figure 7.1) over the 21-day deployment shows the expected estuarine circulation; outflows in the upper layer reach -0.26 m s^{-1} at 40 m, while inflows reach 0.13 m s^{-1} in the bottom well-mixed layer. The mean current is zero at 85 m, the same depth as Labrecque *et al.* (1994) found at a similar distance from the coast using current meter data from 1973. The mean residual cross-channel (i.e. 10° east of north) current is fairly large throughout much of the water column, peaking at about -0.06 m s^{-1} (i.e. southward) at 95 m depth. The mean vertical current (note the separate scale) reveals a 20 m thick convergence layer centred (i.e. the location of the maximum slope) at 87 m, just above a 10 m thick divergence layer centred at 100 m.

7.1.1 Comparison to Geostrophic Flow

a) Along-Channel

The along-channel current is essentially unchanged by small rotations of the (u, v) axes away from the mean inclination of the $M2$ tidal ellipse, 10° south of east (Figure 7.2). The geostrophic along-channel flow, based on the stratification at several CTD stations on the C-line are also shown, for a range of cross-channel sea surface slopes, ξ_y. The geostrophic velocity varies considerably with the choice of different CTD station pairs, especially in the interfacial region at 85 m depth. The calculated currents for station pairs C6-C8 and C5-C8 are similar at the bottom and above 60 m, however, suggesting that the dynamics at mid-depths is significantly altering the hydrography. The geostrophic current between the stations C6 and C8, those directly

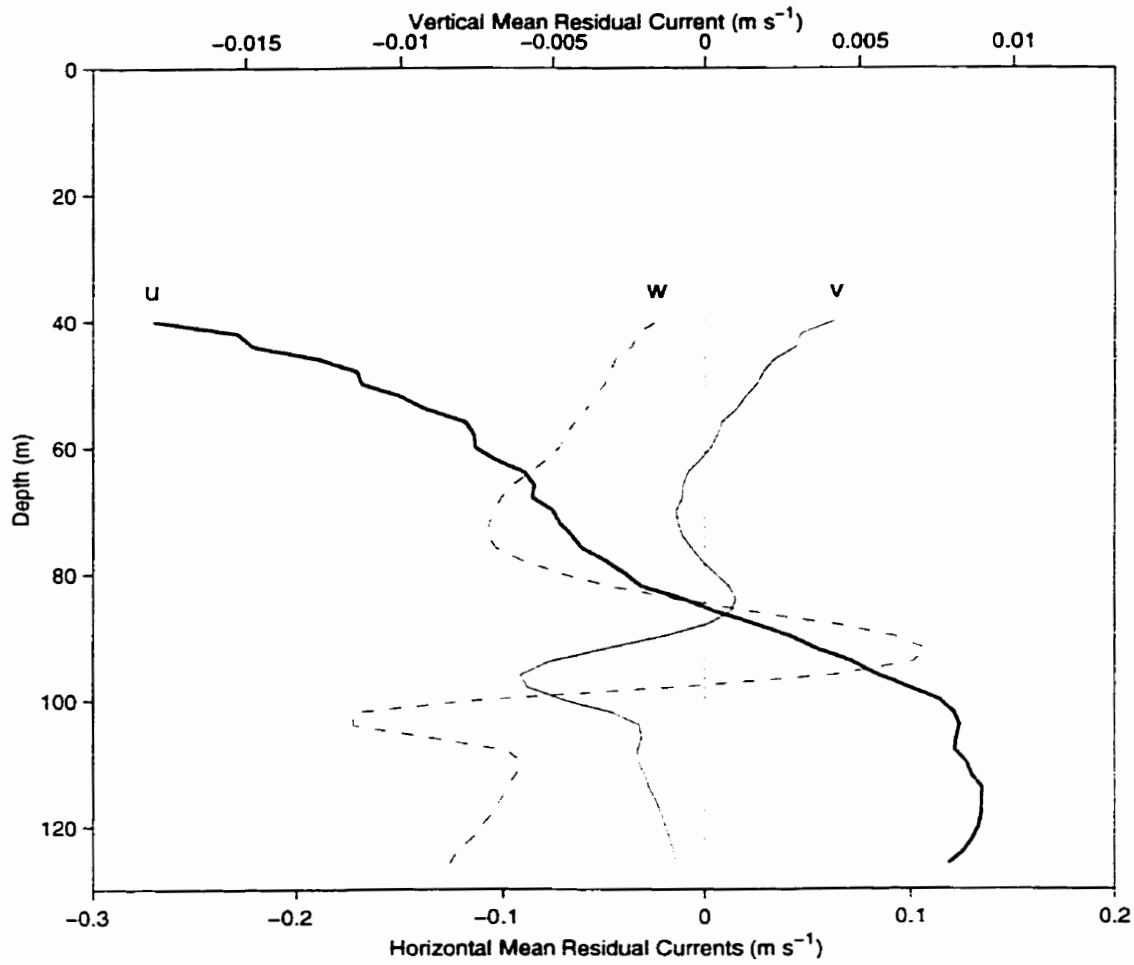

Fig. 7.1. Mean residual (i.e. detided) currents in Juan de Fuca Strait over the entire deployment. The (x, y) axes are rotated 10° clockwise from (east,north).

on either side of the ADCP, suggest that the cross-channel surface slope lies between $\xi_y \approx 2 \times 10^{-6}$ and $\xi_y \approx 2.5 \times 10^{-6}$.

The measured current does not appear to be geostrophic at any depth, with the possible exception of the region between 60 and 80 m depth if $\xi_y \approx 2.5 \times 10^{-6}$. Outside this region, the currents are larger in magnitude than geostrophic, suggesting that the exchange flow is enhanced. At the bottom, i.e. below 100 m, the large currents are unlikely to be the result of vertical convergence due to bottom topography: the

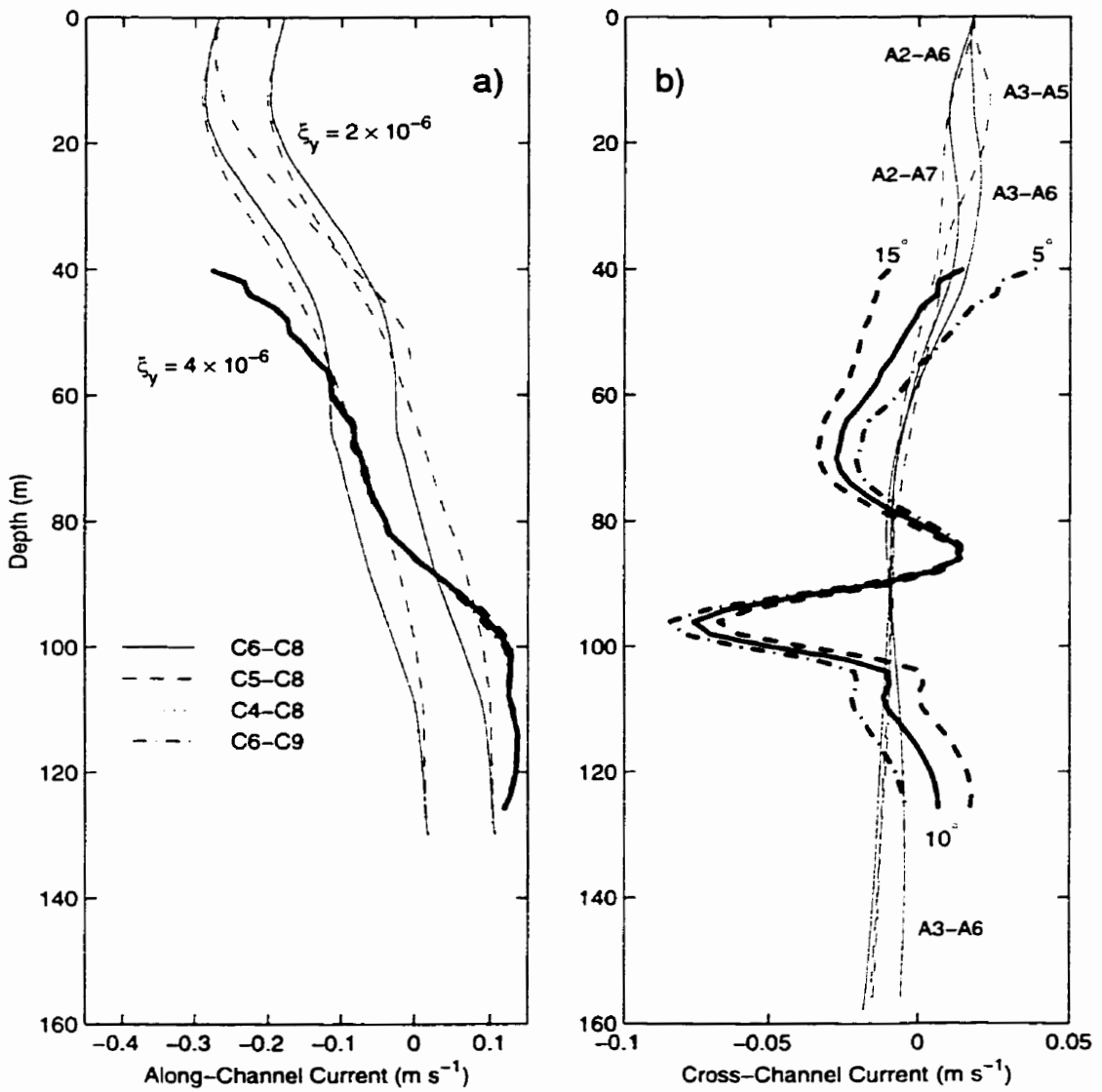

Fig. 7.2. Variation of measured a) along-channel and b) cross-channel current (thick) with axes rotation (degrees clockwise from east-north): 10 (solid), 15 (dash), and 5 (dot-dash). Also shown are the geostrophic velocities (thin). The along-channel geostrophic velocity is based on the stratification at CTD stations C4 and C8, using the cross-strait surface slopes shown, while the cross-channel geostrophic velocity is based on the hydrography at the pairs of CTD stations shown. The along-strait surface slope used, $\xi_x = 2 \times 10^{-7}$, is that for which the geostrophic and measured currents match at the top of the Ekman layer (105 m).

mean vertical current is negative and largely divergent (Figure 7.1). Unfortunately, the nearest CTD stations, C6 and C8, lie 2000 m on either side of the ADCP site and are over 1500 m away from the submarine hill, so the profiles at these sites may not be representative of the local hydrography.

b) Cross-Channel

The strong transverse currents at mid-depth remain unchanged under axes rotations of 5° (Figure 7.2), although currents in the upper and lower layers are significantly altered, raising the question of the 'true' cross-channel direction. The lack of data above 40 m makes it impossible to determine the orientation for which the mean transverse current is zero. The local depth-mean cross-channel flow may not be zero anyway due to blocking of currents by the submarine hill.

In the bottom boundary layer, the simplified momentum equation is

$$\frac{1}{\rho_o}\tau_z + fv = \frac{1}{\rho_o}p_x \tag{7.1}$$

where the acceleration and molecular viscosity terms have been omitted. Integrating from the bottom to a height h at the top of the Ekman layer yields

$$h\overline{V} = C_D u_{ref}^2 / f + h p_x / f\rho_o \tag{7.2}$$

where the total transport $h\overline{V}$ is comprised of the Ekman plus geostrophic transports. The stress at the top of the Ekman layer is zero (i.e. the current is in geostrophic balance), while that at the bottom is parameterised by $u_*^2 \approx C_D u_{ref}^2 \approx 4/\pi C_D U_T u$, where U_T is the tidal magnitude and u is the mean current.

An along-channel sea surface slope, ξ_x, is required to determine the geostrophic transport and this is found by equating the measured and geostrophic currents at the top of the Ekman layer. The geostrophic cross-channel currents calculated from various pairs of along-channel CTD stations are remarkably similar, especially below 40 m depth (Figure 7.2), and $\xi_x \approx 2 \times 10^{-7}$, where h = 105 m, the depth at which the cross-channel current profile has a sharp change.

With a total transport of $h\overline{V} = 0.01$ m^{2}s^{-1} and a geostrophic transport of -0.30 m^{2}s^{-1}, the drag coefficient is estimated to be $C_D \approx 4 \times 10^{-4}$, considerably less than the values estimated from the log-layer fits. A drag coefficient of $C_D \sim 3 \times 10^{-3}$ implies mean Ekman velocities in the lower layer of 0.12 m s^{-1}, equal to those seen in the along-channel direction. Clearly, an axes orientation of 90° is incorrect. For $C_D \sim 3 \times 10^{-3}$ and the axes orientation of 10°, the Ekman transport is balanced for a sea surface slope of $\xi_x \approx 2 \times 10^{-6}$. The resulting geostrophic currents are positive throughout the water column, with a mean value of 0.15 m s^{-1}, also not realistic. The Ekman transport cannot be closed, and the sea surface slope is taken as that for which the current at 105 m is in geostrophic balance, i.e. $\xi_x \approx 2 \times 10^{-7}$.

The sea surface pressure gradient corresponding to the surface slope, $p_x = \rho g \xi_x \approx 2 \times 10^{-3}$, is about half of the long-term mean measured in Juan de Fuca Strait from tidal sea-surface and atmospheric pressure gauges (Figure 3.4). The implication is either that the sea-surface pressure gradient is non-zero in winter, that the situation in 1996 was significantly different from the long-term mean, or that the along-channel sea-surface pressure gradient in the middle section of the strait is less than the strait as a whole. Interestingly, the results of Masson and Cummins' (1999) numerical model of the currents on the west coast of Vancouver Island and inside the Juan de Fuca Strait show that most of the sea-surface drop inside the channel occurs near the mouth, i.e. that the pressure gradient inside the strait is indeed lower.

7.1.2 Volumetric Outflow

The average freshwater input from the Fraser River was about 6200 m^3 s^{-1} for both the 20-day period centred over the middle of the ADCP record and the 20-day period one week earlier. During the summer, the Fraser contributes about 50% of the freshwater input into the Strait of Georgia. The average salinity in the upper layer (above 85 m) is 32.4 and 32.0 psu at CTD stations C4 and C8, respectively, while the lower layer mean is 33.8 psu for both stations. The volumetric outflow in Juan de Fuca Strait expected from the Knudsen relation (2.2) is $Q_1 = 12400/(1 - 32.2/33.8) \approx 0.26$

Sv, where 1 Sv (Sverdrup) $\equiv 10^6$ m^3 s^{-1}. This is approximately the same as the 0.27 Sv result Labrecque *et al.* (1994) calculated using measurements between May 16 and July 15, 1975 from a string of cross-strait moorings in the same region. The mean Fraser inflow over the period of observation in 1975 was about 7300 m^3 s^{-1}, although the relative contributions of other rivers in the region over the 1973 and 1975 deployment periods are unknown.

Without cross-channel resolution of the currents, it is not possible to independently determine the volumetric outflow in 1996, although one can make a very rough estimate by scaling the outflow found in other years by the ratio of the measured along-channel currents at a similar position in Juan de Fuca Strait. For the second deployment of 1973, when the upper layer transport was estimated to be 0.15 Sv (Table 3.1), the current at 50 m depth was approximately -0.07 m s^{-1} (Figure 3.5). The current in 1996 was about -0.16 m s^{-1}, suggesting a volumetric outflow of approximately 0.34 Sv. This is roughly consistent with the Fraser discharge (Figure 3.2) which was about 6500 and 3500 m^3 s^{-1} in late July 1996 and mid-May 1973, respectively.

An estimate of the transverse slope of the depth of zero mean along-channel flow can be made, however, via Margule's equation (3.1), again assuming that the interfacial and isopycnal slopes are similar. The density difference between the upper and lower layers is approximately 2.0 kg m^{-3} at both stations C4 and C8 in 1996, compared to 3.0 kg m^{-3} in 1975, when the geostrophic shear was also less (Table 3.1). Given a difference in geostrophic current of about 0.3 m s^{-1} (Figure 7.2), Margule's equation implies a cross-channel interfacial slope $h_y \approx 2 \times 10^{-3}$, corresponding to a difference of about 40 m across the strait. This slope can also be seen directly in the data, where the $\rho = 1026$ kg m^{-3} isopycnal, for example, slopes from 20 m to 60 m depth over 15 km (Figure 4.3). These slopes are more like those in 1973 (Table 3.1) than 1975, even though total transports are about half. The transport estimates, however, are based on only a few current meters, and may not be reliable. The upper

layer transport in 1975, for example, was calculated from only five current meters on five moorings (i.e. no vertical resolution).

7.1.3 Daily Means

Daily means of the residual along-channel current (Figure 7.3) reveal that the estuarine circulation is fairly consistent over the entire record. However, while the depth of zero mean current varies from 75 m to 90 m over the final 14 days of the deployment, it is much higher in the water column over the first six days just before neap tide, when it lies between 55 and 70 m depth. The descent in the interface at Julian day 206 is consistent with increased outflow in the upper layer due to enhanced estuarine exchange at neap tide (Griffin and LeBlond 1990). Similarities are not seen prior to the next neap at Julian day 219, however, and the depth of zero current also drops at Julian day 211. Before each of these drops in the interface, i.e. on Julian days 205 and 210, both the cross-channel and vertical velocities at mid-depth are substantially reduced compared to values elsewhere throughout the record.

7.2 Stability

The strong shears in the along- and cross-channel directions imply that the mean flow may be unstable to shear instabilities, while the daily variation in the strength of the cross-channel flows (Figure 7.3) suggests that baroclinic instability may be important in Juan de Fuca Strait. Increases in stratification stabilise the flow against both types of instability.

Below 40 m, the same-day differences in density profiles at CTD station ADCP-S (the ADCP site) on Julian days 198, 207, and 219 are of the same order as the difference in the daily mean profiles (Figure 7.4), and no clear spring-neap signal can be determined. Therefore, the overall mean stratification is used for calculations involving the baroclinic instability criterion and the Richardson number. Above 40 m, the differences in the daily means become significant, and it appears that the surface is fresher just after spring tide than after neap, in disagreement with Griffin

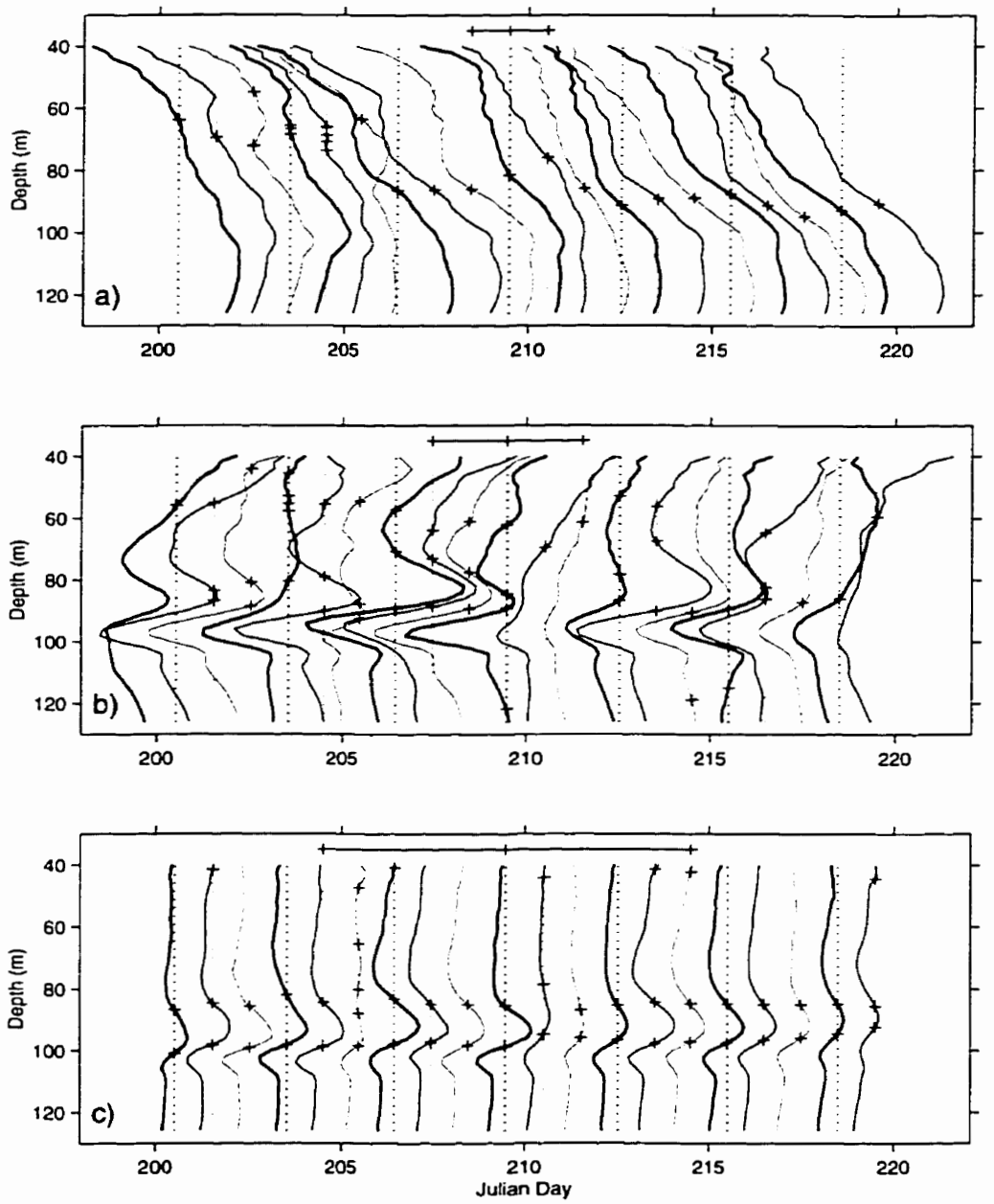

Fig. 7.3. Daily means of residual current in a) along-channel, b) cross-channel, and c) vertical direction. Plus signs indicate zero velocity, and the ± 0.1 m s^{-1} scale is denoted near the top of each plot. The first profile, centred at Julian day 200.5, represents the mean for Julian day 200, July 18.

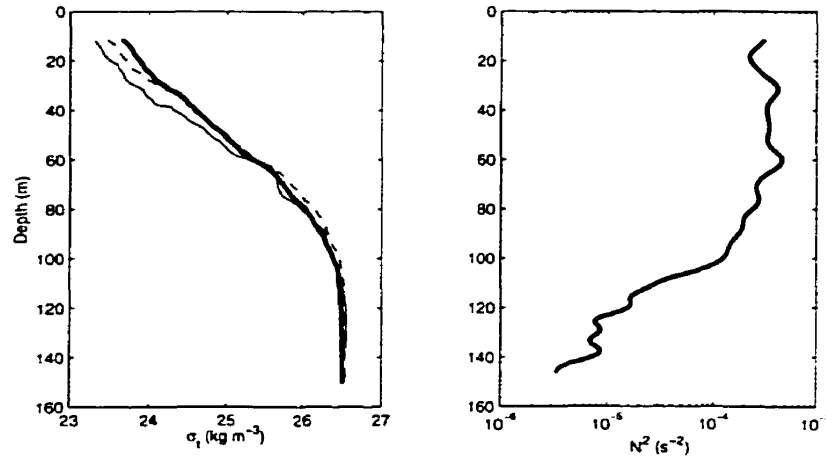

Fig. 7.4. a) Density at CTD station ADCP-S on July 17 (day 199, thin solid, mean of three profiles), July 25 (day 207, thin dash, mean of six profiles), August 6 (day 219, thin dot, mean of three profiles), and overall mean (thick solid), and b) buoyancy frequency of mean profile. Spring tide occurs at Julian days 199 and 213.

and LeBlond (1990). However, this signal is also consistent with an increase in density with time; between Julian day 190 and 220 there is a decrease in the freshwater input as measured by the Fraser River flow, which should result in an increase in salinity in the upper layer, assuming that the amount of lower water entrained into the upper layer does not decrease at the same rate. Unfortunately, while over 60 CTD casts at CTD station ADCP-S were made on July 25 and 26, only three were made on each of July 17 and August 5, and none were made just after the spring tide of July 30 (day 212).

7.2.1 Baroclinic Instability

The criterion for the onset of baroclinic instability based on geometrical arguments was determined to be $W \geq NH/f$. Theoretical arguments for a two-layer flow and for constant stratification yielded the same results, aside from a constant of order unity. In Juan de Fuca Strait, $f = 1.1 \times 10^{-4}$ s^{-1}, the buoyancy frequency is $N \approx 10^{-2}$ s^{-1} (Figure 7.4), and the maximum depth in the central section of the

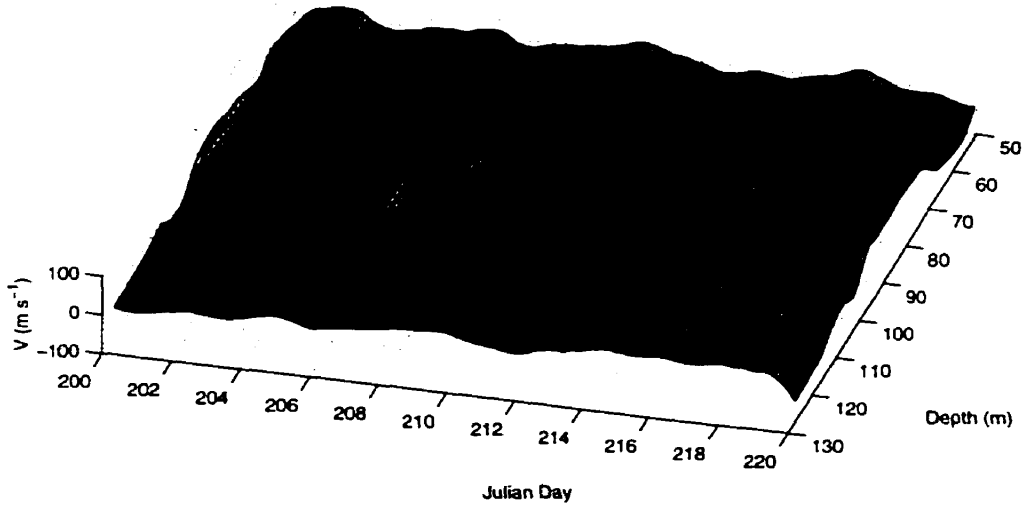

Fig. 7.5. Low frequency oscillations in the cross-channel current. The overall mean at each depth is subtracted from the 48-hour running mean of the residual current.

strait is $H = 200$ m. This suggests that baroclinic instabilities may occur if $W \gtrsim 20$ km, i.e. roughly the width of the strait.

At spring tide, when stratification should be weaker, oscillations in the 48-hour running mean of the residual cross-channel velocity occur at periods of about four days (Figure 7.5). At neap tide, periods are between two and three days. At both spring and neap, currents at depths directly above and below the interface are out of phase. The longer timescales of the oscillations at spring tide may be indicative of a more fully developed baroclinic instability.

7.2.2 Shear Instability

The strong vertical shear in both the along- and cross-channel currents observed in 1973 and 1996 makes it likely that shear instability is important in Juan de Fuca Strait. Transports were generally larger, and stratification, as measured by the density difference between the upper and lower layers, was weaker in 1996 than

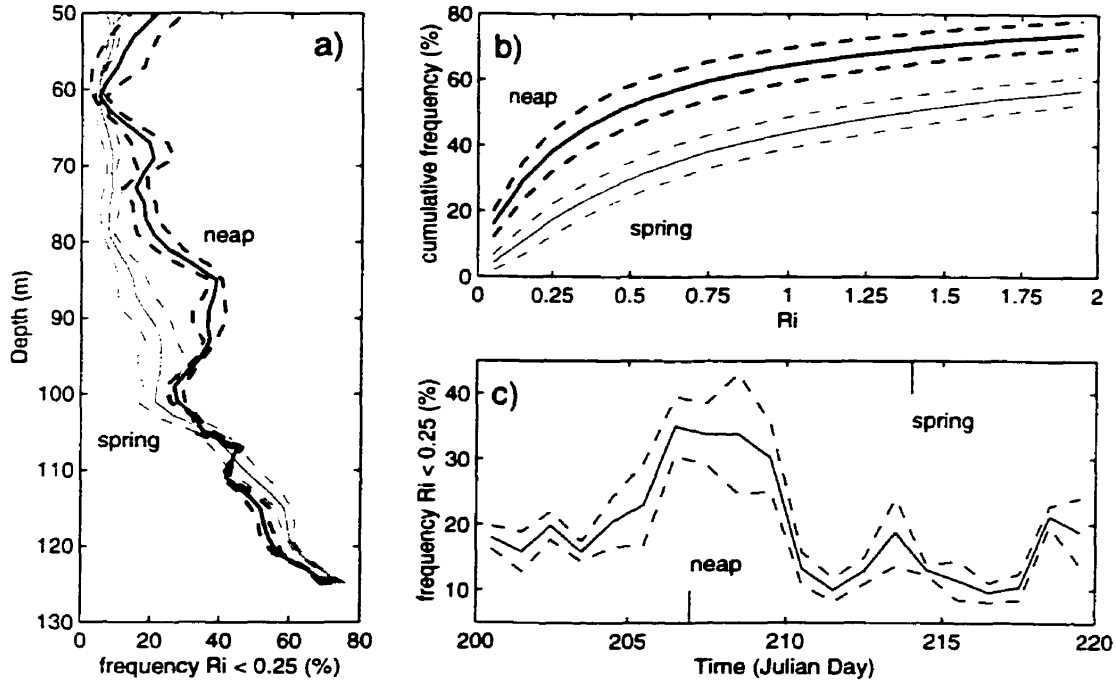

Fig. 7.6. Variation with depth and over the spring-neap cycle of the frequency (%) with which the gradient Richardson number, defined over 2 m, falls below 0.25. In a), the thick and thin lines indicate the period just after neap tide (Julian days 206 to 208) and spring tide (Julian days 213 to 215), respectively. The solid lines are three-day averages and the dashed lines indicate the mean ± the standard deviation of the means for each day. In b), the mean cumulative frequency (%) for the depths between 80 and 90 m over days 206 to 208 and 213 to 215 are denoted by thick and thin lines, respectively. The dashed lines again indicate the mean ± the standard deviation over the three days and 6 depth bins. Panel c) plots the mean daily frequency with which $Ri < 1/4$ over the depth range 80 to 90 m (solid) and the mean ± the standard deviation of the means at each depth (dash).

in 1973, when Ri numbers (calculated over 50 m) were less than unity about 5% of the time.

The Richardson number is calculated with a vertical resolution of two metres using the mean N^2 for the deployment (Figure 7.4) and the shear in the total along-channel current profiles, which are averages of 35 ensembles over 10 seconds. Below 100 m, $Ri < 1/4$ most of the time (panel a, Figure 7.6) which is not surprising given

the strong tidal shear and weak stratification in the bottom well-mixed layer. At mid-depths, maxima in the frequency with which the flow is unstable to shear instability are found between 85 and 90 m, i.e. at the interface between lower inflowing Pacific and outflowing brackish waters, where the 1/4 criterion is reached 25% of the time throughout the deployment, and $Ri < 1$ more than 50% of the time. The flow at mid-depth is more unstable during neap tides, due in large part to the larger shears present; the spring-neap stratification signal is quite weak. The increase in instability above 60 m (panel a, Figure 7.6) is also due to the increase in shear of the along-channel current (Figure 7.1), although whether this is real or an artifact of missing data is unclear.

The spring-neap difference between 80 and 90 m is significant throughout the range of calculated Ri (panel b, Figure 7.6) and does not depend on the choice $Ri = 0.25$. That is, Richardson numbers just after spring tide are significantly larger than after neap tide. The spring-neap cycle in the percentage of critical Richardson numbers between 80 and 90 m depth (panel c, Figure 7.6) also reveals that the current is more unstable just after neap tide. The increase at Julian day 213 (spring tide) is related to bottom shear; the peak decreases when averaging over regions higher in the water column and increases as the bottom is approached.

During spring tide, shear instability appears to follow the tidal cycle (Figure 7.7). On Julian days 213, 214, and 215, mid-depth instability is greatest during peak tidal currents, whereas low Richardson numbers are found at shallower and greater depths during the transition from flood to ebb and from ebb to flood, respectively. At neap tide, however, lower Richardson numbers at mid-depth tend to occur on the transition from the strong ebb to flood tide and during the strong flood itself. The hourly mean currents just above these areas of shear instability are weak, suggesting that critical layer absorption of internal waves may be important dynamically.

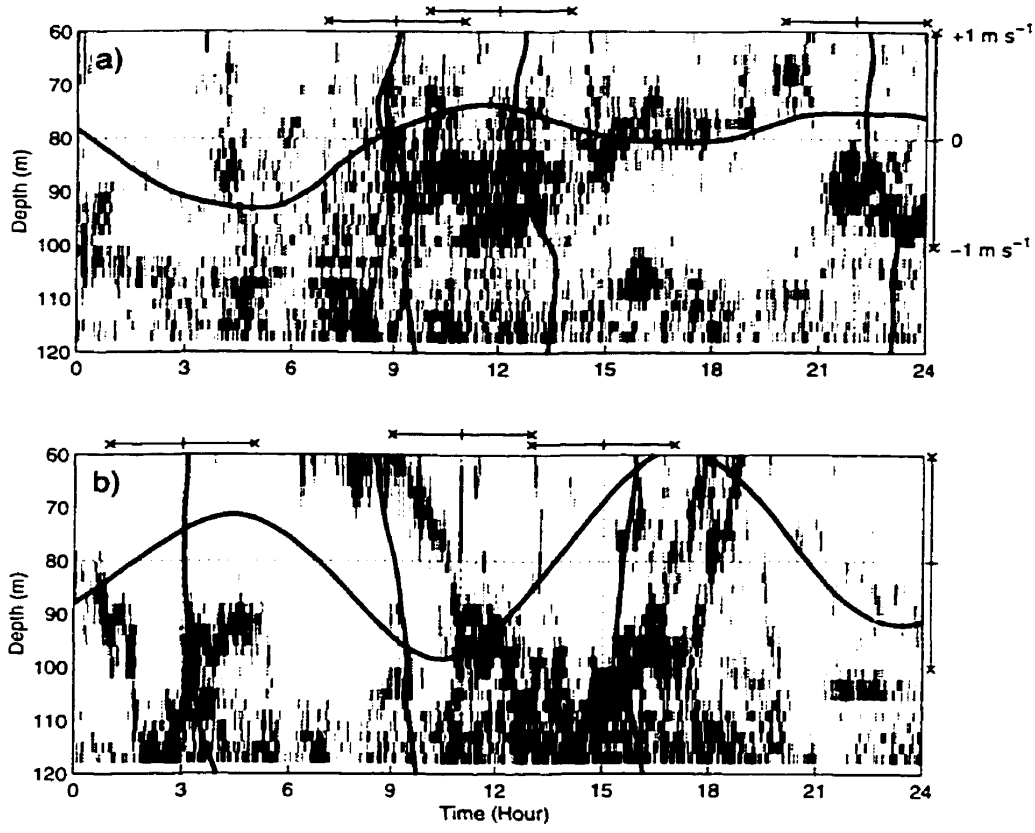

Fig. 7.7. Shear instability on Julian days a) 207 (neap tide) and b) 214 (spring tide). Shaded regions indicate depths and times for which the calculated Richardson number fell below 0.25. The solid horizontal profile is the along-channel tidal velocity at 80 m depth, with the $\pm$ 1 m s^{-1} scale plotted on the right. The vertical profiles at 0900, 1200, and 2200 in a) and at 0300, 1100, and 1500 in b) are the hourly average total (i.e. tidal and residual) along-channel currents with the $\pm$ 1 m s^{-1} scales plotted above.

7.3 Reynolds Stress

The mean momentum equations (2.5) clearly show that convergences or divergences in the correlations of high-frequency current fluctuations affect the mean flow. The difficulty, however, arises in determining what constitutes the fluctuating current as opposed to the mean, especially in geophysical flows where velocities typically occur over all frequencies. Frequencies over which the energy is reduced, or non-existent

in the case of a true spectral gap, provide a convenient cutoff frequency at which to divide the flow. That is, Reynolds stresses based on current fluctuations of frequency greater than that in the middle of the spectral gap should remain constant for changes in the cutoff frequency.

For the present study, the three-dimensional perturbation velocity (u', v', w') is determined by detrending short sections, of between 10 and 80 minute duration, of the total (tidal and residual) ADCP current. The auto- and cross-correlations are calculated by averaging the product of the remaining perturbations over the same time period. It can be shown (e.g. Lu and Lueck 1999, van Haren *et al.* 1994) that the $\overline{u'w'}$ and $\overline{v'w'}$ cross-correlations provide unbiased estimates of the Reynolds stress under the assumption of statistical homogeneity, provided that the (u, v) axes is aligned with the ADCP beam directions. That is, these Reynolds stresses are calculated according to (4.3) with v positive at a direction of 335° relative to true north. While the auto-correlations and $\overline{u'v'}$ are biased, they are included in order to facilitate comparison of the strength of the correlations.

7.3.1 Variation with Averaging Time

The magnitude of the auto-correlations $(\overline{u'u'}, \overline{v'v'}, \overline{w'w'})$ varies somewhat with averaging time at neap tide (Figure 7.8, with similar results for Julian days 206 and 208). Auto-correlations at 10 and 20 minute averaging times are approximately 75% and 85%, respectively, of the values at 80 minutes. The variations in the auto-correlation with averaging time are generally greater at spring tide (Figure 7.9), with values at 10 and 20 minutes only accounting for about 50% and 60% of the 80 minute values. Nevertheless, the general variation of the auto-correlations with depth are constant over the averaging time, particularly for the period after neap tide. Auto-correlations are also much larger after neap than spring and are generally smoother, especially $\overline{u'u'}$.

On the other hand, the variation with averaging time for cross-correlations is quite small for both time periods, with values at 20 minutes about 90% of those at 80

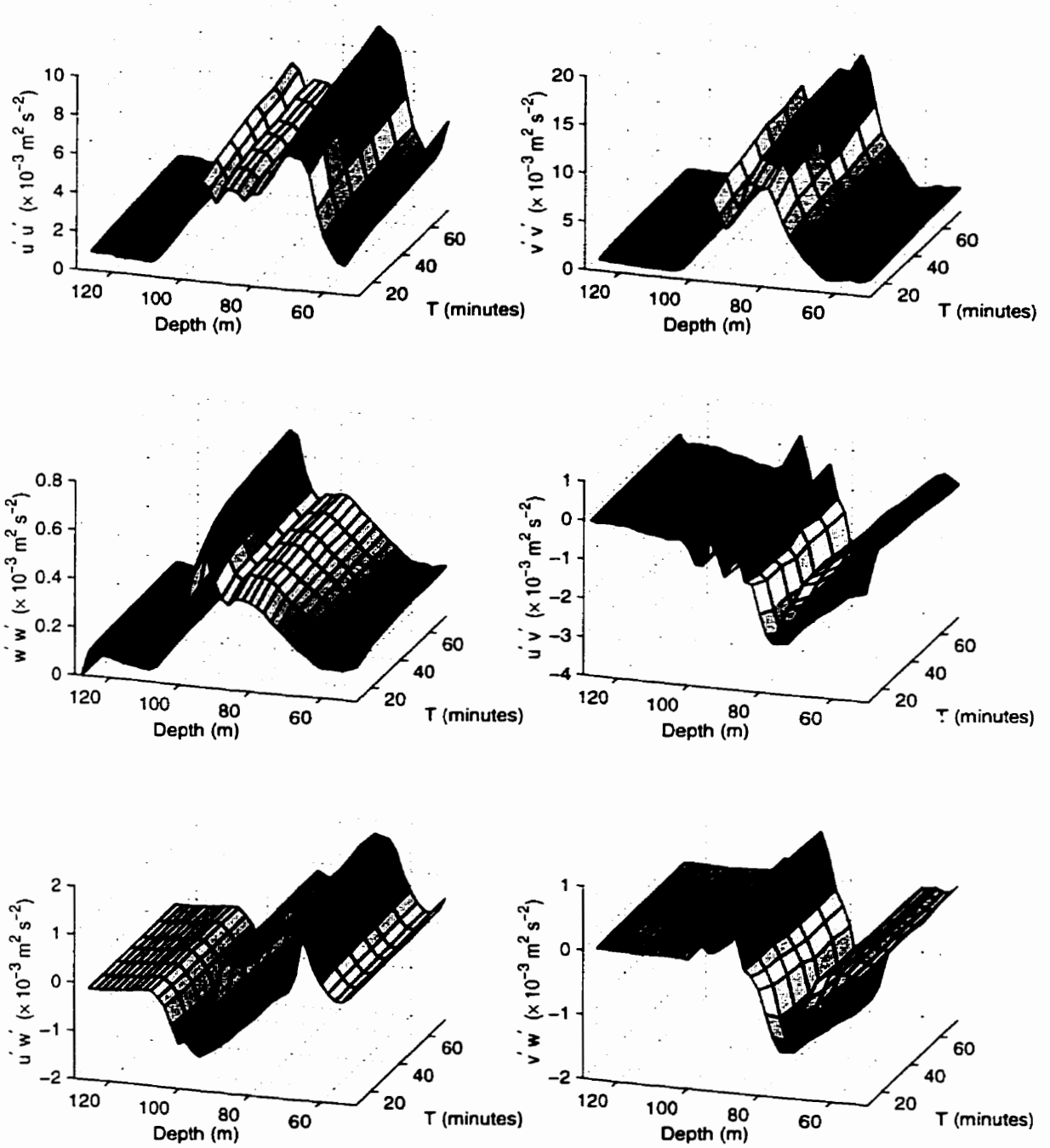

Fig. 7.8. Variation of auto- and cross-correlations of velocity fluctuations with averaging time, T, over the depth range 50 to 130 m for Julian day 207, just after neap tide.

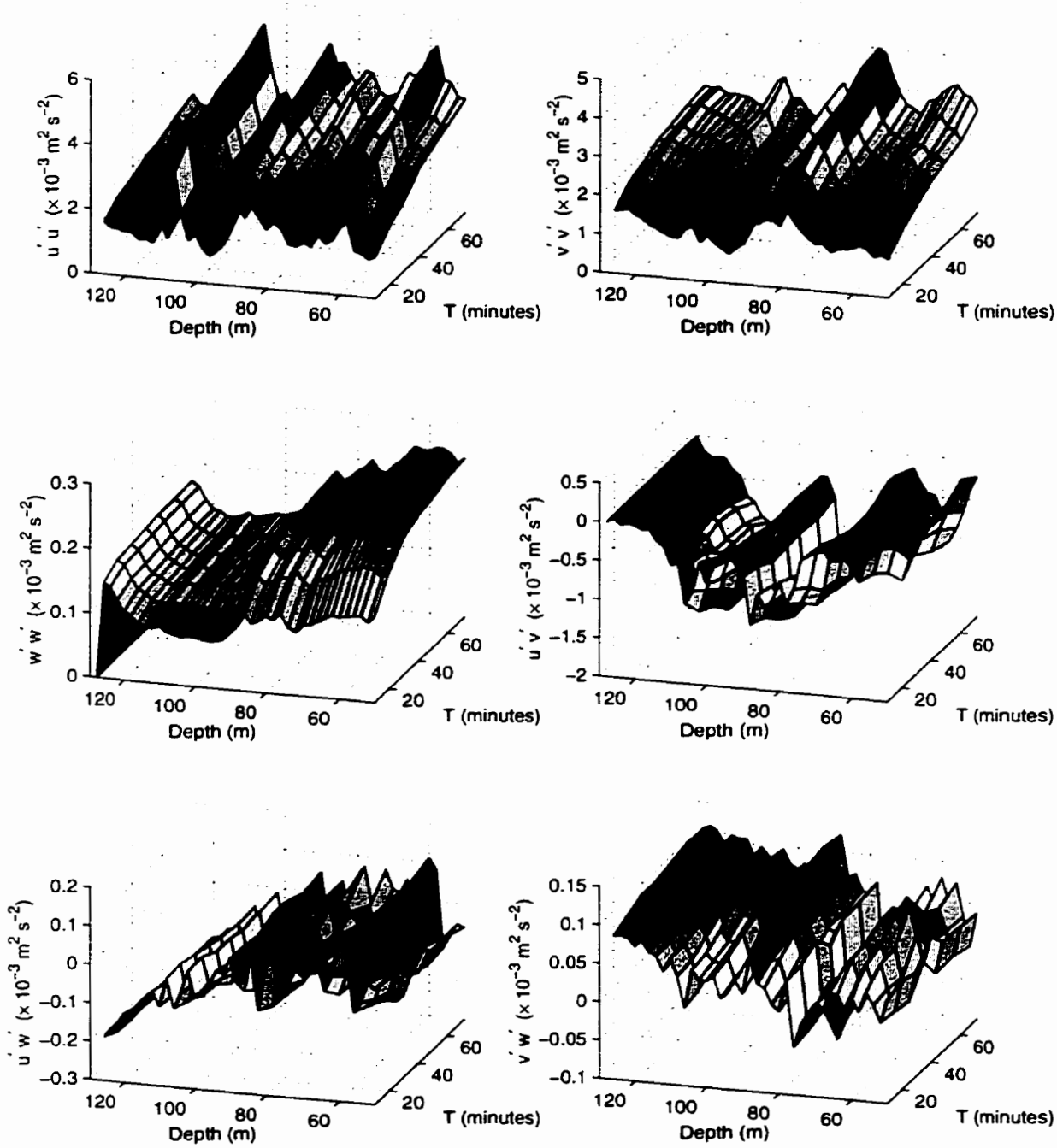

Fig. 7.9. Variation of auto- and cross-correlations of velocity fluctuations with averaging time, T, over the depth range 50 to 130 m for Julian day 214, just after spring tide.

minutes. Values after the neap tide are about an order of magnitude larger than after the spring tide in each case. The variation with depth after spring tide (Figure 7.9) is quite irregular, while that after neap (Figure 7.8) has definite structure. Both of these facts suggest that while the situation after spring tide may be noise, that after neap tide is evidence of large Reynolds stresses.

After neap tide, peaks in $\overline{u'w'}$ at 70 and 95 m depths are about 20% of the corresponding values in $\overline{u'u'}$. Were the $\overline{u'w'}$ signal purely a result of horizontal fluctuations (u' or v') contaminating the vertical w', the error in the measured pitch and roll angle would have to be of the order of 10°. Furthermore, with $\overline{u'u'}$ on day 214 at least a third the peak value at Julian day 207, such large pitch and roll biases would imply $\overline{u'w'} \approx 10^{-3}$ m^2 s^{-2}, much larger than the values seen. The tilt errors required to account for the peaks at 75 m depth in $\overline{v'w'}$ are similar.

In addition, the 95% confidence intervals, determined using the bootstrap technique (von Storch and Zwiers 1998), are small compared to the magnitude of the cross-correlations at neap tide (Figure 7.10). At spring tide, the results are not statistically different from zero. Therefore, the measured cross-correlations at neap should be related to the actual Reynolds stresses by a proportionality constant equal to the density, and the spring-neap cycle is shown to be significant.

The ratio of the error velocity, e, to the vertical velocity, w, increased significantly between 80 and 90 m during neap tide (Figure 5.1), raising concerns about the validity of the measured vertical velocity over these depths. Above 80 m and between 90 and 100 m, however, e/w is much smaller, and it is within these ranges that the values of $\overline{u'w'}$ are large and of opposite sign (Figure 7.10), suggesting that the divergence in the stress, which affects the mean flow, is a real signal.

7.3.2 The Spring-Neap Cycle

To facilitate comparison between the measured Reynolds stresses and the spring-neap cycle in the mean flow, $\overline{u'w'}$ and $\overline{v'w'}$ are rotated into along- and cross-channel directions, with u aligned with the depth-mean orientation of the $M2$ ellipse

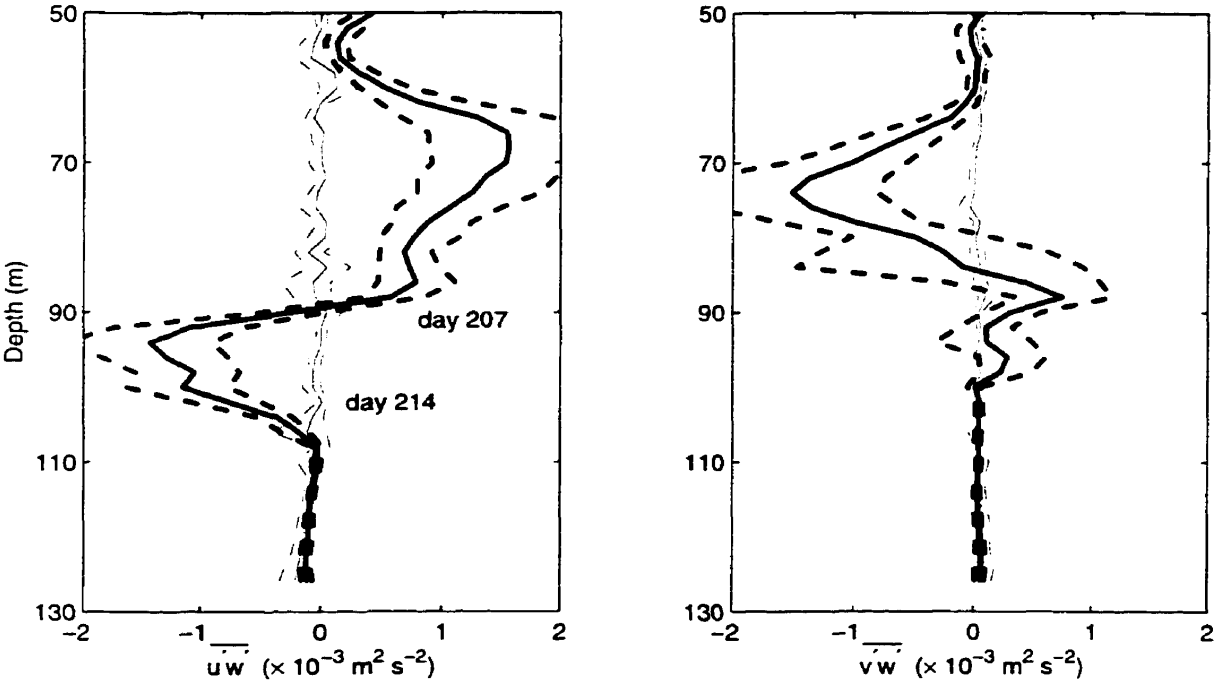

Fig. 7.10. Magnitudes of the daily mean Reynolds stress after neap tide (Julian day 207) and spring tide (Julian day 214), with v positive in the direction of the orientation of ADCP beam 3, 335° from true north. The dashed lines represent the 95% confidence intervals determined from a bootstrap technique.

(10° south of east). The $\overline{u'w'}$ and $\overline{v'w'}$ Reynolds stresses are not significantly different from zero over much of the spring-neap cycle (Figure 7.11), and are largest during the three or four days around neap tide. This is consistent with the reduced Richardson numbers found following neap tide (Figure 7.6), and also with the enhanced estuarine exchange at this time. Although the salinity at Race Rocks is considerably recovered by Julian day 213 from the anomalously low values over much of the previous month (Figure 4.4), indicating a return to a more common spring-neap cycle in the estuarine exchange, there is some indication that Reynolds stresses during the neap centred at Julian day 221 are again significant. Thus, while it may be that the measured stresses are enhanced compared to the regular neap values, the data suggests that a regular spring-neap cycle in the mixing in Juan de Fuca Strait exists.

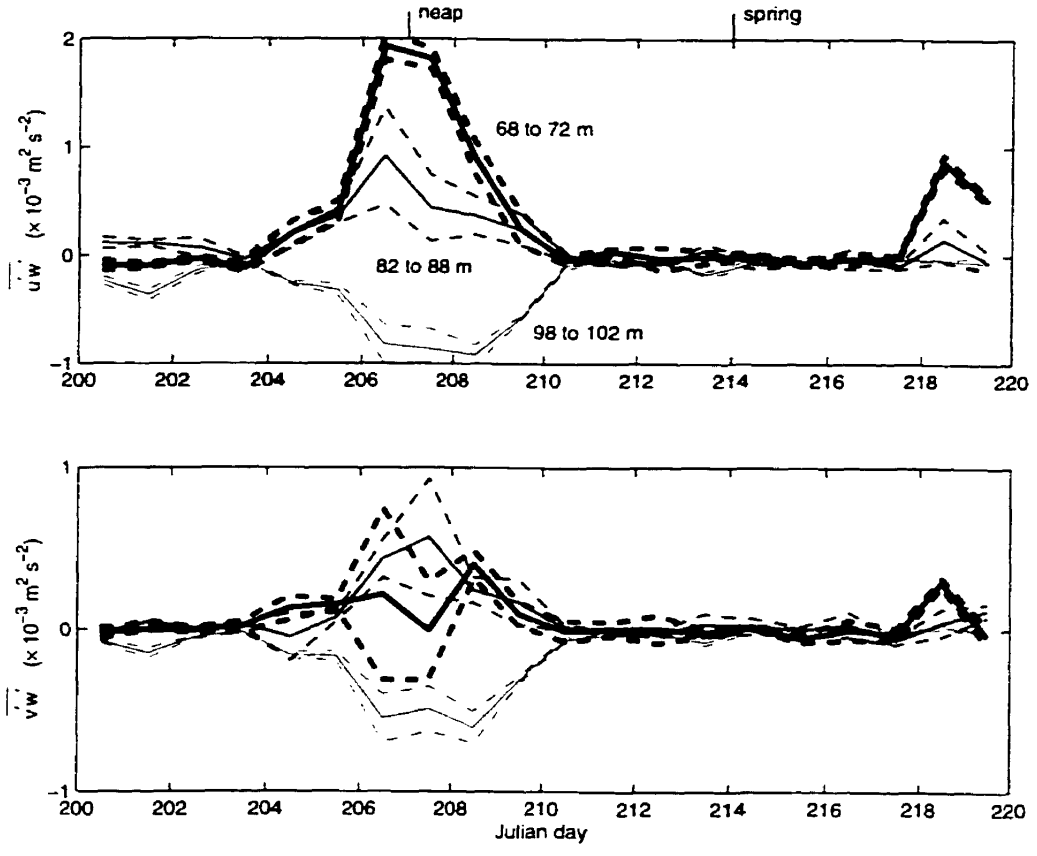

Fig. 7.11. Variation of $\overline{u'w'}$ and $\overline{v'w'}$ Reynolds stress throughout the spring-neap cycle. In each case, the solid lines represent the daily averages over the depth ranges shown and the dashed lines indicate the standard deviation over the depth range. The (u, v) axes are rotated such that u is positive up-channel.

This was found to be the case in the results of Masson and Cummins' (2000) numerical model investigating the effect of a fortnightly modulation of the tidally-induced mixing over Victoria sill on the circulation and dynamics within Juan de Fuca Strait itself. That is, interfacial mixing in the central section of the strait was found to be larger during neap tide than at spring tide, enhancing the vertical exchange of momentum. As a result, the spring-neap cycle in the estuarine exchange was reduced in the downstream direction, a "negative feedback" (Patrick Cummins, personal communication, 2000) which largely confined the salinity and current variations to the eastern portion of the strait.

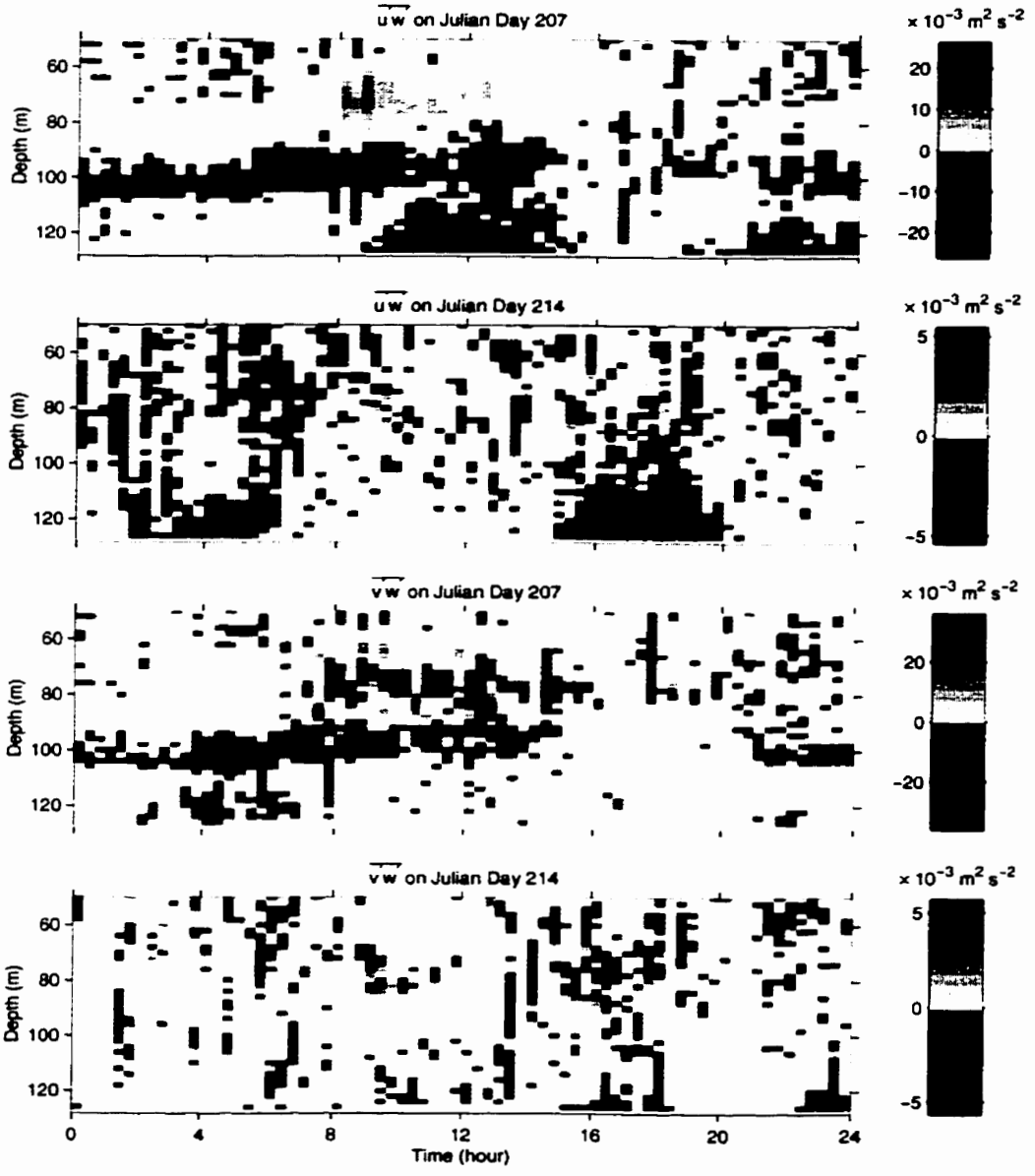

Fig. 7.12. Reynolds stresses at neap (Julian day 207) and spring (Julian day 214) tide. Stresses of magnitude less than 10^{-4} m^2 s^{-2} are not shown.

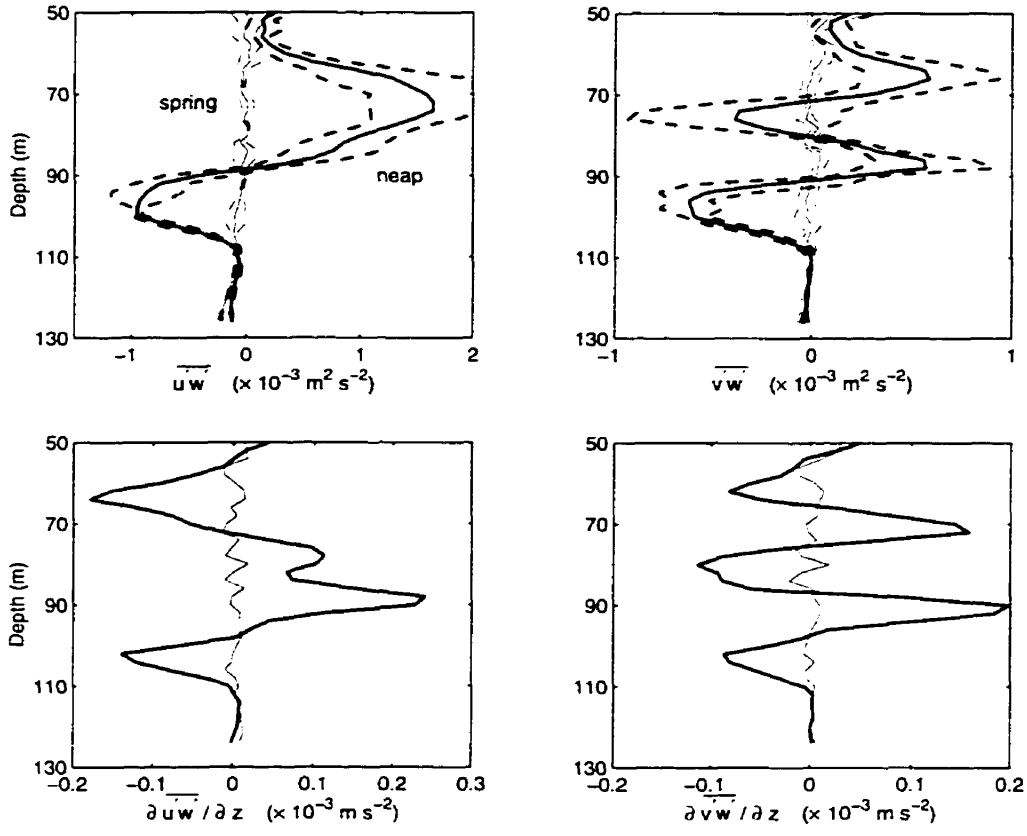

Fig. 7.13. Mean vertical Reynolds stress and vertical derivative over three days at neap (Julian day 206 to 208, thick lines) and spring tide (Julian day 213 to 215, thin lines). The dashed lines indicate the standard deviation over the three days.

Strong neap $\overline{u'w'}$ stresses occur between strong ebb and the following flood (Figure 7.12). This is true both below 85 m, where the stresses are predominantly negative, and above 85 m, where the stresses are positive. The stresses occur at the same depths and times as the low Richardson numbers (Figure 7.7). There is a suggestion that the $\overline{u'w'}$ stress at spring tide also occurs when $Ri < 1/4$, but the magnitude of the stress is much weaker and the signal is not apparent.

With the exception of the bottom boundary layer, the mean Reynolds stress during spring tide is not significantly different from zero throughout the water column (Figure 7.13). The mean bottom stress acting on the water can be parameterised as $\tau/\rho = -4/\pi C_D U_T u$, where U_T is the magnitude of the tidal current and u is the mean

near-bottom velocity. For $C_D = 3 \times 10^{-3}$, $U_T \approx 1$ m s^{-1} and 0.5 m s^{-1} at spring and neap tide, respectively, and $u \approx 0.1$ m s^{-1}, the Reynolds stress should be of the order -4×10^{-4} m^{2}s^{-2} at spring tide. The measured value of the Reynolds stress near the bottom is in rough agreement, with $\overline{u'w'} \approx -2 \times 10^{-4}$ m^{2}s^{-2}, and about half that at neap tide (Figure 7.13).

Above the bottom boundary layer, the Reynolds stress during neap tide is large throughout most of the water column. There is a strong divergence of $\overline{u'w'}$ within a 30 m band centred at the depth of the zero mean along-channel current, with convergences above and below. During neap tide, the depth averages of both $\overline{u'w'}$ and $\overline{v'w'}$ between 50 m and the bottom, $(6 \pm 8) \times 10^{-5}$ m^2 s^{-2} and $(-5 \pm 6) \times 10^{-5}$ m^2 s^{-2}, respectively, are not statistically different from zero, indicating that the measured stresses are consistent with a redistribution of momentum over the water column.

7.3.3 The Vertical Eddy Viscosity

The along-channel estuarine circulation is enhanced at neap tide, with integrated inflows below 85 m depth of approximately 6 m^2 s^{-1}, compared to about 4 m^2 s^{-1} during spring tide (Figure 7.14). The increase in the transverse flows is even more dramatic, with velocities at 95 m increasing four-fold, to about 0.16 m s^{-1}. These currents are not significantly affected by the choice of cross-channel direction: rotating the axes orientation clockwise by a further 20° reduces the neap magnitude at 95 m depth to only 0.12 m s^{-1}. The depth of the maximum transverse current increases from 98 m at spring to about 94 m during neap tide, closer to the 90 m peak in the vertical derivative of the measured Reynolds stress (Figure 7.13).

The enhanced estuarine exchange and transverse flows at neap tide lead to larger shears in both horizontal components (Figure 7.14), particularly between 80 and 90 m depth. As a result, the gradient Richardson number is considerably smaller over these depths at neap tide (Figure 7.6). The vertical eddy viscosity, parameterised as $A_v \equiv -\overline{u'w'}/U_z$, with U_z the vertical shear in the mean along-channel velocity, is positive and increases with height above the bottom in the lowest 15 m, and is larger

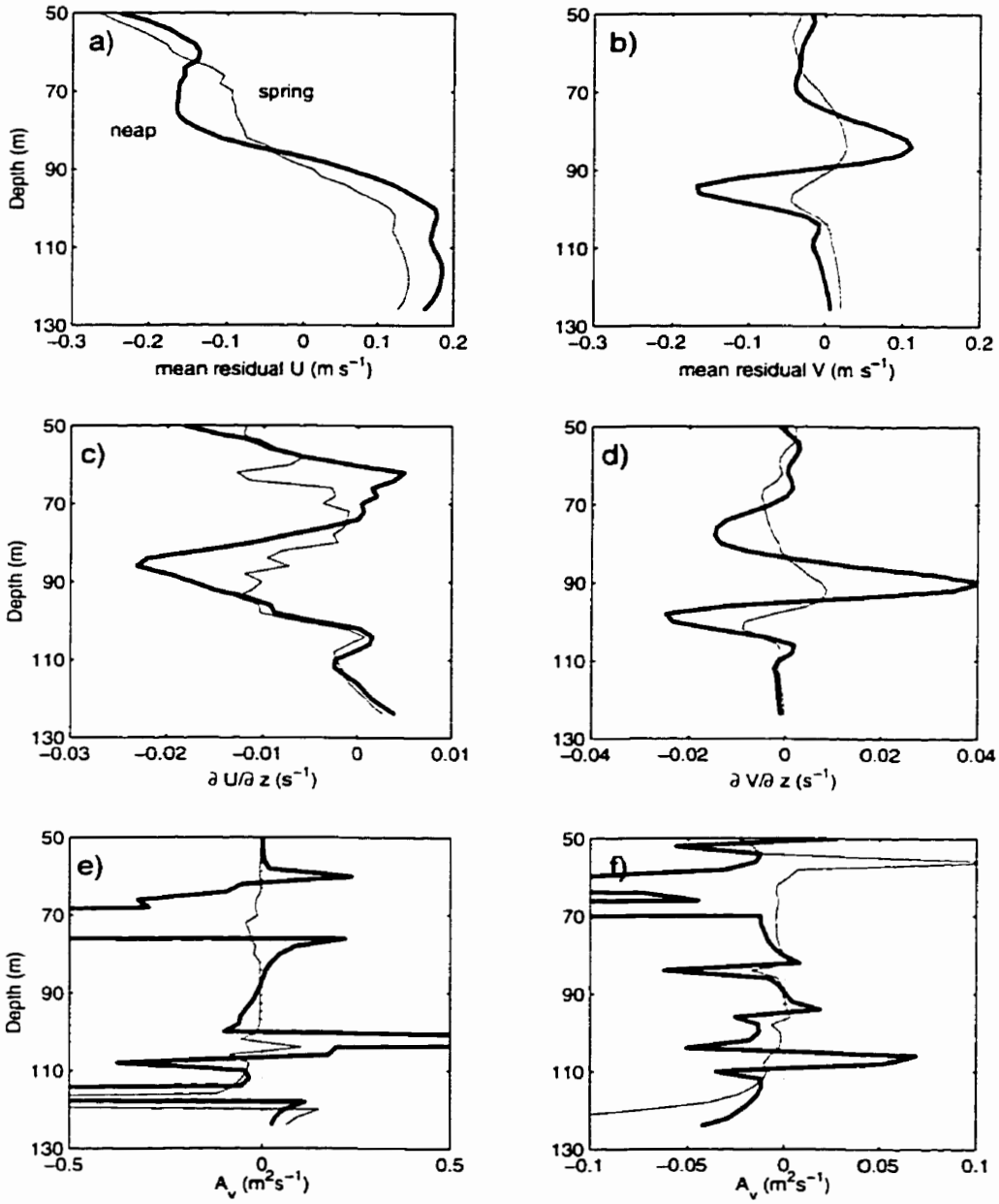

Fig. 7.14. Mean residual a) along-channel and b) cross-channel current with c) and d) associated shears. The vertical eddy viscosities, parameterised as (2.6) are plotted in e) and f). Thick lines are the three day averages at neap tide (Julian day 206 to 208) and thin lines during spring tide (Julian day 213 to 215).

at spring tide than at neap tide (Figure 7.14). This is the expected result for wall-bounded flow, where eddy sizes are restricted close to the solid boundary.

Above 80 m and between 100 m and 120 m, the shear is weak, magnifying uncertainties in the measured Reynolds stress to the point where the vertical eddy viscosity parameter, A_v, is not meaningful. In the interfacial region (between 80 and 100 m), however, A_v varies with depth, and is negative below the interface. This indicates that the Reynolds stress is transporting momentum up-gradient (possibly by internal waves generated at the bottom and breaking at mid-depths), suggesting that the fluctuations may be driving the mean current. At neap tide, the Richardson number was lowest at mid-depth, particularly after the ebb tide and on the subsequent transition to flood (Figure 7.7), i.e. when the along-channel currents at 80 m were nearly zero. The $\overline{u'w'}$ stress divergence was also largest at 80 m depth during this time (Figure 7.12). This suggests that a critical layer exists near the interface, where internal waves generated as the tide flows over topography within the strait break.

7.3.4 Effect on the Mean Flow

The stress divergences during spring tide are relatively small, and have little effect on the mean flow compared to the forcings at neap tide. The vertical derivatives of these Reynolds stresses appear explicitly (i.e. are not parameterisations) in the momentum equations, which can be written as

$$\begin{aligned} u_t + (\overline{u'w'})_z - fv_a &= 0 \\ v_t + (\overline{v'w'})_z + fu_a &= 0 \end{aligned} \tag{7.3}$$

where (u_a, v_a) are the ageostrophic horizontal velocities. The divergence in $\overline{u'w'}$ for example, can directly alter v_a or lead to accelerations in u. With the measured hydrography at the ADCP site very similar between spring and neap tide (Figure 7.4), the geostrophic velocities should be relatively unchanged.

The depth average of the stress divergence over the bands centred at 100 and 85 m are of magnitude $\approx 0.5 \times 10^{-4}$ m s^{-2}, implying $(\overline{u'w'})_z/f \approx 0.5$ and -0.5 m s^{-1}, respectively. Although these are of the same sign as the change in the cross-channel current from spring to neap (Figure 7.14), they are too large by about a factor of three. The peak in $(\overline{u'w'})_z$ at 65 m is not associated with a significant spring-neap difference in the cross-channel flow. Above 80 m depth, $-(\overline{v'w'})_z/f$ is consistent with changes in the along-channel flow, within a factor of two. The large narrow band with $(\overline{v'w'})_z < 0$ centred at 90 m depth does not appear to affect the along-channel current. The average of $(\overline{v'w'})_z$ between 75 and 100 m $\approx 8 \times 10^{-6}$ m s^{-2}, however, which is consistent with the changes in u at 100 m of 0.08 m s^{-1}.

The $(\overline{u'w'})_z$ profile is also qualitatively similar to spring-neap differences in u, except for the region below 110 m, suggesting that some part of the measured Reynolds stress divergence may be accelerating the flow. The agreement in shape between $(\overline{v'w'})_z$ and v above 100 m depth is also reasonable. However, the difference of -0.1 m s^{-1} in u seen at 80 m depth could be driven by the measured Reynolds stress divergence of about 5×10^{-5} m s^{-2} in only 2000 s, or about 30 minutes, whereas the stress divergences act on the mean flow for a period of about three days.

Preliminary analysis of 1998 ADCP data from a location a few kilometres away reveals that both the mean cross-channel currents and estuarine exchange were considerably smaller. In 1998, the current structure was similar to that observed in 1996 during spring tide, suggesting that the neap tide results may be due to very localised processes. That is, if the 1996 current structure elsewhere in the strait were similar throughout the spring-neap cycle to that found at the ADCP site at spring tide, as in 1998, the currents would only be driven by the strong neap Reynolds stress divergences as the along-channel current advects water past the ADCP site. For a root-mean-square tidal velocity of $u_{rms} = 0.5$ m s^{-1}, a simple estimate of the along-channel length scale of the forcing field required to drive the currents observed above the 1996 ADCP is 10^3 m, roughly the length scale of the local topographic feature underneath the ADCP unit. After passing over the local bathymetry the forcing

would end and friction would reduce the shears and currents to values more typically found elsewhere in the strait.

However, numerical models (Masson and Cummins 2000) suggest that the spring-neap cycle in the estuarine exchange flow is more pervasive, although the magnitude of the modulation was found to be about 20% of the mean, considerably less than that measured (Figure 7.14). This implies that the variability measured is only partly due to the regular spring-neap cycle. The anomalously low surface salinities at Race Rocks during the deployment period (Figure 4.4), which were not found during the 1998 deployment, are consistent with unusually large exchange flow resulting from northwesterly winds in the Strait of Georgia during neap tide (Griffin and LeBlond 1990).

The mid-depth Reynolds stresses measured during the neap tide which occured during the deployment are sufficiently large to considerably alter the current structure within Juan de Fuca Strait. Unfortunately, while the surface salinity recovered toward the end of the deployment, currents and Reynolds stresses were measured over only the single neap tide, making it difficult to draw firm conclusions regarding either the temporal or spatial variability of the observed spring-neap cycle in the turbulent mixing.

Chapter 8

Conclusions

The along-channel circulation in partially-mixed estuaries is fairly well understood. Salinity in the brackish upper outflow increases in the downstream direction due to entrainment and diffusive fluxes, while saltier oceanic water flows into the estuary at depth. In Juan de Fuca Strait, this estuarine flow is highly seasonal, as evidenced by historical current meter and hydrographic data. Maximal exchange flows, for example, occur after the summer freshet.

Historical current meter data from a number of deployments were used to demonstrate that the upper to lower layer differences in along-channel currents were consistent with the thermal wind equation over a large range of stratifications, implying significant seasonal and inter-annual variability in the cross-channel isopycnal slopes. The cross-channel difference in the depth of the mean along-channel flow was found to be consistent with that of the isopycnals.

Monthly average sea level and atmospheric pressure data reveal that surface pressure gradients inside Juan de Fuca Strait reach about 5×10^{-2} Pa m^{-1} seaward in August. However, upper layer currents are fairly constant in the seaward direction, implying that friction between the two layers partly offsets the pressure term. A momentum balance suggests that the vertical eddy viscosity $A_v \approx 0.02$ m^{2}s^{-1} at interfacial depths in May and larger values may be more appropriate in summer.

A breakdown in the geostrophic balance, a result of friction acting on shear, leads to transverse currents. Historical current meter data reveal strong cross-channel flows of up to 0.06 m s^{-1} at mid-depths in Juan de Fuca, although vertical resolutions have been insufficient to properly resolve them. Laboratory experiments (Johnson and Ohlsen 1994) have demonstrated that strong transverse currents exist at the interface of a two-layer rotating flow, allowing water masses formed at the sidewalls to spread

into the interior, limiting the along-channel exchange, and aiding in the dispersal of tracers. The structure of cross-channel flows in real estuaries is considerably more complex than in the laboratory, however, owing to continuous stratification and the presence of tides and internal waves, and they remain poorly understood.

Turbulence, which elevates mixing rates and enhances stresses which can affect the mean flow, is also associated with strong friction. Traditional current meters measure only the horizontal component of the velocity and record only after significant averaging. Acoustic Doppler Current Profilers, on the other hand, sample the three-dimensional velocity much more rapidly, enabling the fluctuating components to be measured. This provides an additional tool in the study of the effect of Reynolds stresses on the dynamics of geophysical flows.

A better understanding of the cross-channel flows, turbulence, and mixing within Juan de Fuca Strait was the motivation for the observational programme of 1996. Specifically, I was interested in adequately resolving the interfacial region, particularly the transverse currents, and in examining the forcing terms which drive the dynamics in a partially-mixed estuary. An additional aim was to measure Reynolds stresses in a stratified fluid to complement the dynamical study.

Timed to coincide with the expected maximal estuarine flow due to the summer freshet, a bottom-mounted ADCP was deployed in the central section of Juan de Fuca Strait in July for 21 days. Currents were sampled every 30 seconds with two-metre vertical resolution over a large portion of the water column, capturing the mid-depth region containing the interface between the brackish surface layer and the return flow beneath. Conductivity-Temperature-Depth (CTD) profiles were obtained over the course of the deployment to determine the hydrography.

a) Vertical Velocities

Vertical currents are the most difficult velocity component to measure, mainly because they are generally small in magnitude. Difficulties include the risk of contamination by horizontal velocities through errors in the measured ADCP tilt angles, spatial inhomogeneity over the width of the beam separation, and contamination due

to the active migration of zooplankton. A minimisation of the energy contained in w for pitch and roll corrections revealed that there is no obvious bias in either tilt angle, and the difference in vertical velocity estimates from orthogonal beam pairs was small compared to the mean vertical velocity. At times and depths outside zooplankton migration routes, internal wave induced undulations in bands of anomalously large backscatter intensity were used as independent confirmation of the reliability of the vertical velocity estimate. Slopes of vertical velocity versus backscatter intensity, as well as composite anomalies of w and the intensity suggest that the diurnal zooplankton migration did not have a significant bias on the measured vertical velocity, even though the migrating zooplankton clearly show up in the backscatter intensity data. This is in contrast to Plueddemann and Pinkel (1989), who found that the vertical velocities measured with a 67 kHz ADCP in an oceanic environment were consistent with the backscatter signal. The differences, which may be the result of the frequency used or of the populations of zooplankton, warrant further examination.

b) Tides

The effect of bottom friction in reducing the magnitude of the near bottom currents was clearly seen in the tidal constituents. This motivated a log-layer analysis of the total along-channel current, and the results suggest that the drag coefficient was only slightly larger on flood tide than on ebb, with $C_D = 2.9 \times 10^{-3}$ and $C_D = 2.8 \times 10^{-3}$, respectively. For rectilinear currents, one would expect the bottom roughness parameter to be independent of the freestream velocity. The data showed very small correlation ($r = -0.023$) between z_o and U_{11} for flood tide, and somewhat larger correlation ($r = 0.21$) for ebb.

The flip in rotation sense of the $M2$ current vector just above the bottom was demonstrated to be the result of different boundary layer thicknesses for the clockwise and anticlockwise rotating components. The momentum balance analysis proposed by Soulsby (1983) predicted the shear of the magnitudes for the two components fairly well in the bottom 15 m. In contrast, agreement between the theoretical and measured phases was poor. A fuller numerical model, i.e. involving a time-varying

eddy viscosity, should improve the prediction, but without modelling the effects of stratification cannot be expected to do so above the bottom well-mixed layer. The presence of internal tides, as evidenced by the baroclinicity of the tidal magnitudes above the bottom boundary layer, is a further complication, and a proper analysis would necessarily include the topography of Juan de Fuca Strait, and possibly the shelf break as well.

Energy spectra showing that considerable energy is present at near-tidal frequencies also suggests that the tides within Juan de Fuca Strait contain internal modes. The vertical structure of these modes can be significantly altered in the presence of a mean current. Furthermore, incoming and outgoing waves are affected differently by the estuarine flow within the channel. Thus, without horizontal resolution of the tidal currents, a decomposition of the total tide into its barotropic and baroclinic components is a difficult task.

The vertical structure of the internal modes in a non-rotating fluid is given by the Taylor-Goldstein equation. The Rossby radii for the barotropic tides and the first baroclinic tide at diurnal frequencies are much larger than the width of the strait, and the tides are rectilinear. For higher modes, however, cross-channel tidal components are not constrained to be zero, and the Taylor-Goldstein equation may not be appropriate. The modal fits to the measured tidal currents did not allow modes higher than the first baroclinic to be identified though, so this was not an issue in the present study.

A modal fit to the observed $M2$ tide suggests that the barotropic tide has a magnitude of about 0.47 m s^{-1}. The first baroclinic mode has maximum associated currents of between 0.05 and 0.10 m s^{-1}. Horizontal resolution of the tidal structure within Juan de Fuca Strait is required to properly determine this. Unfortunately, historical data sets which contain some degree of horizontal resolution suffer from a lack of vertical resolution.

c) The Mean Flow

The vertical structure of the currents at mid-depth was resolved, revealing large cross-channel currents and strong shears in the interfacial region. The mean along-channel flow is typical of estuarine circulation, with outflow in the upper layer, and return flow beneath. The measured currents are generally larger at all depths than geostrophic currents based on the measured hydrography, suggesting that the dynamics affecting the flow may be sufficiently localised that they do not affect the hydrography at the nearest CTD stations. Currents are particularly strong at mid-depth (i.e. near the interface), with means reaching -0.07 m s^{-1}, and are robust to small rotations of the (x, y) axes.

The three-dimensional mean residual flow in Juan de Fuca Strait agrees in a qualitative sense with results from a laboratory experiment of two-layer rotating exchange flow (Johnson and Ohlsen 1994), although the spring-neap and inter-annual variations measured suggest that the dynamical processes may not be similar. Both the along- and cross-channel mean currents were significantly larger during neap tide than at spring tide. The fortnightly modulation of the estuarine exchange flow can be understood in terms of elevated mixing levels in the Gulf Islands upstream of Juan de Fuca Strait during spring tides, which enhances the vertical exchange of momentum, reducing the estuarine exchange. Occasionally, northwesterly winds in the Strait of Georgia during neap tides result in an additional increase in the exchange flow, and surface salinity data from Race Rocks suggests that such an event occured over the time of the ADCP deployment.

d) Interfacial Mixing

Direct measurements of the Reynolds stress were made in a stratified environment and temporal variability was clearly seen, both on semidiurnal and fortnightly timescales. The spring-neap cycle in the turbulent mixing matched that of the shear in that elevated mixing levels were associated with lower gradient Richardson numbers. The decrease in the gradient Richardson number during neap tide implies that the exchange flow is more unstable to shear instability, and the prevalence of low

Richardson numbers during the transition from ebb to flood at interfacial depths suggests that critical layer absorption of internal waves may be dynamically important.

The magnitudes of the measured Reynolds stresses were qualitatively consistent with the observed spring-neap variations in the mean along and cross-channel currents. While the fortnightly modulation in the estuarine exchange arises upstream in the narrow and shallow constrictions between the Gulf and San Juan Islands, the additional mixing inside Juan de Fuca Strait during neap tide enhances the vertical transfer of momentum, and likely acts as a brake on the spring-neap cycle of the along-channel flow.

d) Future Work

Efforts to further study the spring-neap variation in turbulence and the associated effects on the mean currents would benefit from a more thorough analysis of the hydrographic and current structure within Juan de Fuca Strait. Most of the CTD profiles near the ADCP site, including the only time series, were taken over a single two-day period, at neap tide. In addition to increased measurement of the spring-neap hydrographic cycle, higher resolution in the horizontal direction is needed. The spacing between CTD stations near the ADCP site was too large to measure the effect of any localised dynamic processes which were occuring. A series of hydrographic moorings would accomplish both of these objectives, and the synoptic coverage would also allow internal waves to be measured.

There is also some uncertainty as to whether the spatial variability in the observed current structure and Reynolds stresses is part of the regular spring-neap cycle in Juan de Fuca Strait or if it was a result of the freshwater event which occured in late July. Measurements over several spring-neap cycles are required to more fully understand the degree to which mixing within the strait is modulated by the fortnightly tidal cycle.

References

Batchelor, G., 1967: *An introduction to fluid dynamics*, Cambridge University Press, London, 615 pp.

Blumen, W., 1972: Geostrophic adjustment, *Rev. Geophys. Space Phys.*, **10**, 485-528.

Bowden, K., L. Fairbairn, and P. Hughes, 1959: The distribution of shearing stresses in a tidal current, *Geophys. J. R. Astron. Soc.*, **2**, 288-305.

Bowden, K., and P. Hamilton, 1975: Some experiments with a numerical model of circulation and mixing in a tidal estuary, *Est. Mar. Coastal Sci.*, **3**, 281-301.

Bradshaw, P., and J. Woods, 1978: Geophysical turbulence and buoyant flows, in *Turbulence*, vol. 12 of *Topics in applied physics*, edited by P. Bradshaw, pp. 171-192, Springer-Verlag, New York.

Cameron, W., and D. Pritchard, 1963: Estuaries, in *The Sea, ideas and observations on progress in the study of the seas*, vol. 2, edited by M. Hill, pp. 306-324, Interscience Publishers, New York.

Clay, C., and H. Medwin, 1977: *Acoustical oceanography: principles and applications*, Interscience Publishers, New York, 544 pp.

Crean, P., and A. Ages, 1971: *Oceanographic records from twelve cruises in the Strait of Georgia and Juan de Fuca Strait. 1968*, vol. I-V, [Ottawa] Dept. of Energy, Mines and Resources, Marine Sciences Branch.

Csanady, G., 1972: Secondary circulation near an upwelled density interface, in *Canadian Conference on Oceanography*, p. 41.

Csanady, G., 1976: Mean circulation in shallow seas, *J. Geophys. Res.*, **81**, 5389-5399.

DaSilva, A., C. Young, and S. Levitus, 1995: *Atlas of Surface Marine Data. 1994*, vol. 1 of *Algorithms and Procedures, NOAA Atlas, NESDIS, 6*, Natl. Oceanogr. and Data Cent., Silver Springs, Md., 83 pp.

Davies, A., 1986: A model of oscillatory rough turbulent boundary layer flow, *Est. Coast. and Shelf Sci.*, **23**, 353-374.

Defant, A., 1961: *Physical oceanography*, vol. II, Pergamon Press, New York, 598 pp.

Dyer, K., 1973: *Estuaries: a physical introduction*, Wiley-Interscience, New York, 140 pp.

Eady, E., 1949: Long waves and cyclone waves, *Tellus*, **1**, 33-52.

Ellison, T., and J. Turner, 1960: Mixing of dense fluid in a turbulent pipe flow, *J. Fluid Mech.*, **8**, 514-544.

Fang, G., and T. Ichiye, 1983: On the vertical structure of tidal currents in a homogenous sea, *Geophys. J. R. Astron. Soc.*, **73**, 65-82.

Fischer, H., E. List, R. Koh, J. Imberger, and N. Brooks, 1979: *Mixing in inland and coastal waters*, Academic Press, San Diego, Calif., 483 pp.

Fissel, D., 1976: Pressure differences as a measure of currents in Juan de Fuca Strait, *Pac. Mar. Sci. Rep.*, **76-17**.

Fjeldstad, J., 1935: Interne welle, *Geofys. Publ.*, **10**.

Foreman, M., 1976: Manual for tidal currents analysis and prediction, *Pac. Mar. Sci. Rep.*, **78-6**, 57 pp.

Forrester, W., 1974: Internal tides in St. Lawrence Estuary, *J. Marine Res.*, **33**, 55-66.

Francois, R., and G. Garrison, 1982: Sound absorbtion based on ocean measurements. Part II: boric acid contribution and equation for total absorption, *J. Acoustic Soc. Am.*, **72**, 1879-1890.

Gill, A., 1982: *Atmosphere-ocean dynamics*, Academic Press, New York, 662 pp.

Godin, G., 1972: *The analysis of tides*, University of Toronto press, Toronto, 264 pp.

Griffin, D., and P. LeBlond, 1990: Estuary/ocean exchange controlled by spring-neap tidal mixing, *Est. Coast. and Shelf Sci.*, **30**, 275-297.

Hansen, D., and M. Rattray, 1965: Gravitational circulation in estuaries, *J. Marine Res.*, **23**, 104-122.

Hansen, D., and M. Rattray, 1966: New dimensions in estuary classification, *Limnol. Oceanog.*, **11**, 319-326.

Herlinveaux, R., 1954: Tidal currents in Juan de Fuca Strait, *J. Fish. Res. Bd., Canada*, **1(6)**, 799-815.

Hickey, B., R. Thomson, H. Yih, and P. LeBlond, 1991: Velocity and temperature fluctuations in a buoyancy-driven current off Vancouver Island, *J. Geophys. Res.*, **36**, 10507-10538.

Holbrook, J., and D. Halpern, 1982: Wintertime near-surface currents in the Strait of Juan de Fuca, *Atmosphere-Ocean*, **20**, 327-339.

Holbrook, J., R. Muench, and G. Cannon, 1980: Seasonal observations of low frequency atmospheric forcing in the Strait of Juan de Fuca, in *Fjord oceanography*, vol. 4 of *NATO Conf. Ser., Ser. IV: Mar. Sci.*, edited by H. Freeland, D. Farmer, and C. Levings, pp. 305-317, Plenum Press, New York.

Johnson, G., and D. Ohlsen, 1994: Frictionally modified rotating hydraulic channel exchange and ocean outflows, *J. Phys. Oceanogr.*, **24**, 66-78.

Johnson, G., and T. Sanford, 1992: Secondary circulation in the Faroe Bank Channel Outflow, *J. Phys. Oceanogr.*, **22**, 927-933.

Kundu, P., 1990: *Fluid Mechanics*, Academic Press, New York, 638 pp.

Labrecque, A., R. Thomson, M. Stacey, and J. Buckley, 1994: Residual currents in Juan de Fuca Strait, *Atmosphere-Ocean*, **32**, 375-394.

Lavelle, J., and H. Mofjeld, 1983: Effects of time-varying viscosity on oscillatory turbulent channel flow, *J. Geophys. Res.*, **88**, 7607-7616.

LeBlond, P., K. Dyck, K. Perry, and D. Cumming, 1983: Runoff and precipitation time series for the coasts of B.C. and Washington coast, *Tech. Rep. 39.* , Dep. of Oceanogr., Univ. of B.C., Vancouver, Canada.

Lohrmann, A., B. Hackett, and L. Roed, 1990: High resolution measurements of turbulence, velocity and stress using a pulse-to-pulse coherent sonar, *J. Atmos. Oceanic Technol.*, **7**, 19-37.

Lu, Y., 1997: Flow and turbulence in a tidal channel, Ph.D. thesis, University of Victoria, Victoria, Canada.

Lu, Y., and R. Lueck, 1999: Using a broadband ADCP in a tidal channel. Part II: Turbulence, *J. Atmos. Oceanic Technol.*, **16**, 1568-1579.

MacCready, P., 1999: Estuarine adjustment to changes in river flow and tidal mixing, *J. Phys. Oceanogr.*, **29**, 708-726.

Masson, D., and P. Cummins, 1999: Numerical simulations of a buoyancy-driven coastal countercurrent off Vancouver Island, *J. Phys. Oceanogr.*, **29**, 418-435.

Masson, D., and P. Cummins, 2000: Fortnightly modulation of the estuarine circulation in Juan de Fuca Strait, *J. Marine Res.*, **58**, 439-463.

Mertz, G., and Y. Gratton, 1995: The generation of transverse flows by internal friction in the St. Lawrence Estuary, *Cont. Shelf Res.*, **15**, 789-801.

Ott, M., and C. Garrett, 1998: Frictional estuarine flow in Juan de Fuca Strait, with implications for secondary circulation, *J. Geophys. Res.*, **103**, 15657-15666.

Panofsky, H., and J. Dutton, 1984: *Atmospheric turbulence*, Wiley, New York, 397 pp.

Pedlosky, J., 1979: *Geophysical Fluid Dynamics*, Springer-Verlag, New York, 624 pp.

Plueddemann, A., 1987: Observations of the upper ocean using a multi-beam doppler sonar, Ph.D. thesis, Scripps Institution of Oceanography.

Plueddemann, A., and R. Pinkel, 1989: Characterisation of the patterns of diel migration using a doppler sonar, *Deep Sea Res.*, **36**, 509-530.

Pond, S., and G. Pickard, 1983: *Introductory dynamical oceanography*, Butterworth-Heineman, Oxford, 329 pp.

Prandle, D., 1982: The vertical structure of tidal currents, *Geophys. Astrophys. Fluid Dyn.*, **22**, 29-49.

Pritchard, D., 1952: Estuarine hydrography, *Advan. Geophy.*, **1**, 243-280.

Pritchard, D., 1955: Estuarine circulation patterns, *Proc. Amer. Soc. Civ. Eng.*, **81**.

Pugh, D., 1987: *Tides, surges, and mean sea-level*, Wiley, New York, 472 pp.

Rattray, M., and D. Hansen, 1962: A similarity solution for circulation in an estuary, *J. Marine Res.*, **20**, 121-133.

Rossby, C., 1938: On the mutual adjustment of pressure and velocity distribution in certain simple current systems, ii, *J. Marine Res.*, **1**, 239-263.

Simmons, H., 1955: Some effects of upland discharge on estuarine hydraulics, *Proc. Amer. Soc. Civ. Eng.*, **81**.

Soulsby, R., 1983: The bottom boundary layer of shelf seas, in *Physical oceanography of coastal and shelf seas*, vol. 35 of *Elsevier Oceanography Series*, edited by B. Johns, pp. 189-266, Elsevier, Amsterdam.

Soulsby, R., 1990: Tidal-current boundary layers, in *The Sea*, vol. 9A of *Ideas and observations on progress in the study of the seas*, edited by B. LeMéhaute, and D. Hanes, pp. 523-566, Interscience Publishers, New York.

Squire, H., 1933: On the stability of three-dimensional disturbances of viscous flow between parallel walls, *Proc. R. Soc. Lond., A*, **142**, 621-628.

Stacey, M., S. Monismith, and R. Burau, J, 1999a: Measurement of Reynolds stress profiles in unstratified tidal flow, *J. Geophys. Res.*, **104**, 10933-10949.

Stacey, M., S. Monismith, and R. Burau, J, 1999b: Observations of turbulence in a partially stratified estuary, *J. Phys. Oceanogr.*, **29**, 1950-1970.

Stern, M., 1975: *Ocean circulation physics*, Academic Press, New York, 246 pp.

Stommel, H., 1952: Classification of estuaries by salinity structure, in *Collected works of Henry M. Stommel*, vol. III, edited by N. Hogg, and R. Huang, American Meteorological Society, Boston.

Stull, R., 1976: Internal gravity-waves generated by penetrative convection, *J. Acoustic Soc. Am.*, **33**, 1279-1286.

Tennekes, H., 1973: The logarithmic wind profile, *J. Acoustic Soc. Am.*, **30**, 234-238.

Thomson, R., 1981: *Oceanography of the British Columbia coast*, Department of Fisheries and Oceans, Ottawa, 291 pp.

Trump, C., 1983: A current-induced Ekman Spiral in the St. Lawrence Estuary, *J. Phys. Oceanogr.*, **13**, 1540-1543.

Turner, J., 1973: *Buoyancy effects in fluids*, Cambridge University Press, Cambridge, 368 pp.

Turner, J., 1981: Small-scale mixing processes, in *Evolution of physical oceanography*, edited by B. Warren, and C. Wunsch, pp. 236-262, MIT press, Cambridge, Massachusetts.

van Haren, H., N. Oakey, and C. Garrett, 1994: Measurements of internal wave band eddy fluxes above a sloping bottom, *J. Marine Res.*, **52**, 909-946.

von Storch, H., and F. Zwiers, 1998: *Statistical Analysis in Climate Research*, Cambridge University Press, Cambridge, 484 pp.

Waldichuck, M., 1957: Physical oceanography of the Strait of Georgia, British Columbia, *J. Fish. Res. Bd., Canada*, **1(6)**, 321-486.

Wilks, D., 1997: Resampling hypothesis tests for auto-correlated fields, *J. Climate*, **10**, 67-82.

Wunsch, C., 1975: Internal tides in the ocean, *Rev. Geophys. Space Phys.*, **13**, 167-182.

Yih, C., 1955: Stability of two-dimensional parallel flows for three-dimensional disturbances, *Q. Appl. Math.*, **12**, 434-435.